8-2012

Two-Dimensional Blood Flow Velocity Estimation Using Ultrasound Speckle Pattern Dependence On Scan Direction And Velocity

Tiantian Xu
University of Nebraska-Lincoln, eason1984@gmail.com

TWO-DIMENSIONAL BLOOD FLOW VELOCITY ESTIMATION USING ULTRASOUND SPECKLE PATTERN DEPENDENCE ON SCAN DIRECTION AND VELOCITY

by

Tiantian Xu

A DISSERTATION

Presented to the Faculty of

The Graduate College at the University of Nebraska

In Partial Fulfillment of Requirements

For the Degree of Doctor of Philosophy

Major: Engineering

Biomedical Engineering

Under the Supervision of Professor Gregory R. Bashford

Lincoln, Nebraska

August, 2012

TWO-DIMENSIONAL BLOOD FLOW VELOCITY ESTIMATION USING ULTRASOUND SPECKLE PATTERN DEPENDENCE ON SCAN DIRECTION AND VELOCITY

Tiantian Xu, Ph.D.

University of Nebraska, 2012

Advisor: Gregory R. Bashford

Cardiovascular disease is the leading cause death in the United States. Although emergency surgery and medicine can be used for cardiovascular disease treatment, the survivors will suffer for it afterwards. Ultrasound blood flow measurement provides a noninvasive way for cardiovascular diseases diagnosis. In this dissertation, three algorithms for blood flow velocity measurements were investigated and optimized. Feature tracking has been previously proposed for vector velocity measurement. In Chapter 3, the optimal amplitude and time thresholds for feature extraction were investigated to minimize flow estimate variance while providing sufficient spatial and temporal coverage of flow area. A new method of lateral blood flow velocity measurement was investigated in Chapter 4 using the observation that the speckle pattern corresponding to blood reflectors stretches if the blood is moving in the same direction as the electronically-controlled transducer line selection in a 2-D image. The results demonstrated that there is a linear relationship between the speckle size and blood flow velocity, which can be used for ultrasound blood flow velocity measurement. To improve the lateral blood flow estimation performance using speckle size estimation, the relationship between blood flow velocity estimation for flow purely lateral to the

ultrasound beam and flow gradient, random scatterer movement and ROI size was investigated and quantitatively assessed in Chapter 5. By changing the ROI sizes, the results showed that different optimal ROI sizes exist in different flow profile regarding the flow gradient and random scatterer movement. The method of blood flow velocity estimation using speckle size estimation was further tested *in vivo* with jugular vein blood flow from human subjects in Chapter 6. The results showed that speckle size estimation has a comparable estimation performance to spectral Doppler with potential time savings. Finally, a two-dimensional blood flow velocity estimation algorithm using apparent speckle pattern angle was proposed in Chapter 7. The apparent angle of speckle pattern changes with different scan velocities due to mis-registration between the ultrasound beam and scatterers. Results showed that this algorithm can resolve the amplitude and angle of the blood flow simultaneously.

Acknowledgements

I would like to thank Dr. Bashford for his valuable guidance throughout my graduate program. I thank him for his continuous supporting and encouraging both for my research work and career development. Thanks for his warm kindly relationship with his students, which makes his lab an energetic place for studying, working and living.

I also thank Dr. David Jones, Dr. John Paul Barton, Dr. Michael W Hoffman and Dr. Shadi Othman for serving on my Ph.D. dissertation committee. Thanks for their valuable thoughts and insights regarding the quality and significance of my dissertation.

I would like to thank all the members in the Biomedical Imaging and Biosignal Analysis Laboratory. Throughout my five years study in Nebraska, I received generous help, kind solicitude and countless fun from them. They made my life in Nebraska more meaningful and memorable.

Last and most important, I owe my deepest thanks to my parents Chenquan Xu and Kaiqing Zhang for their endless and self-giving love, caring and encouraging. Thank them for giving me support and confidence for every decision I made for my life. Thank them for giving me help and strength during my dark time. Thank them for always being with me in pursuing my dreams.

Contents

List of Symbols and Abbreviations

Symbols

c	Speed of sound [m/s]
v	Velocity of blood flow and tissue motion [m/s]
b	Bulk modulus [Pa]
ρ	Tissue density [kg/m^3]
z	Acoustic impedance [rayls]
f_0	Center frequency of ultrasound transducer [Hz]
f_s	Sampling frequency [Hz]
f_d	Doppler frequency [Hz]
ω	Angular frequency [rad/s]
θ	Angle between ultrasound beam and blood flow [degree]
λ	Wavelength [m]
T_{prf}	Pulse repetition interval [s]

Abbreviations

FWHM	Full width of half maximum
ACVF	Autocovariance function
SNR	Signal to noise ratio
PRF	Pulse repetition frequency

PRI	Pulse repetition interval
RMS	Root mean square
RF	Radio frequency signal
A-line	Amplitude mode in which a trace that shows the instantaneous echo signal amplitude versus time after transmission of the ultrasound pulse
B-mode	Brightness mode in which a ultrasound transducer simultaneously scans a plane through the body that can be viewed as a two dimensional image on screen
URI	Ultrasound research interface
ROI	Region of interest
SF	Stretch factor
IRB	Institutional review board

List of Figures and Tables

Chapter 1

Introduction

1.1 Clinical relevance

Cardiovascular diseases cause serious pathologies that affect the heart and blood vessels, such as stroke, heart attack and arrhythmia. It is the leading cause of death in the United States (The Heart Foundation 2012). In 2008, 32.8% (811,940 out of 2,471,984) of deaths in the United States were caused by cardiovascular diseases (Roger 2012). For example, stroke is one kind of cardiovascular disease that affects the arteries leading to and within the brain (American Stroke Association 2012). Stroke can be classified into two categories. The first kind of stroke is called as ischemic stroke, which occurs when

the blood flow to the brain is obstructed by a clot in the vessel. The second kind of stroke is called as hemorrhagic stroke, which occurs when the blood vessel in the brain is ruptured (American Stroke Association 2012).These two types are shown in Fig. 1.1. When a stroke happens, part of the brain cannot get the blood and oxygen it needs, and the brain tissues start to die. This could result in diseases, such as paralysis, vision problems, abnormal behavioral style and memory loss. The impairments typically occur on the opposite of body since one side of the brain controls the opposite side of the body (Gray 1918; American Stroke Association 2012). Emergency treatment of stroke includes dissolving the clot in the blood vessel for ischemic stroke and reducing blood pressure for hemorrhagic stroke. However, stroke can cause permanent damage to the brain tissue, which is difficult to rehabilitate (Golstein et al. 2011). The estimated medical cost of stroke in 2008 was $34.3 billion (Roger 2012). This cost increased to $73.7 billion in 2010 (American Stroke Association 2012). Besides stroke, other cardiovascular diseases, such as heart attack and arrhythmia have similar healthcare costs (Roger 2012). As a result, the estimated cost of cardiovascular diseases for 2008 is $297.7 billion, and this number is expected to triple from 2010 to 2030 (Roger 2012). Thus, the best way of reduce the cost of cardiovascular diseases will be effective prevention measures (Golstein et al. 2011).

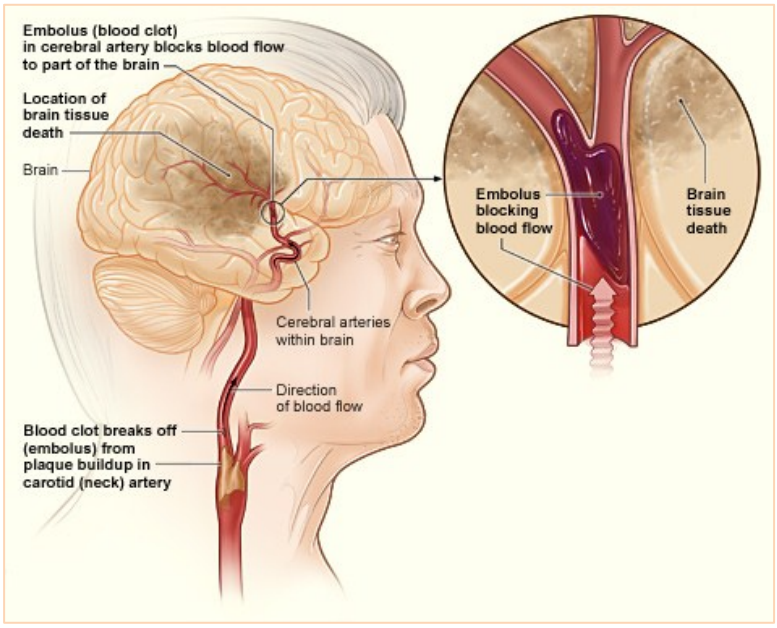

(a)

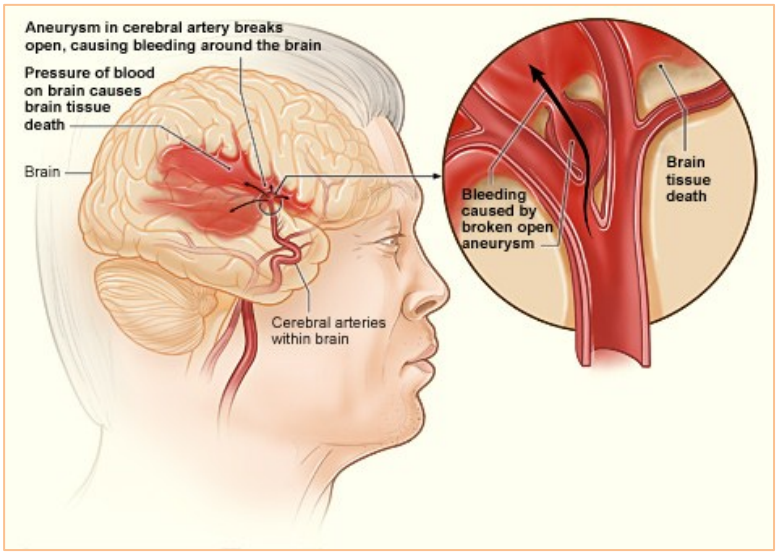

(b)

Fig. 1.1. Reprinted from National Heart Lung and Blood Institute (NHLBI) website. Two types of stroke. a) Ischemic stroke caused by a clot obstructing the flow of blood to the brain, b) hemorrhagic stroke caused by a blood vessel rupturing and preventing blood flow to the brain. (NHLBI 2012)

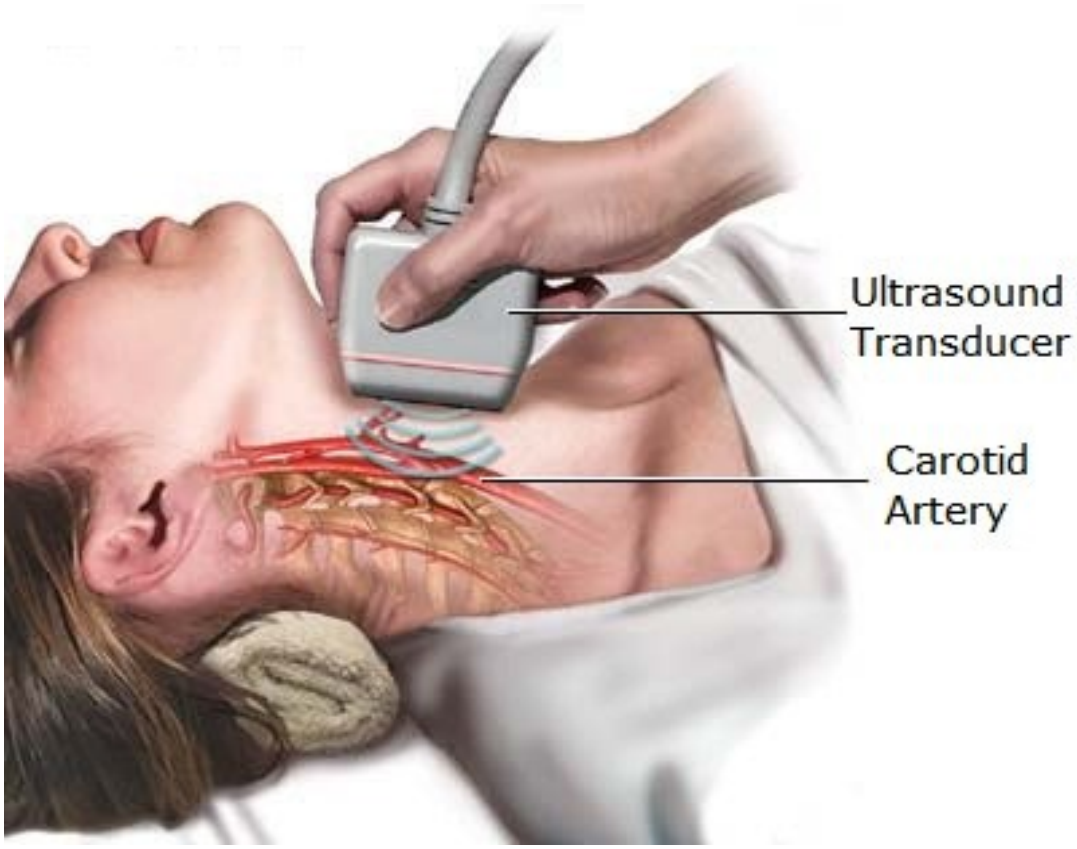

Fig. 1.2. Reprinted from AllRefer website. An example of carotid ultrasound scan. An ultrasound transducer is placed over the suspect arteries in the neck, and information about the vessel's blood flow is collected. (AllRefer 2012)

It is known that the distribution of the blood velocities within a vessel contains valuable diagnostic information (Hein and O'Brien 1993). For example, when a stroke occurs, the blood vessel will be either blocked by a clot or burst, both of which cause abnormal blood-flow velocities. A noninvasive way of monitoring the cardiovascular blood flow velocity will help clinicians assess the health of cardiovascular system and could prevent imminent stroke. Ultrasound blood flow estimation is one of the methods used to investigate the condition of arteries. As shown in Fig. 1.2, an ultrasound transducer is placed over the suspect artery, especially arteries in the neck (carotid) for blood flow detection. The piezoelectric elements in the ultrasound transducer first emit

ultrasound waves into the human body after being excited by a short duration of electric voltage, and the reflected ultrasound waves produced by constructive and deconstructive interference of scatterer reflections will be received by the transducer. Different tissues have different echogenicity (composite amplitude of the reflected ultrasound wave). For example, blood has a lower echogenicity compared with other human tissues; thus blood is seen as dark areas in ultrasound images. In this way, the brightness of reflected ultrasound can be used to view the inner anatomy structure of human tissue. Furthermore, successive reflected ultrasound waves also contain information which can be monitored to resolve the motion of tissues (including blood).

The "Doppler effect" in ultrasound (actually a measurement of phase change) is widely used in ultrasound to measure blood-flow. Upon insonification by an ultrasound beam (a mechanical disturbance with a wave-like nature in the body), the echoes scattered by blood cells carry information about the velocity of blood flow. Blood flow estimation is used on most commercial ultrasound machines. In current clinical ultrasound machines, the one dimensional (1-D) blood flow velocity vector projection along the axial dimension of the ultrasound beam is estimated. There are two main modes of blood flow estimation which used the "Doppler" effect on commercial machines. The first was developed by Kasai et al., who created an algorithm to quickly estimate the mean velocity over a large spatial field of view (e.g. 5 cm by 5 cm) based on an autocorrelation technique (Kasai et al. 1985), which is now commonly referred to as "color flow." A complementary method, referred to as "spectral Doppler," is capable of visualizing a velocity distribution at a single (resolution-limited) small region of interest

by displaying a spectral plot of the (temporal- and wall-filtered) flow signal (Jensen and Svendsen 1996).

However, neither mode is able to measure the velocity vector projection along the lateral dimension of the ultrasound beam, since there is no Doppler frequency shift (or phase shift) when the transducer face is aligned parallel to blood flow. Some researchers have formed alternative estimation algorithms to solve this problem. A complete literature review is given in Chapter 2. These methods either use information from multiple ultrasound beam scan positions or require multiple images and measure speckle position change.

1.2 Long term goal

The long-term objective of this research is to develop a commercially applicable algorithm that measures three-dimensional (3-D) volume blood flow, in real-time, over a broad field of view. In this dissertation, novel methods termed "multiple-PRF scanning" and speckle size estimation were developed as a step towards the long-term objective. A commercially available 1-D linear ultrasound transducer will be used to collect B-mode ("brightness" mode in which a transducer simultaneously scans a plane through the body that can be viewed as a two dimensional image on a screen) images of blood flow with different scanning velocities, which represents the spatial rate at which individual ultrasound A-lines ("amplitude" mode in which a trace that shows the instantaneous echo signal amplitude versus time after transmission of the ultrasound pulse) are collected laterally across the transducer. During data acquisition, the scan velocity and blood flow are in the same direction. The algorithms developed only need one B-mode image of

blood flow for each scan velocity to make a blood flow estimate (although further images increase the accuracy of estimate) and provide a fast way of 2-D blood flow measurement. Detailed information of blood flow, including velocity amplitude and flow angle, can then be calculated. In this work, 2-D flow measurement was accomplished through data post processing, although future work could include real-time estimation with an embedded system. Physicians can potentially use this information for better diagnosis of the health of cardiac muscle to predict and prevent cardiac diseases, such as heart attack and stroke.

1.3 Contribution of this dissertation

The goal of this work is to take certain steps towards the long-term goal. Specifically, a new method of 2-D blood flow measurement needs to be theoretically developed, tested through computer simulations and experiments using a blood flow phantom, and then tested in *in vivo* experiments. The contribution of this dissertation may be specified as follows:

i. Theoretically develop an algorithm for 1-D lateral blood flow measurement, which is angle independent and requires less computational complexity compared with traditional methods, such as Doppler and speckle tracking (Chapter 4).
ii. Verify the feasibility and performance of the algorithm using an ultrasound computer simulation (Field II). Implement the algorithm on a PC, and test its effectiveness and accuracy using a blood flow phantom with commercial ultrasound imaging system (Chapter 4).

iii. Investigate parameter configurations of the algorithm regarding the speckle decorrelation. Improve the estimation accuracy according to different blood flow profiles (Chapter 5).

iv. Test the effectiveness and accuracy of the blood flow estimation algorithm on human subjects, using post-processed data acquired from a commercial ultrasound machine (Chapter 6).

v. Extend the algorithm to 2-D blood flow measurement to automatically resolve the direction and amplitude of the blood flow simultaneously. Test its effectiveness and accuracy with computer simulation (Field II) and Phantom experiments (Chapter 7).

Chapter 2

Background and Literature Review

2.1 Ultrasound blood flow estimation

Ultrasound is a kind of mechanical wave with frequency above 20 kHz. It can propagate in solids, fluid and gases. In the human body, the main component of the ultrasound wave is in the longitudinal direction. The longitudinal speed of ultrasound c (m/s) in human body depends on the properties of tissue through which it propagates. Furthermore, different tissues have different mechanical properties that affect ultrasound reflection. In ultrasound, the ratio between sound pressure p (Pa) and particle velocity v_p

(m/s) is called acoustic impedance (actually characteristic impedance) Z (*rayls,* kg/s/m^2), which is shown as follows:

$$z = \frac{p}{v_p} \tag{2.1}$$

The relationship between Z and the speed of sound c can be represented as follows:

$$c = \frac{Z}{\rho} = \sqrt{\frac{B}{\rho}} \tag{2.2}$$

where B (Pa) is the bulk modulus and ρ (kg/m^3) is the density. Ultrasound imaging is based on the reflection/scattering of acoustic waves in the medium (Christensen 1988, Zhai 2009). The ultrasound transducer is the key component for ultrasound image formation. It is formed of individual piezoelectric elements, which mechanically deform when a voltage potential is placed across their surface and vice versa (Insana 2006). During ultrasound imaging, the transducer is excited by a short duration of voltage waveform (e. g., 0.3-1 μs, 1-4 cycles, ~100 V) and emits ultrasound beams into media, such as the human body. Part of the ultrasound waves will be attenuated by reflection, scatter at interfaces and be absorbed in body tissues, depending both on the ultrasound frequency and propagation depth (e. g., 0.5 dB/MHz/cm in human liver). The remaining energy will be reflected back to the transducer or continue on (transmit) further in depth. To form ultrasound images using reflected and scattered ultrasound waves, the transducer is switched to reception mode immediately after being pulsed by special circuitry. Most modern transducers are made of a group of closely spaced piezoelectric elements. For example, the VF 13-5 linear array transducer of the Siemens Antares ultrasound imaging system (Siemens Medical Solutions, Ultrasound Division, Issaquah, WA) has 192

individual elements. The width and height of each element is 0.176 mm and 2.5 mm. The kerf (distance between two adjacent elements) is 25 μm and the transducer has an overall lateral aperture size as 3.38 cm. In transmission mode, each element can be excited individually with a different time delay to form ultrasound beams with a specific emitting direction and focal position. In reception mode, the reflected ultrasound waves detected by each element will be individually delayed and summed in a similar way to form ultrasound beams with a preferential receiving direction and focal position. This process is called beamforming, which is shown in Fig. 2.1. Generally, ultrasound beams can only

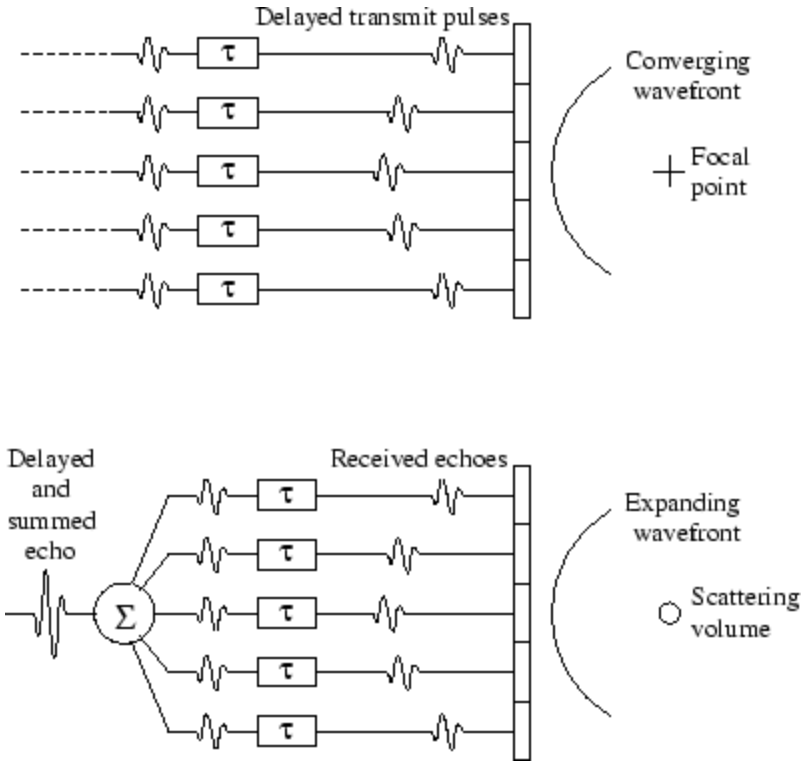

Fig. 2.1. Reprinted from Anderson et al. 2006. "A conceptual diagram of phased array beamforming. (Top) Appropriately delayed pulses are transmitted from an array of piezoelectric elements to achieve steering and focusing at the point of interest. (For simplicity, only focusing delays are shown here.) (Bottom) The echoes returning are likewise delayed before they are summed together to form a strong echo signal from the region of interest." (Anderson and Trahey 2006)

focus once during transmission but can focus at multiple positions during reception, which is called dynamic receiving (Von Ramm and Smith 1983). The received ultrasound signals are then demodulated and filtered to generate *I* (in phase) and *Q* (quadrature) signals. The envelope of the complex *IQ* signals is detected to obtain information about the human body, which can be seen in Fig. 2.2.

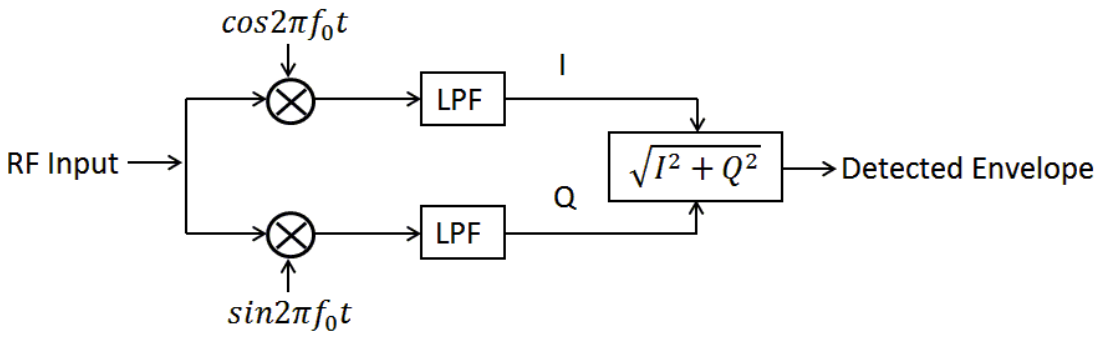

Fig. 2.2. The procedure of envelope detection. RF signals are demodulated by two local oscillators with transmitting frequency f_0. Demodulated signals are filtered by low-pass filters to generate *I* (in phase) and *Q* (quadrature) signals. The envelope of the complex *IQ* signal is then detected.

Blood flow measurement is one of the major functions of an ultrasound imaging system. Conventional methods (available on most commercial ultrasound machines) operate in one dimension (1-D) and estimate the velocity vector projection along the axial dimension of the ultrasound beam. Although they are all called Doppler effects based methods, only continuous-wave Doppler method resolves the actual Doppler frequency from the reflected ultrasound waves. Other methods, such as spectral Doppler and color Doppler, use the phase shift of the reflected ultrasound waves for blood flow velocity estimation.

2.1.1 Continuous-Wave Doppler

Continuous-wave Doppler is the simplest method of blood flow detection using ultrasound. Typically, a continuous-wave Doppler transducer contains two separate elements to transmit and receive ultrasound waves. A continuous ultrasound wave with center frequency f_0 is emitted into the body with a transmitting element, while simultaneously detecting the reflected ultrasound wave with the receiving element. The frequency of the received ultrasound wave contains both the center frequency and Doppler frequency f_d. Post processing can extract out the Doppler frequency by demodulation with a local oscillator with the center frequency f_0 followed by a low-pass filter. The blood flow velocity is calculated by the Doppler equation as follows:

$$v = \frac{f_d \cdot c}{2f_0 \cdot cos\theta} \tag{2.3}$$

where v is blood flow velocity, c is the speed of ultrasound in human tissue (e. g., 1540 m/s) and θ is the angle between ultrasound beam and blood flow.

A typical configuration of the continuous-wave Doppler can be seen in Fig. 2.3. During the continuous ultrasound beam transmitting and receiving, all the scatterers along the propagation path of the ultrasound beam will contribute to Doppler signals. Thus, continuous-wave Doppler cannot collect Doppler signals and measure the blood flow velocity at a specific location. Although the other two main methods of flow estimation are also termed “Doppler”, continuous-wave Doppler is the only method that truly measures the Doppler shift (frequency shift due to moving media).

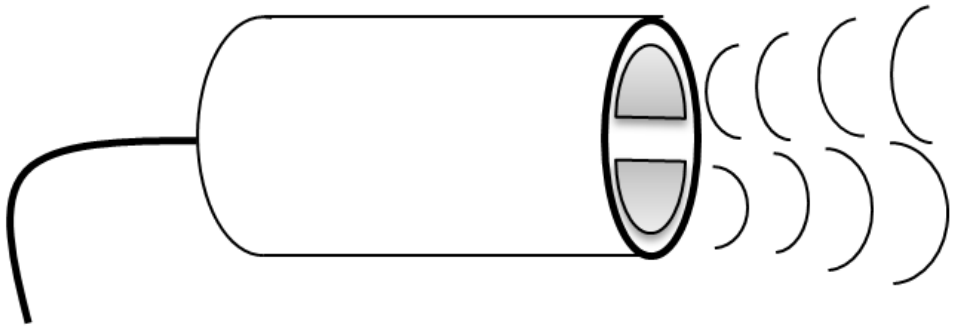

Fig. 2.3. A continuous-wave Doppler transducer contains two separate elements to transmit and receive ultrasound waves.

2.1.2 Spectral Doppler

In contrast to continuous-wave Doppler, spectral Doppler emits pulsed ultrasound beams into the blood flow with a certain pulse repetition frequency (PRF). Typically, 64-128 A-lines are obtained by emitting and receiving ultrasound beams in a specific direction. To measure the blood flow velocity at a specific depth, the A-lines are time-gated to extract signals from a desired depth. Both the amplitude and phase information of the time-gated signals are preserved. If the time-gated signals originate from moving reflectors, such as blood flow, their phase will change during subsequent pulse-echo interrogations. Thus, a new signal is constituted by the time-gated signals from repeated pulse-echo sequences, which is the Doppler signal. As shown in Fig. 2.4, the frequency of the Doppler signal is scaled by the blood flow velocity, which can be used for blood flow velocity measurement (Evans et al. 1989; Hoskins 1999; Jensen 2007). A windowed

Fourier transform (aiming to suppress the sidelobes in the spectrum) is usually performed on the Doppler signal to calculate the velocity spectrum of the blood flow.

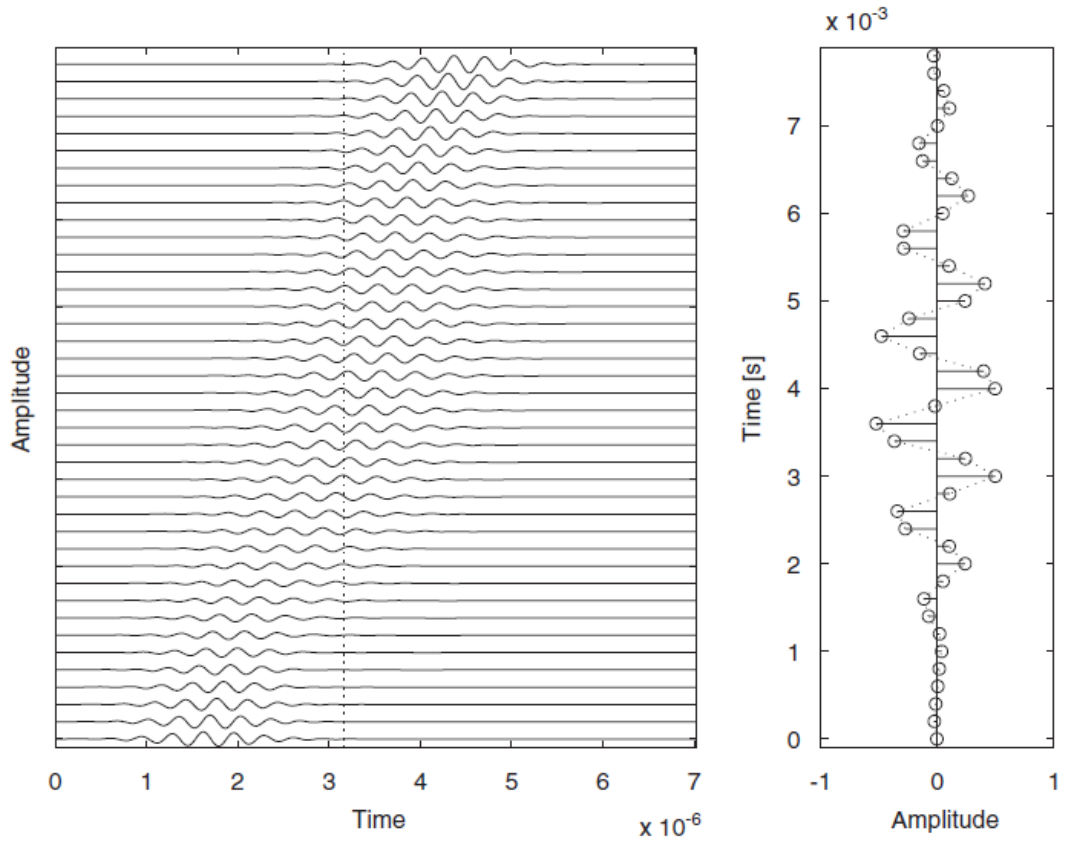

Fig. 2.4. Reprinted from Jensen, 2007. "RF sampling of single pulse moving away from the transducer. The left graph shows the different received RF lines, and the right graph is the sampled signal. The dotted line indicates the time when samples are acquired" (Jensen 2007).

Fig. 2.5 shows a screen shot of spectral Doppler which is available on most commercial ultrasound machines. The top half of the screen shows the anatomic gray scale (B-mode) image of the carotid artery. The bottom half shows the velocity spectrum of the blood flow in the vessel. In the B-mode image, the longest white solid line indicates the beam direction. The two short parallel line segments indicate the time-gated window. The line running through the center of the gate is used to determine the angle between blood flow and ultrasound beam. Usually, a gate (e. g., 1 – 2 mm wide) will be

manually (e. g., by use of a trackball) placed along the beam direction in the middle of the vessel. This gate indicates what depth the ultrasound signals are sampled between successive pulse-echo sequences. A cursor in the middle of the gate is manually adjusted to align with the blood vessel. Once the gate and cursor are manually positioned, the angle between the ultrasound beam and blood flow vessel is stored in the ultrasound machine and used for a cosine correction during blood flow velocity estimation.

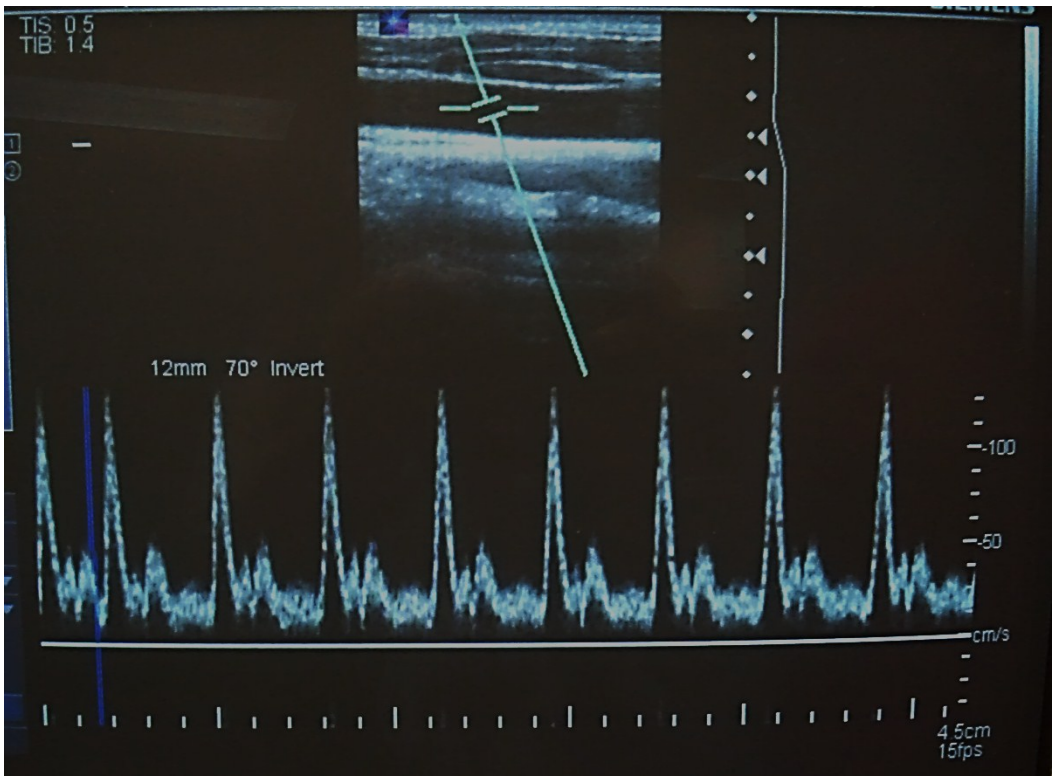

Fig. 2.5. A screen shot of spectral Doppler showing both B-mode image and spectrogram of the carotid artery. The Doppler signal is collected from the gate along the beam direction.

2.1.3 Color Doppler

A complementary method, referred to as color Doppler, was developed by Kasai *et al.* to quickly estimate the mean velocity over a large spatial field of view based on an autocorrelation technique (Kasai and Namekawa 1985). In color Doppler, 8-16 lines of

data in one direction are acquired and divided into a number of segments based on a resolution-cell. According to Wagner's work (1983), the axial resolution-cell size S_z is defined as a half of the ultrasound pulse length, and the lateral resolution-cell size S_x *is* defined as follows:

$$S_x = \frac{\lambda z_0}{D} \tag{2.4}$$

where λ is the ultrasound wavelength, z_0 is the focal distance and D refers to the transducer dimension in the transverse direction. Successive complex (typically 8-16) samples from each segment will be used to estimate the blood flow velocity, which can be seen in Fig. 2.6.

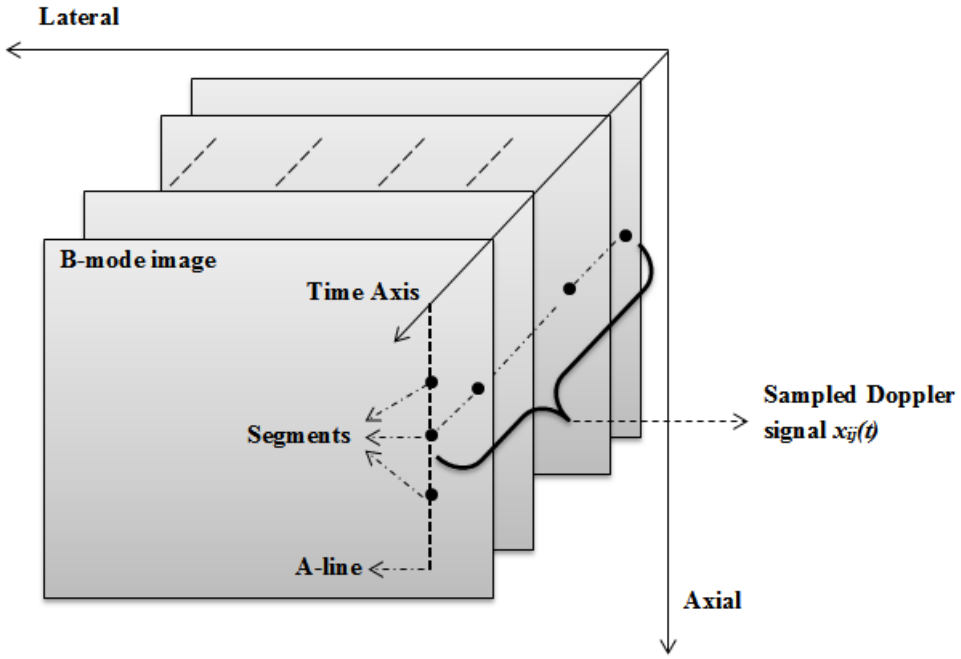

Fig. 2.6. A diagram of color Doppler. Samples at specific locations in successive B-mode images are collected to form the Doppler signal $x_{ij}(t)$, where i and j represents the location of the samples and t represents the sampling time.

Theoretically, the mean frequency of the complex samples from each segment can be used to estimate the mean blood flow velocity at that depth. As described in Kasai's work (1985), the mean blood flow velocity can be calculated as follows:

$$\bar{\omega} = \frac{\int_{-\infty}^{+\infty} \omega P(\omega) d\omega}{\int_{-\infty}^{+\infty} P(\omega) d\omega} \; and \; \bar{v} = \frac{\bar{\omega}}{2\pi f_o} \frac{c}{2} \tag{2.5}$$

where ω is the angular frequency of the sampled signal, $P(\omega)$ is the power spectral density the sampled signal, c is the speed of ultrasound, f_0 is the center frequency of the ultrasound waves, $\bar{\omega}$ is the mean angular frequency of the sampled signal and $\bar{v}$ is the mean velocity of the blood flow. However, the computation of evaluating the theoretical equation is complex in practice. Hence, an alternative method of calculating the mean frequency has been implemented in commercial ultrasound machines using the autocorrelation function of sampled signals. Suppose that the autocorrelation function of the samples is defined as follows:

$$R_{ij}(\tau) = \int_{-\infty}^{+\infty} x_{ij}(t)\, x_{ij}{}^{*}(t-\tau) dt \tag{2.6}$$

where $x_{ij}(t)$ is the sampled signal at a specific location denoted by coordinates (i, j) at time t. $R_{ij}(\tau)$ is the autocorrelation function of $x_{ij}(t)$ with time interval τ. The symbol * represents complex conjugate. The mean frequency of the sampled signal can be approximated by measuring the phase changing rate of the autocorrelation function within the first lag (Kasai and Namekawa 1985). In commercial ultrasound machines, the blood flow velocity is estimated as follows:

$$\bar{v} = -\frac{c}{4\pi f_0 T_{prf}} arctan\left(\frac{Im(R_{ij}(T_{prf}))}{Re(R_{ij}(T_{prf}))}\right) \tag{2.7}$$

where T_{prf} is the pulse repetition interval (PRI) between two successive pulse-echo sequences. $Im(R_{ij}(T_{prf}))$ is the imaginary part of the autocorrelation function, and $Re(R_{ij}(T_{prf}))$ is the real part of the autocorrelation function. Fig. 2.7 shows a screen shot of a typical color Doppler image. The colors are superimposed on the B-mode image to represent the amplitude and direction of the blood flow velocity. In the jugular vein, the color of blood flow is blue, which means that it flows away from the transducer. In the carotid artery, the color of the blood flow is red, which means that it flows towards the transducer.

Fig. 2.7. A screen shot of color flow image of carotid artery bifurcation. The velocity information is superimposed on the B-mode image. The color represents the direction of the blood flow.

Note that Doppler methods are not able to measure the velocity vector projection along the lateral dimension of the ultrasound beam, since there is no Doppler frequency shift (or phase shift) when the transducer face is aligned parallel to the blood flow. Some researchers have formed alternative estimation algorithms to solve this problem. For example, estimating the transit time across the ultrasound beam was proposed for measuring flow parallel to the transducer face. One method described by Newhouse and Reid measures the variance of the Doppler signals returned from lateral flow (Newhouse and Reid 1990, Newhouse et al. 1987). Vector Doppler is an extension of 1-D Doppler techniques by emitting ultrasound beams along different angles and making vector velocity estimations through triangulation (Fox 1978; Overbeck et al. 1992; Scabia et al. 2000; Dunmire et al. 2000; Hein 1997). Transverse spatial modulation applies lateral modulation in the ultrasound field to make the received signal influenced by transverse motion (Anderson 1998; Jensen and Anderson 1998). Speckle tracking measures multidimensional blood flow by tracking the displacement of speckle patterns generated by scatterers (typically red blood cells) in blood (Trahey et al. 1987; Bohs et al. 1991; Embree and O'Brien 1985; Philips et al. 1995; Swillens et al. 2010). Maximum likelihood blood velocity estimation incorporates properties of flow physics into the cross correlation function to perform 2-D flow imaging (Schlaikjer and Jensen 2004). Other techniques such as sample tracking (Zahiri-Azar and Salcuden 2008), maximum likelihood estimator (Ferrara and Algazi 1991) and multidimensional spectrum analysis (Niels et al. 2008) have also been proposed. All of these methods either use information from multiple ultrasound beam scan positions or require multiple images and measure speckle position change.

2.2 Feature tracking

In speckle tracking, the displacement of speckle patterns generated by scatterers is extracted and tracked through successive ultrasound signals. The tracking is completed by searching for the most similar part of signals by applying cross-correlation estimation across a "searching" area in subsequent ultrasound signals. In one-dimensional (1-D) data, a short segment of ultrasound signals is tracked, which is simple to implement. For two-dimensional (2-D) ultrasound images, a region of interest (ROI) from the ultrasound image is tracked through successive images, which significantly increases the computational complexity. When speckle tracking is applied to three-dimensional (3-D) data, a volume of ultrasound data is extracted and tracked through successive ultrasound volumes. The enormous computational complexity makes it difficult to implement this algorithm in real time. To search for a more computationally efficient, accurate blood flow estimation method, feature tracking has been proposed and investigated (Roundhill 1991; Bashford and Von Ramm 1996, Kuo and Von Ramm 2008).

Feature tracking identified trackable features from received ultrasound signals and tracked them over space and time. These trackable features include local minima or maxima in 1-D, 2-D and 3-D ultrasound signals (Bashford and Von Ramm 1996). In practice, since "minima are low-amplitude values and more easily lost in noise, typically the maxima are selected for feature tracking" (Bashford and Robinson 2007). Theoretically, the local maxima occur when the first-order derivative equals zero. In practice, searching for the local maxima is done by locating the position where the amplitude difference between two adjacent sample points changes sign along a certain direction, which can be further simplified as difference and comparison operations

(Bashford and Robinson 2007). A list of local maxima is selected from ultrasound signals in this way. Before using these local maxima as features, thresholds are applied to select qualified features above certain amplitude (amplitude threshold) and time width (time threshold). The selected features are indexed and saved. Similar procedures are performed to successive ultrasound signals. Then, the corresponding features in successive ultrasound signals or images are used to calculate the velocity and direction of target movement. A diagram of tracking process is shown in Fig. 2.8. The blood flow velocity v is estimated as follows:

$$v = \frac{\Delta L}{t} \tag{2.8}$$

where the ΔL is the traveling distance of the feature and t is the traveling time.

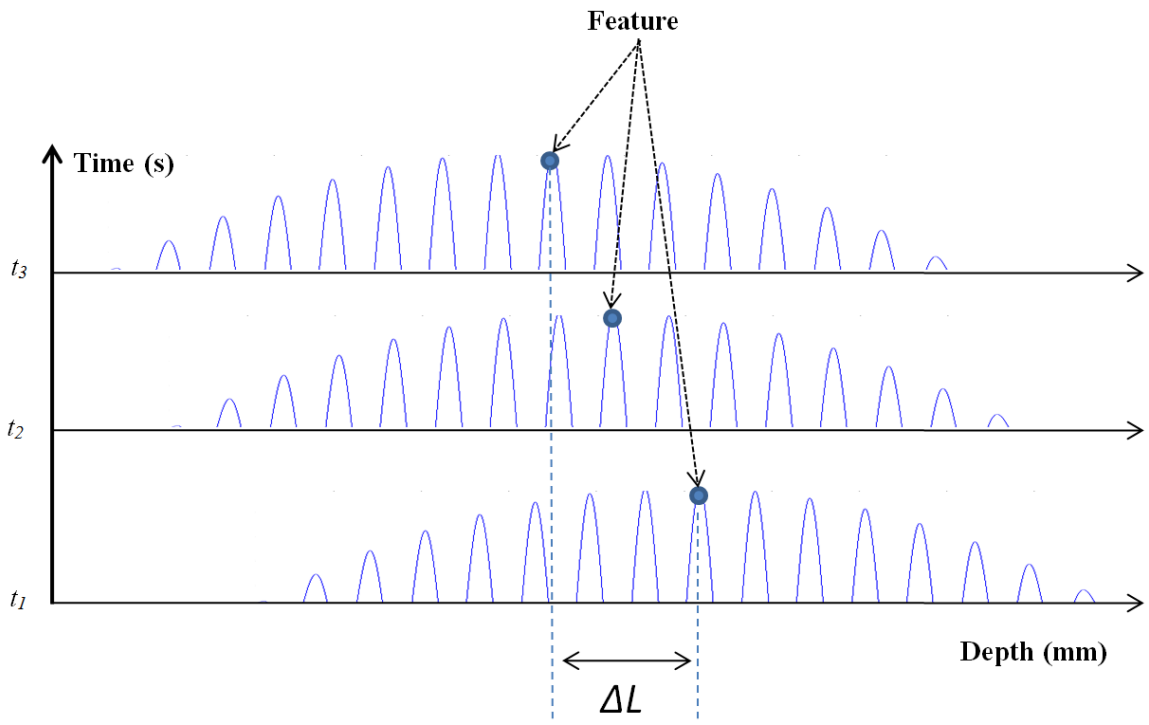

Fig. 2.8. Diagram of feature tracking process (1-D). ΔL is the traveling distance of the feature and t is the traveling time.

2.3 Ultrasound speckle

Ultrasound B-mode images have a granular appearance, which is called "speckle". It can also be seen through other coherent imaging modalities, such as optical imaging and radar. In medical ultrasound, after the ultrasound beam is emitted into the medium, such as human body, the ultrasound wave will be reflected, refracted and attenuated by scatterers. This process can be simulated as an accumulation of ultrasound waves with random phases between 0 and 2π. The real and imaginary parts of the complex echo signals have a jointly Gaussian probability density. After envelope detection, the amplitude of the speckle will have a Rayleigh distribution (Goodman 1975; Burckhardt 1978). In medical ultrasound images, when multiple scatterers are homogeneously distributed in a resolution cell, the second order statistics of the speckle pattern, such as autocovariance function (ACVF), is not dependent on tissue structure, but rather on transducer and geometry parameters (Wagner et al. 1983). Fig. 2.9 represents the normalized ACVF in the transverse direction, which is theoretically predictable by the scanning system parameters. However, when the scatterers are spatially organized or on the scale of the resolution cell size, the ACVF will also contain the information of tissue structures (Wagner et al. 1983), which can be seen in Fig. 2.10. It shows that the Achilles tendon has a laterally correlated pattern as a result of the spatially organized scatterers, while in the surrounding tissue; the speckle pattern is more granular since the scatterers are homogeneously distributed.

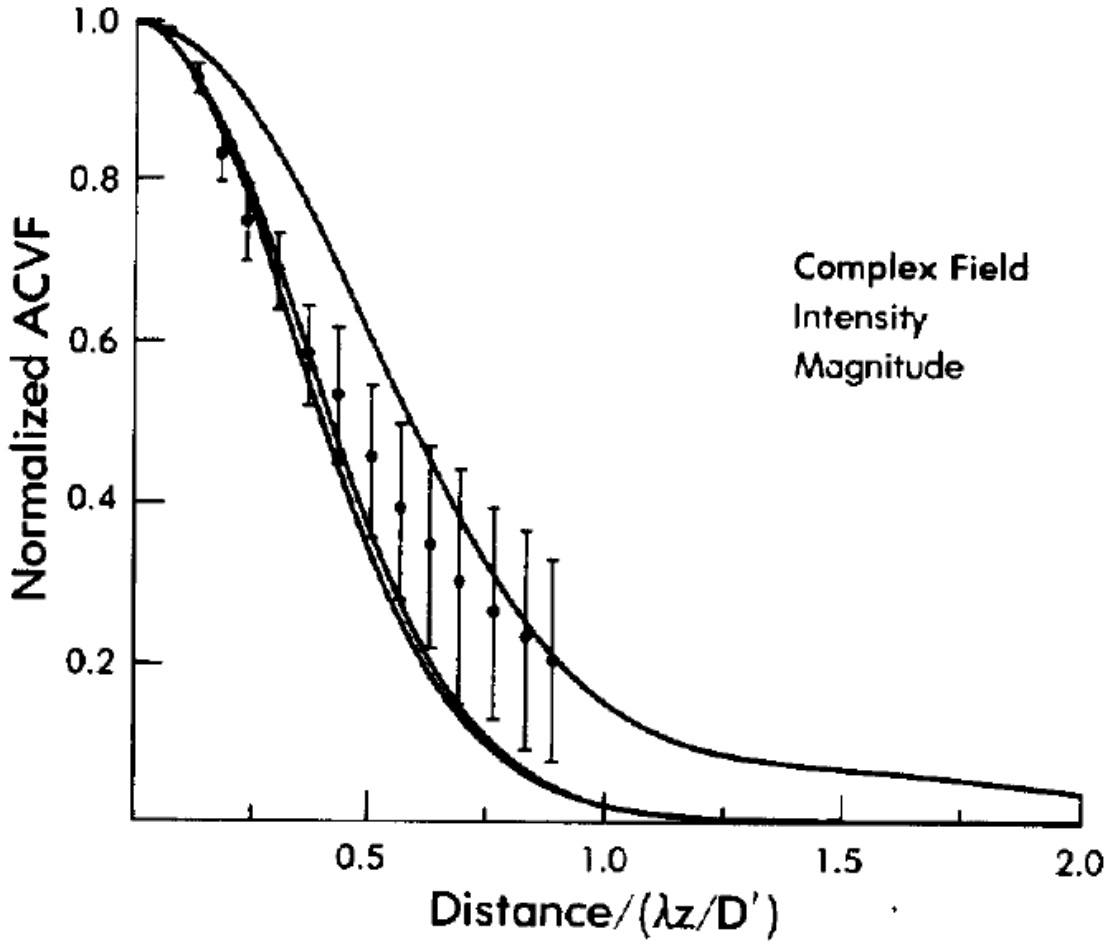

Fig. 2.9. Reprinted from Wagner, 1983. "Theoretical autocovariance functions for (top to bottom) complex field, intensity, and magnitude for transverse direction or direction of scan. Data points with error bars are mean (plus and minus two standard errors) of six experimentally determined autocovariance functions from B-scans of two scattering phantoms (20 μm scattering particles, and 150 μm scattering particles) at three frequencies."(Wagner et al. 1983).

In most cases, speckle is an undesired property in ultrasound imaging, which can reduce the imaging resolution and contrast. Many methods have been proposed to suppress the speckle during ultrasound imaging (Ortiz et al. 2012). However, speckle can be the signal used for ultrasound blood flow estimation. The scatterers (e. g., the red blood cells) in blood flow produce speckle patterns which can be detected and amplified by the ultrasound imaging system. The information of blood flow velocity can be

extracted from the speckle patterns with post data analysis (e. g., Doppler effects, speckle tracking). Fig. 2.11 shows a typical ultrasound blood flow image from a blood flow phantom. The area of blood flow is dark in the ultrasound image compared with surrounding tissue. After filtering and amplifying, speckle patterns in the dark area will be used for blood flow velocity estimation.

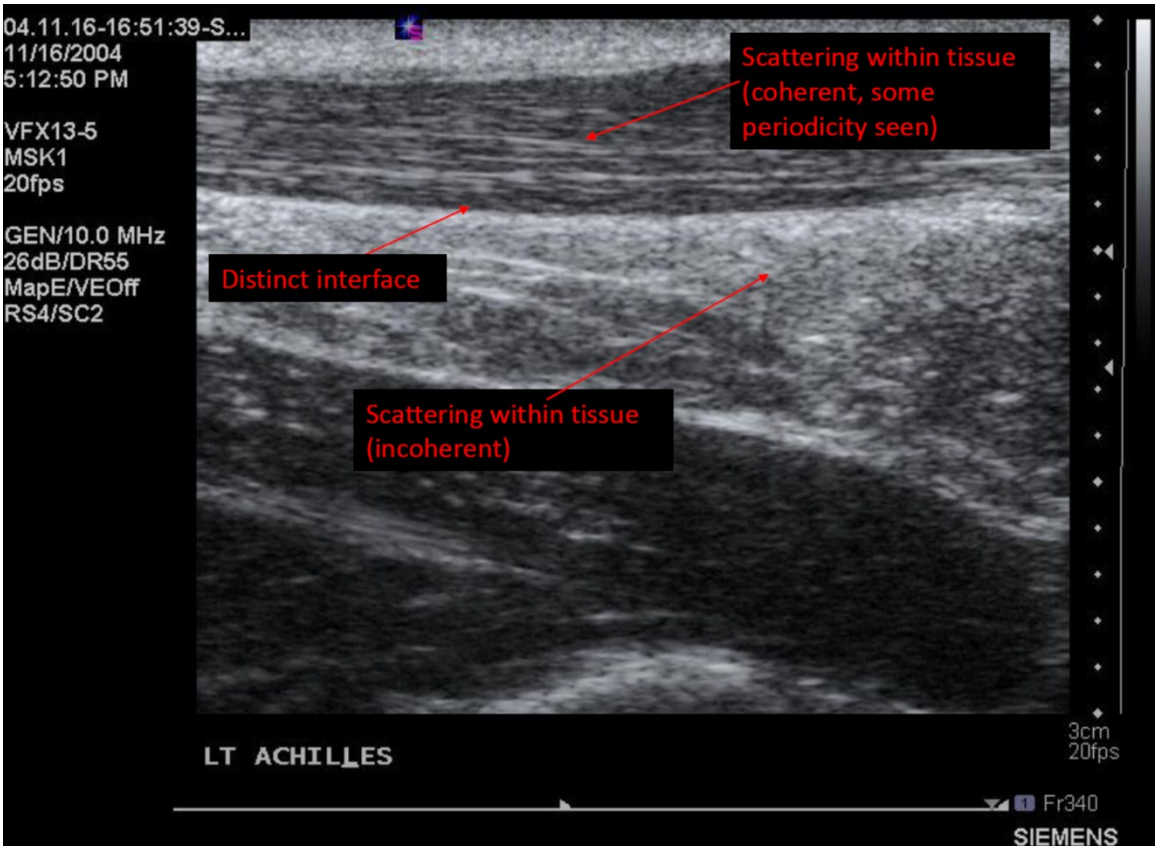

Fig. 2.10. A screen shot of human Achilles tendon. In the ultrasound image, the Achilles tendon has a laterally correlated speckle pattern as a result of the spatial organized scatterers, while in the surrounding tissue; the speckle pattern is granular since the scatterers are homogeneously distributed. (Biomedical Imaging and Biosignal Analysis Labarotory, University of Nebraska-Lincoln, 2012)

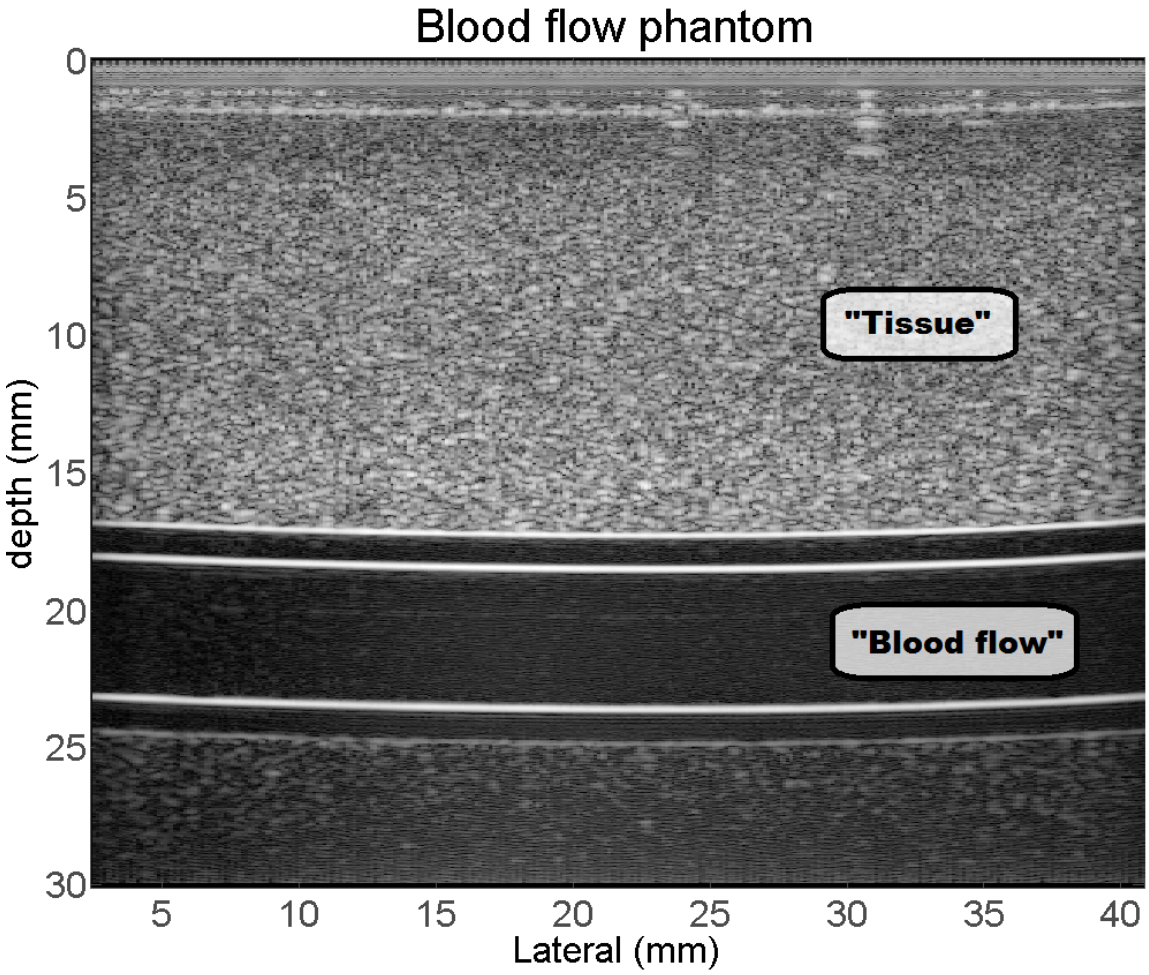

Fig. 2.11. A sample B-mode image of blood flow phantom. The area of blood flow is dark compared with surrounding tissue. After filtering and amplifying, speckle patterns in the dark area will be used for blood flow velocity estimation (Biomedical Imaging and Biosignal Analysis Labarotory, University of Nebraska-Lincoln, 2012).

2.4 Jugular veins anatomy/pathology

The jugular vein and its associated branches are the main vessels that drain blood flow from the head back to the heart. They are located next to the carotid artery and its associated branches in the neck. In ultrasound imaging, the jugular vein can be seen on top of the carotid artery, which is shown in Fig. 2.7. The jugular vein branches into two parts. The first part is called the internal jugular vein which collects blood from the inner

part of head (brain, deep in the face, etc.). The second part is called the external jugular vein which collects blood from the outer part of the head (outside of face, skin, etc.).

Dangerous jugular vein pathology occurs when the jugular vein is blocked by a blood clot, which is called jugular vein thrombosis. It is caused by various internal and external reasons, such as surgery and infections. When the blood is blocked by jugular vein thrombosis, high blood pressure may cause jugular vein rupture and lead to congestive heart failure (heart cannot pump enough blood for the rest of the body). Hemodynamic abnormalities are associated with internal jugular vein diseases. For example, in one study, blood flow velocity in patients with thrombosis was significantly lower than that in patients without thrombosis (Veryseller et al. 2010). If ultrasound blood flow measurement can estimate jugular vein blood flow velocities, then it is a potential method to predict and prevent jugular vein thrombosis. However, most of current methods for jugular vein blood flow velocity measurement, as described above in section 2.1, are based on the "Doppler" effect, which can only measure the axial component of blood flow velocity. The angle between the ultrasound beam and blood flow has to be manually set and used for angle correction during velocity estimation. Furthermore, errors in estimating the Doppler angle decrease the accuracy of blood flow velocity estimation, especially when the angle approaches 90^{o}. Other potential errors include spectral broadening of Doppler signals caused by the broad frequency spectrum of the transducer, which introduces bias to the blood flow velocity estimation (Gill 1985; Hein and O'Brien 1993). A limit to current ultrasound-based blood flow measurement techniques includes aliasing, which occurs when the maximum Doppler frequency is greater than one half of the pulse repetition frequency (PRF), and the aliasing limits the

maximum detectable velocity of Doppler based methods (Hein and O'Brien 1993). In this dissertation, we investigated the apparent speckle pattern of ultrasound blood flow images collected by different scanning velocities. A relationship between the blood flow velocity and the apparent speckle pattern was theoretically developed and tested by phantom and *in vivo* experiments. Results showed that this method is capable of resolving the direction and amplitude of two-dimensional blood flow simultaneously with less computational complexity than Doppler based methods. It provides a potential alternative way of jugular vein blood flow detection and thrombosis diagnosis.

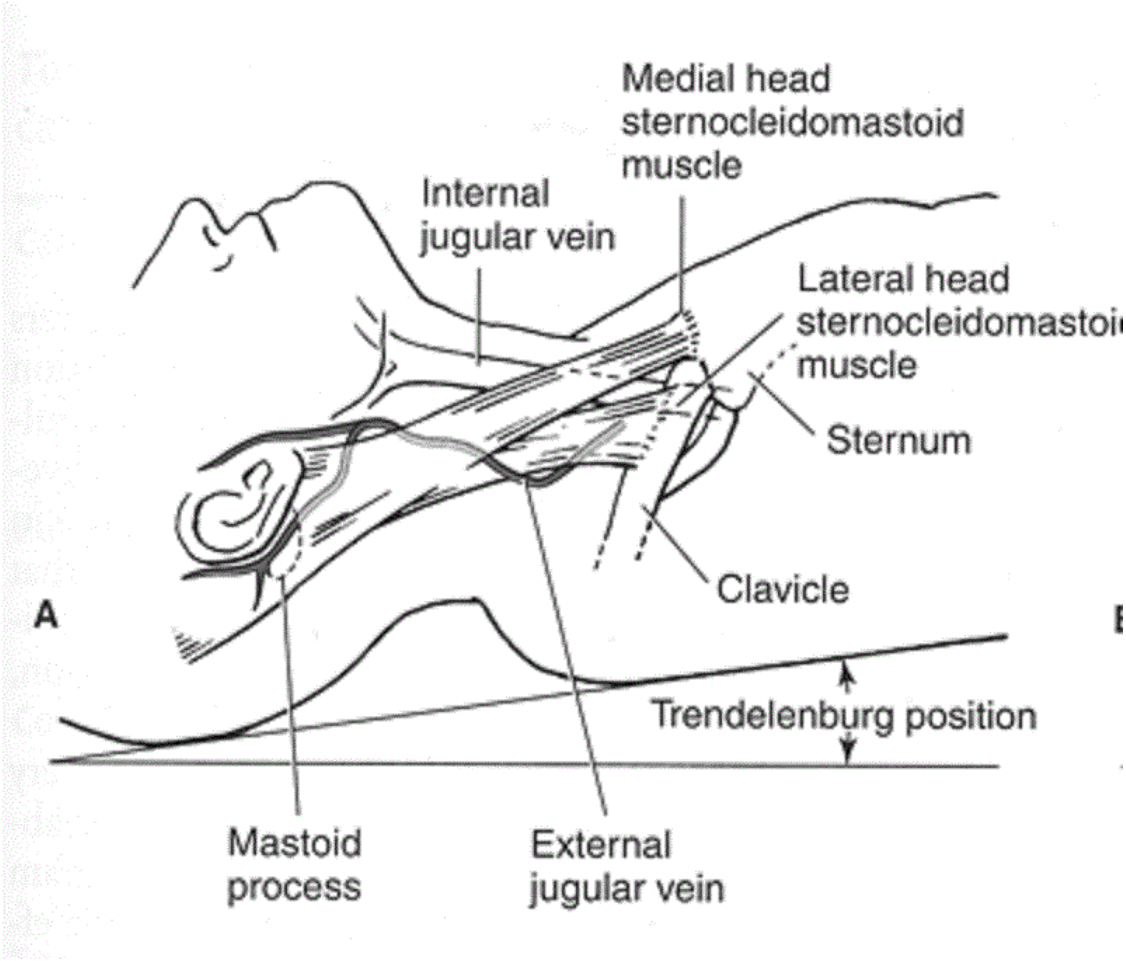

Fig. 2.12. Reprinted from Encyclopedia Britannica (http://www.britannica.com/EBchecked/topic/307668/jugular-vein) "Anatomy of jugular veins. The external jugular vein receives blood from the neck, the outside of the cranium and the deep tissues of the face, empty into the subclavian veins. The internal jugular vein, which unite with the subclavian veins to from the brachiocephalic veins, and drain blood from the brain, the face and the neck." (Encyclopedia Britannica).

Chapter 3

Optimization of Feature Tracking

3.1 Introduction

Feature tracking was first proposed by Roundhill in 1991 and performed accurately in one dimension (Roundhill 1991). Instead of dealing with the entire volume of image data, feature tracking selects discrete trackable locations in the data, which are called “features”. Directly tracking selected features permits estimation of the direction and velocity of target motion. This method significantly reduces data storage and increases computational efficiency (Kuo and Von Ramm 2008). Feature tracking was

extended to ultrasound 3-D velocity and motion measurement (Bashford and Von Ramm 1996; Morsy and Von Ramm 1999).

Most recently, to assess the performance of feature tracking in terms of estimation bias and standard deviation, it was directly compared with the conventional autocorrelation method. The results suggested that feature tracking exhibits a comparable estimation mean to the conventional commercial method, and a favorable estimation variance (Bashford and Robinson 2007).

Feature extraction is the first and crucial step in feature tracking. First, a candidate list of features is created based on applying a rule to the data (e.g., finding the locations of local maxima of the signal amplitude). Next, the candidate list is narrowed according to some criterion (e.g., the features must meet certain threshold amplitudes). Prior studies used an ad hoc approach to set thresholds based on experimental observation (Kuo and Von Ramm 2008; Bashford and Von Ramm 1996; Morsy and Von Ramm 1999; Bashford and Robinson 2007). Specifically, in (Bashford and Von Ramm 1996), an amplitude threshold was used to select features with amplitude above the average magnitude of the pulse-echo signal. Additionally, a width threshold was established to extract features with a certain breadth in the time domain. The width threshold was 1/4 to 1/3 of the wavelength corresponding to the center frequency of the transducer. In (Morsy and Von Ramm 1999), Morsy and von Ramm proposed different methods to select thresholds; the amplitude threshold H_{th} was determined by the equation:

$$H_{th} = \mu_A + C \cdot \sigma_A \tag{3.1}$$

where μ_A is the mean of the detected axial line, and σ_A is its standard deviation. C is a number used to control the value of H_{th}. Also, two width thresholds W_{min} and W_{max} were

selected. W_{min} represents a lower limit on the acceptable width of the axial segment while W_{max} represents an upper threshold on the axial segment width. The values used for W_{min} and W_{max} were 2 samples (0.3mm) and 11 samples (1.7mm). Based on these two thresholds, the candidate list of features was narrowed. Morsy and von Ramm found that by raising the thresholds, the number of available features declined. This work represented a step towards standardization of threshold selection, but was not fully developed.

Thus, to date not much attention has been paid to either the process by which trackable features are selected from the data, or the process by which the candidate list is narrowed. While both processes are clearly important, here we address the latter, i.e., we suggest the use of amplitude and width thresholds, and study the relationship between threshold selection and estimate performance. The reason that we are studying the latter process in this chapter is that we have previously shown that at least one feature (the local maxima) translates in correspondence with tissue motion (Bashford and Von Ramm 1996); rather than studying multiple processes at once, we wish to explore how thresholds affect the accuracy of the motion estimation.

The number of trackable features will decrease as the amplitude or width threshold increases. We hypothesize that with a higher threshold, the estimate standard deviation (error) will decrease. However, tracking fewer features would result in sparser spatial sampling of the flow field. Therefore, there should be a trade-off between spatial sampling of motion (number of trackable features) and the accuracy of estimation at each spatial location. If this hypothesis is true, it should be possible to find optimal thresholds

that maximize the estimator's accuracy (minimize the standard deviation) for a desired spatial sampling.

The purpose of this chapter is to compare feature tracking estimation standard deviation with varying width and amplitude thresholds. This analysis will be done in one-dimension.

3.2 Materials

3.2.1 Blood flow phantom

A commercial flow phantom (Optimizer RMI 1425, Gammex, Middleton, WI), was used to simulate blood flow. This phantom contains a tube (5mm inside diameter, 1.25 mm thickness) through which blood-mimicking fluid is pumped. The fluid has acoustic properties similar to blood (speed of sound 1550 m/s, density 1.03 g/cc). The tube is surrounded by tissue-mimicking material (speed of sound 1540 m/s, attenuation 0.5 dB/cm/MHz). A spherically focused 3.5 MHz transducer with F# = 3.0 (ratio of focal depth and transducer aperture diameter) and -6 dB bandwidth = 35% (Panametrics A382S, Waltham, MA) was mounted on a transducer stand and vertically directed at the blood flow phantom. The tube is oriented at a 40 degree angle to the horizontal, i.e., to the transducer face. Due to physical limitations combining the focal length of the transducer and the location of the tube interrogated past the pump, the flow was not guaranteed to be fully developed (parabolic) by the manufacturer; however, experiments (see Results section) showed that the detected flow was nearly parabolic.

The SNR in the experimental setup was 15.0 dB. The SNR was measured in the following manner. One thousand pulse-echo signals were acquired with the flow

phantom velocity set to zero. The average of the 1000 signals was calculated to estimate the mean signal. Then, for each signal, a noise signal was produced by subtracting the mean signal from the raw signal. The SNR was calculated by dividing the standard deviation of the mean signal by the standard deviation of the noise signal.

3.2.2 Data acquisition platform

A pulser/receiver (500PR, Panametrics, Waltham, MA) was used to excite the transducer. The phantom was set to constant velocity mode with velocities of 15, 30, 45, and 60 cm/s. The PRF was set at four times the effective Doppler frequency, given the phantom velocity and scan geometry. Our motivation for picking this PRF was to place the center of the resulting Doppler spectrum halfway between 0 Hz and PRF/2 Hz to avoid aliasing. The resulting PRFs were 2090, 4170, 6330, and 6720 Hz respectively. (The pulser in our lab has a maximum PRF of 6720 Hz, so the 60 cm/s data was taken at 3.2 times the effective Doppler frequency. This did not appreciably change the results.) Each data set consisted of 128 pulse-echo interrogations separated by a time interval of 1/PRF. Each pulse-echo signal consisted of 20.5 μs of data centered about and fully including the phantom tube. The echo signal was received by a dedicated 14-bit, 100 MHz A/D card (PXI-5122, National Instruments, Austin, TX). In feature tracking processing, only data corresponding to the tube (6.5 μs) was analyzed.

3.3 Methods

The data were filtered before further processing. Filtering in the time direction was performed with a 12^{th}-order Butterworth IIR band pass filter (-3dB cutoff frequencies 1.89 and 5.29 MHz). No initialization was used in the band pass filter and no

samples were discarded because the samples corresponding to the tube were at least several hundred samples from the start of the signal. In the ensemble ("slow time") direction, a 2nd-order Butterworth IIR high pass filter (wall filter) was designed (-3 dB cutoff frequency = 6.3% of PRF/2) to cancel stationary echoes, and applied to the data. No initialization was used in the wall filter because the first 10 samples were discarded.

3.3.1 Potential feature extraction

Estimates of the probability distribution functions for feature amplitude and width were made by forming histograms of detected local maxima over several data sets. Specifically, 20 datasets each containing 128 pulse-echo A-lines were examined for each estimate. A feature was detected by examining successive samples x_i along each line and looking for local maxima (peaks). If x_i satisfies

$$x_{i-1} < x_i \quad and \quad x_i > x_{i+1}, \tag{3.2}$$

then the location x_i was considered a feature, which can be seen in Fig. 3.1. The amplitude and full-width at half-maximum (FWHM) of the peak were then recorded to calculate the cumulative probability for each value.

3.3.2 Define feature thresholds

To extract the features for blood flow measurement, the potential features are examined to see if they meet amplitude (height) and time (width) thresholds. The thresholds were selected subjectively by manual inspection of several flow signals in Bashford's work in 2007, in which the height threshold roughly corresponded to the average magnitude of the flow signal and the width threshold was roughly 1/4 to1/3 of the wavelength (Bashford and Robinson 2007).

In this chapter, two sets of thresholds were chosen. The first set ("set 1") spanned the cumulative distribution of available features from 10 to 90% in multiples of 10% for both amplitude and width thresholds. In the second set ("set 2"), amplitude thresholds were chosen in even fractions of the mean energy (RMS) of the signal, while width thresholds were chosen in even fractions of the wavelength of the center frequency of the transducer.

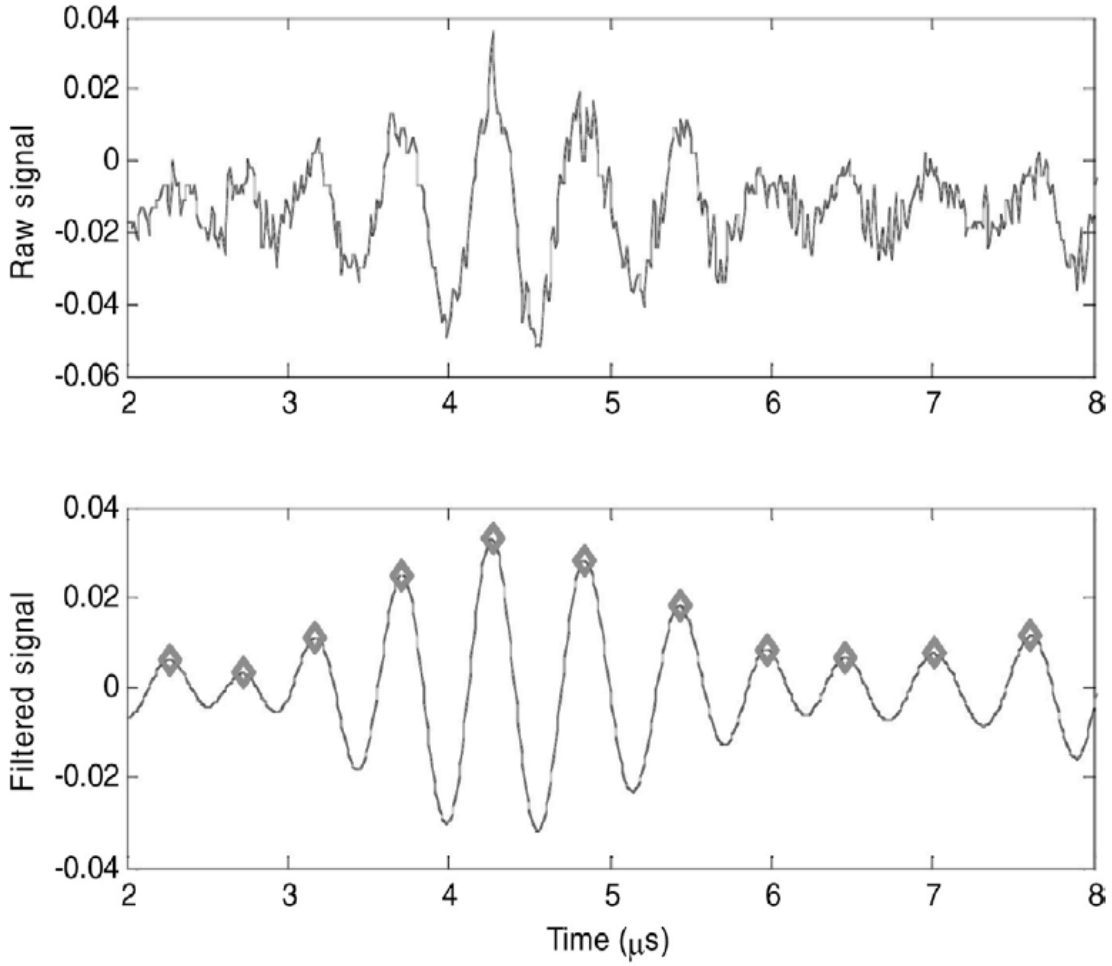

Fig. 3.1. Reprinted from Bashford et al. 2007. "A gradient search locates features in one dimension. Top, raw data of a 6-μs portion of an ultrasound echo signal from a string target. Bottom, filtered data overlaid with results of gradient search for feature location"(Bashford and Robinson 2007).

3.3.3 Blood flow velocity estimation using feature tracking

A portion of the RF signal corresponding to the tube location was selected for all features. Each feature was examined to see if it met an amplitude and time (width) threshold. Those features that remained were tracked across successive pulse-echo repetitions (i.e., eight adjoined lines separated in time by the PRF).

The location of the first local maximum that passes the thresholds was taken as the initial feature location. In subsequent pulse-echo signals, a feature was found by examining the data immediately around the location of the previous feature. The local maximum nearest the location of the previous feature was taken as the next feature location. After the initial feature, subsequent local maxima were not compared to threshold values. This process was repeated *N* times, where *N* is the number of flow samples acquired. A final variance threshold was applied in the following manner. The variance of the *N*-1 differences in peak locations was calculated. If the variance was above a certain threshold, the data set was not processed further for feature tracking. Then, the difference in sample location of the *N*th feature and the first feature was taken as the feature tracking estimate v (including a factor for time conversion):

$$v = \frac{(peak(N) - peak(1))}{N-1} \frac{cPRF}{2 f_s cos\theta} \tag{3.3}$$

where v is the estimated blood flow velocity, c is the sound velocity of ultrasound, PRF is the pulse repetition frequency of data collection, f_s is the sampling frequency and θ is the angle between blood flow and ultrasound beam axis.

To ensure that features were tracked across the entire tube, the diameter of the tube was divided into eight equal distances. At least 100 features were tracked at each of

these eight locations (depths) within the tube. The performance of feature tracking under these conditions was evaluated by calculating the mean velocity and standard deviation of the estimates.

3.4 Results

Histograms of the cumulative probability of the amplitude and width of the features are shown in Fig.3.2, for all velocities. Markers on each curve show the actual threshold values selected in our experiment for set 2. The set 1 values can be determined by noting where the cumulative probability curves cross the horizontal grid lines.

Graphs of the estimate standard deviation versus width thresholds are shown in Fig. 3.3. Fig. 3.4 denotes the standard deviation versus different amplitude threshold values. Graphs of the number of trackable features found in one dataset versus threshold values are shown in Fig. 3.5.

The mean estimated velocity throughout the tube is shown in Fig. 3.6, for all four velocity experiments. It was not possible to assume a particular flow profile *a priori*, so in order to compare the volume flow rate displayed on the phantom's controller with that which would be estimated by feature tracking, we adopted a quasi-numerical technique by integrating the mean velocity detected in the tube across a cross-sectional circle. That is, the cross-sectional area in the tube was divided into eight concentric sectors, each with a width of 1/8 of the tube's inner diameter. Each of the eight velocities v_i detected across the tube was assumed to correspond to one of the sectors S_i, thus representing a fraction of the entire volume flow. The flow rate was calculated as follow:

$$F = \sum_{i=1}^{8} (v_i \times S_i) \tag{3.4}$$

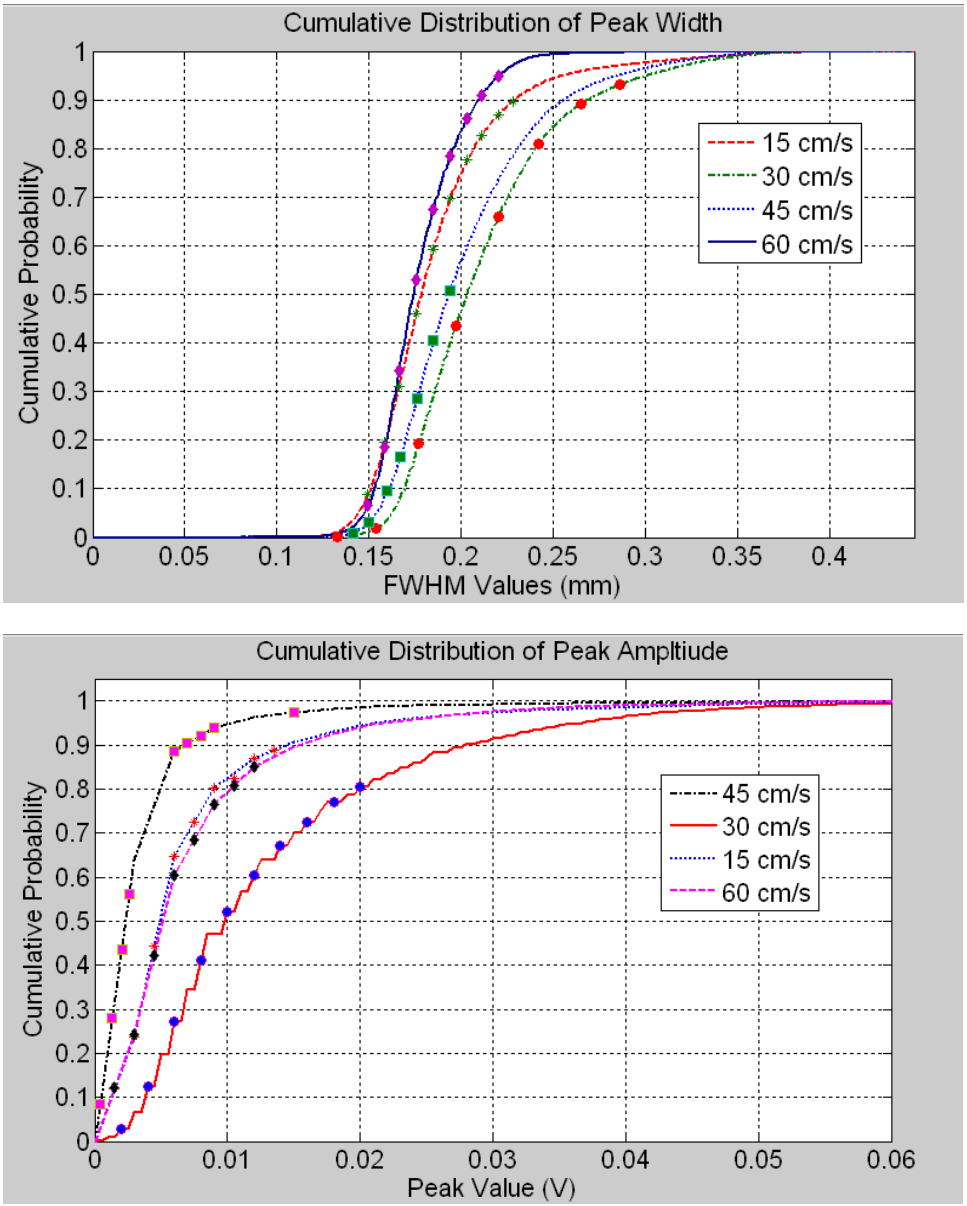

Fig. 3.2. Cumulative distribution of features. (Top) Feature amplitude, (bottom) feature width. Markers are shown where chosen threshold values for "set 2" were used in the experiments.

Using the mean velocity distribution denoted by Fig. 3.6, we calculated the flow rate for the velocity settings of 15, 30, 45, and 60 cm/s to be 1.1, 2.9, 4.2, and 5.5 ml/s respectively. These results are close (within 10%) to the values given by the phantom, which are 1.0, 2.6, 4.2, and 5.9 ml/s respectively. The motivation for comparing the

volume flow rates were to check the estimated mean velocities, which cannot be compared directly with the flow phantom setting since only one velocity for the tube is "selectable."

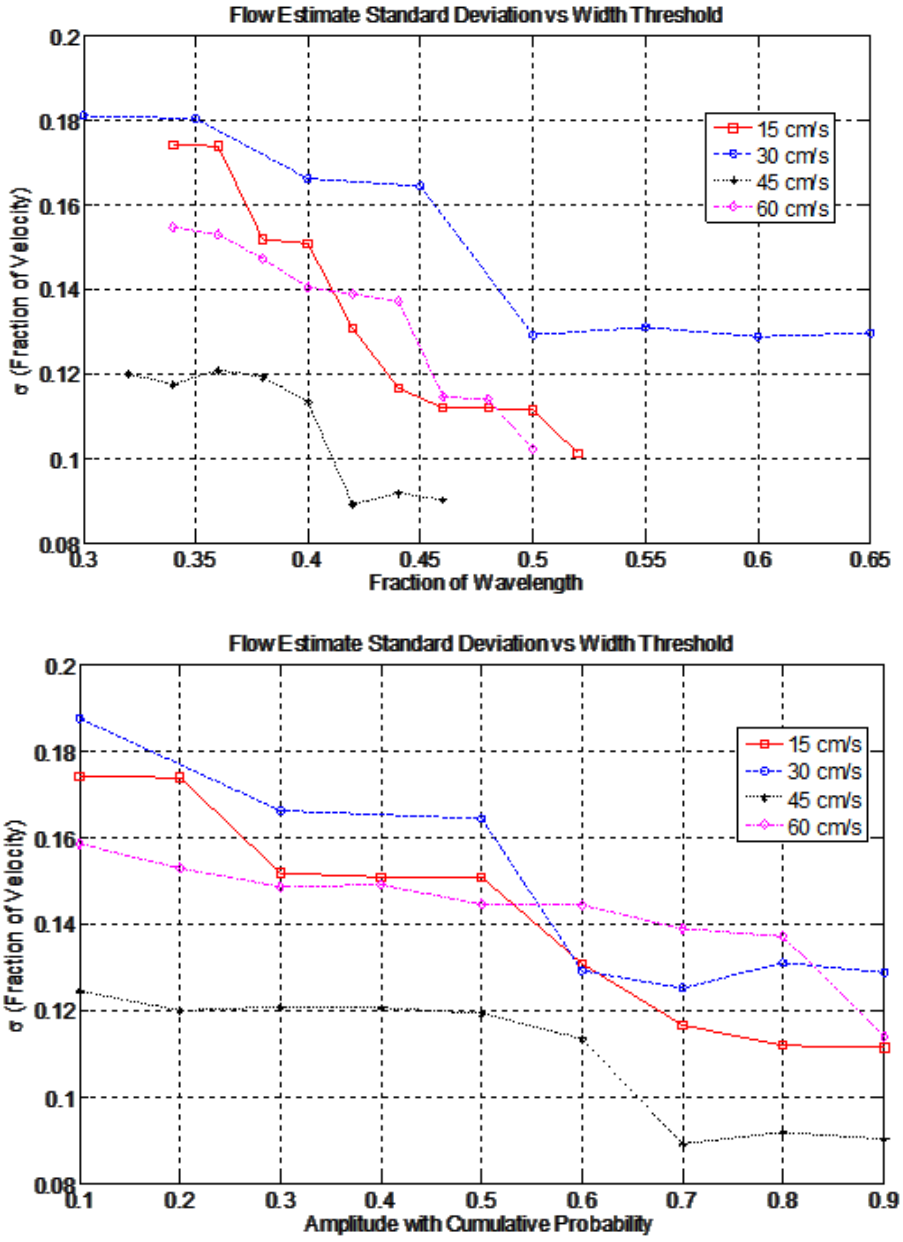

Fig. 3.3. Standard deviation versus width thresholds. Top, thresholds with constant interval of wavelength fractions ("set 2" thresholds); bottom, thresholds with constant interval of cumulative probability ("set 1" thresholds).

Another important note is that flow estimation is seen slightly outside the boundaries of the inner diameter of the tube in Fig. 3.6, because of convolution effects with the pulse length (detected full-width-half-maximum measured to be 1.3 microseconds or 1.0 mm).

3.5 Discussion

The relationship between estimation standard deviation and threshold value reveals that, as expected, the standard deviation decreases with higher threshold values. An interesting finding is that in the width threshold curves, a significant drop occurs at a certain point for most velocities. For example, in the top of Fig. 3.3, the 30 cm/s curve standard deviation remains between 0.16 and 0.18 of the velocity (between 4.8 and 5.4 cm/s) up to a fraction of a wavelength of about 0.45. At that point, the curve suddenly drops to about 0.13 of the velocity (3.9 cm/s), which is an improvement of over 25%. The same or close behavior can be seen in the other velocities as well. For all four velocities, this transition point occurs at a threshold between 0.40 and 0.45 of a wavelength. This drop suggests that a nonlinear relationship exists between estimate standard deviation and threshold selection. The reason for this sudden drop may be related to the distribution of the sizes of features within the speckle data set. However, a user can presently take advantage of this transition point to minimize estimate variance while preserving flow field coverage over time as explained below.

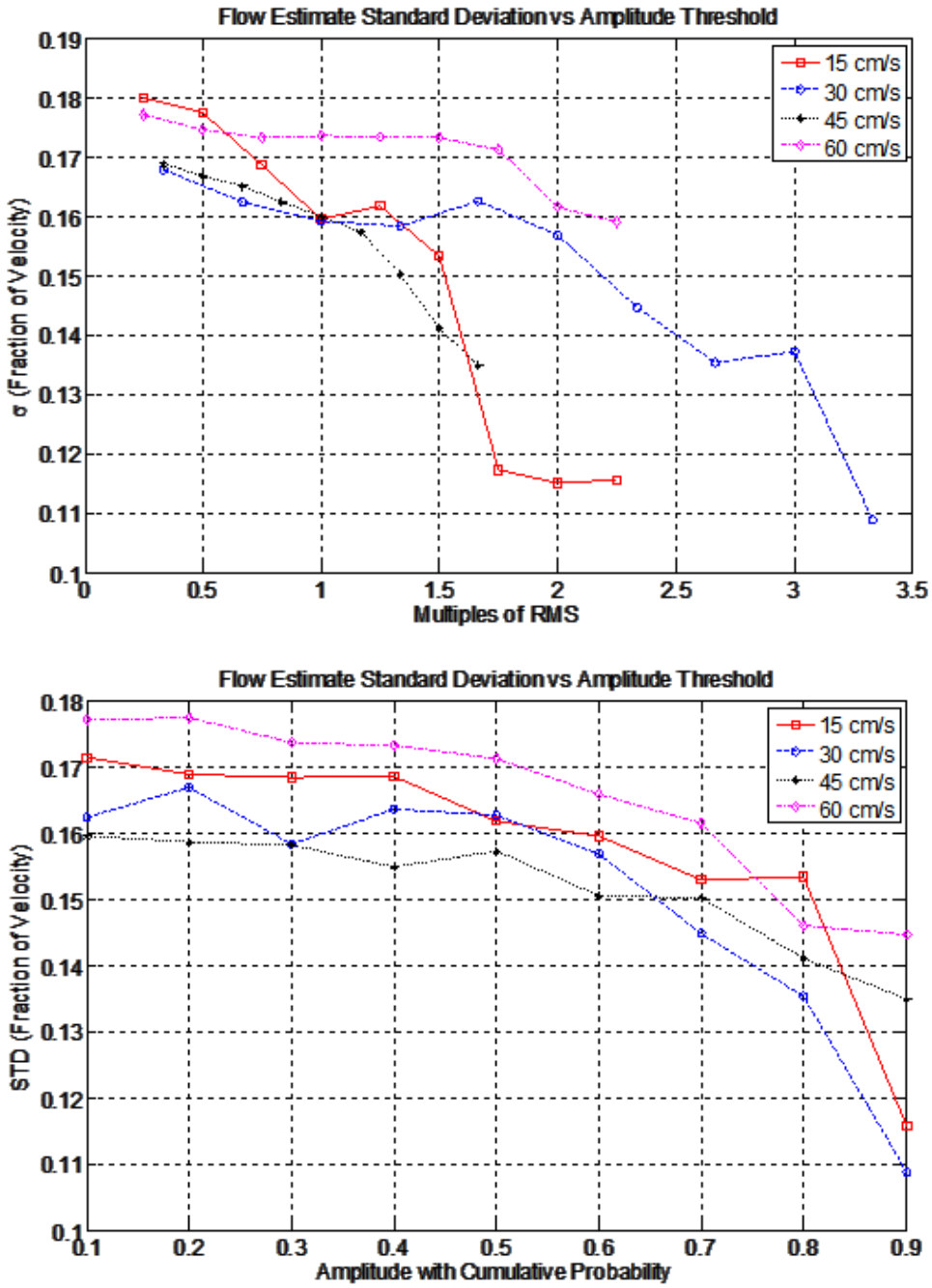

Fig. 3.4. Standard deviation versus amplitude thresholds. Top, thresholds with constant intervals of RMS widths; ("set 2" thresholds); bottom, thresholds with constant interval of cumulative probability ("set 1" thresholds).

The relationship between amplitude threshold and standard deviation denoted by Fig. 3.4 is different, with no consistent behavior or transition point when thresholds are viewed as multiples of RMS. However, from Fig. 3.4 (bottom), the standard deviation

curves are markedly similar when comparing thresholds chosen across the cumulative distribution.

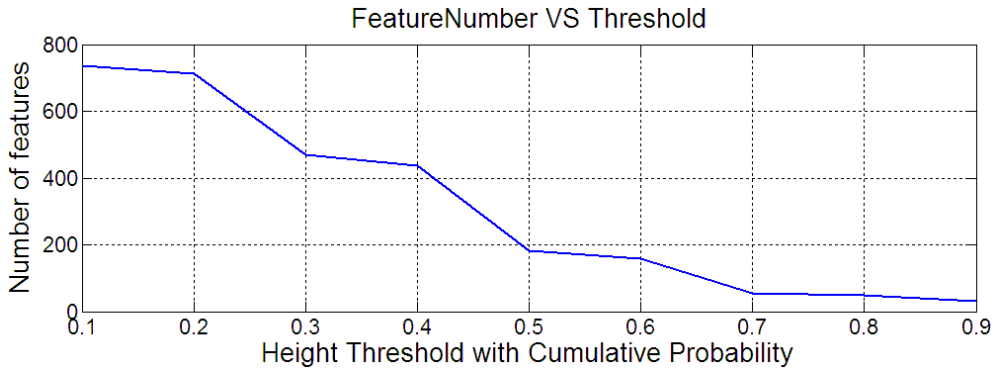

Fig. 3.5. Number of trackable features versus amplitude threshold values.

From the relation of standard deviation and threshold, we can generally say that greater thresholds give a better estimation through a lower standard deviation. The range of potential improvement can be significant. For example, the maximum and minimum standard deviations in the 30 cm/s curve on Fig. 3.4 are 5.04 cm/s and 3.26 cm/s, an improvement of over 35%.

The number of trackable features decreases with an increase of threshold values, which is shown in Fig. 3.5. This is important as it shows how finely the "flow estimate space" in the tube will be sampled. For 1D estimation, we are sampling across a line running transverse to the tube in the ultrasound beam direction. Higher thresholds result in fewer trackable features, meaning sparser coverage of the flow estimate space. The benefit of a higher threshold is a smaller estimate standard deviation, which translates to higher accuracy. On the other hand, a smaller threshold gives a greater number of trackable features, meaning more coverage of the flow space, but greater estimate standard deviation which translates to less accuracy. The required sampling relates to the expected spatial flow field correlation (Schlaikjer et al. 2004).

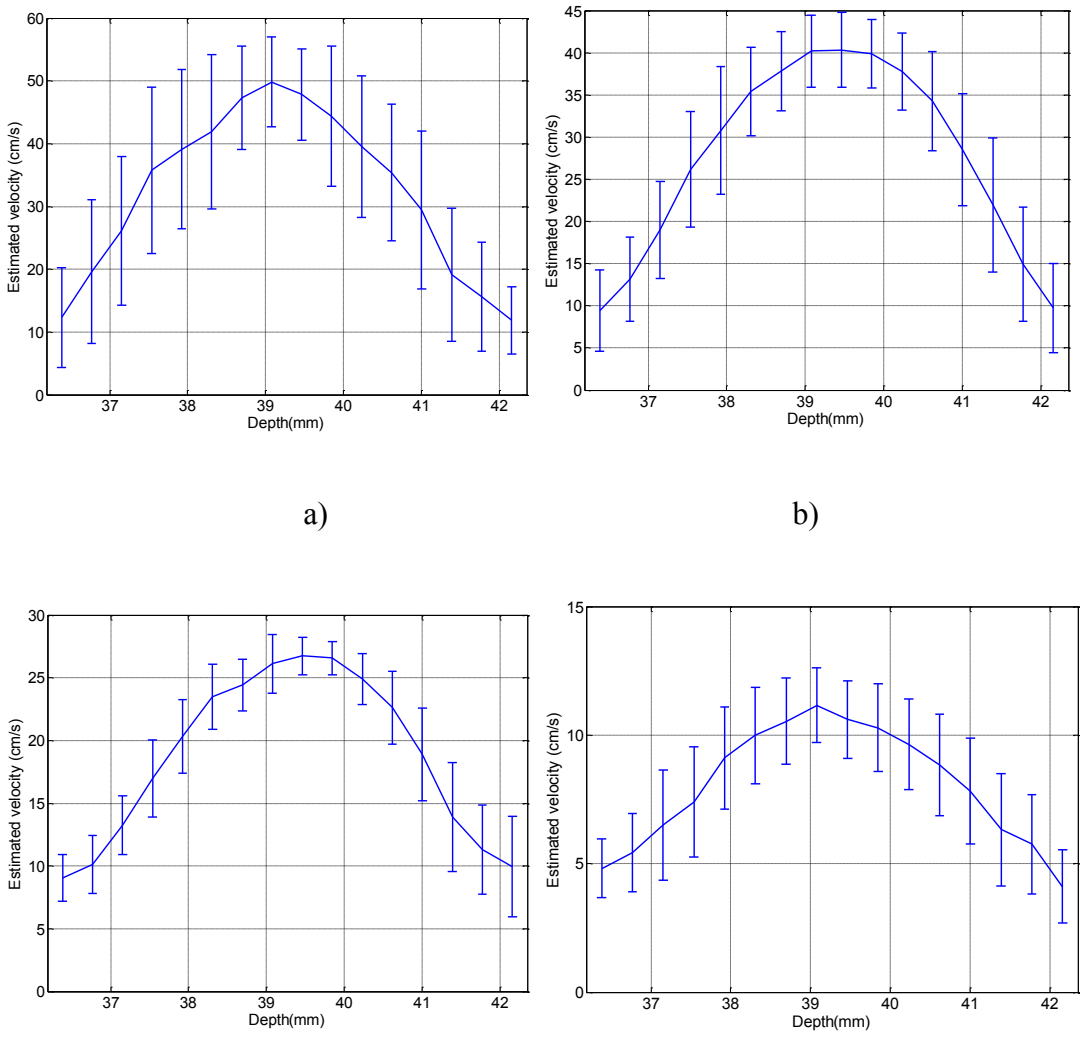

Fig. 3.6. Estimated velocity across the tube. (a)15 cm/s, (b) 30cm/s, (c) 45 cm/s, (d) 60 cm/s.

These graphs may help the interested user select optimal thresholds for a particular application. For example, the data shown in Fig. 3.3 suggest that rapid improvement (decrease) in standard deviation occurs while increasing the threshold until a particular transition point, where not much further improvement can be expected. In particular, using width thresholds at about 40-45% of the center frequency wavelength gives optimal results by taking advantage of the rapid decrease in standard deviation

while avoiding the region where estimation variance stays relatively constant. Fig. 3.4 suggests that using the largest practical amplitude threshold provides the lowest estimate variance. These selections must be balanced with the desired sampling of the flow space and desired time to acquire estimates. Although (as noted above) a comprehensive study of space/time coverage of features in the flow field as functions of threshold selection and flow profile has not been done, the current results can help those applications with some *a priori* known flow profiles. If the flow application is in an area that is not expected to vary widely throughout the flow space, such as plug flow, then higher thresholds with less flow field sampling and higher accuracy are preferable. On the other hand, if the flow application is expected to have a greater variance across space, such as turbulent flow, lower thresholds would be better for sufficient coverage of the flow field. It should be noted that another factor in this process is time to acquire samples. If more time is available to collect feature tracking data, then one can afford to "wait" for a sufficient number of thresholded features to appear. Therefore, taking into account the factors of desired spatial flow field coverage, desired flow estimation accuracy (variance), and desired time to complete flow sampling, a user can optimize the feature tracking algorithm for a particular application.

3.6 Conclusion

This chapter investigated the relationship between feature tracking estimation performance and feature threshold values. The number of trackable features decreases with increasing thresholds. The decrease of standard deviation with width thresholds suggests that an optimal width threshold occurs at about 40-45% of the center frequency wavelength. The decrease of standard deviation with amplitude thresholds does not

contain a similar type of transition point. Combining the relationship between the number of trackable features and estimate standard deviation, users may select preferred threshold values according to the specific flow application. With a judicious choice of thresholds, estimate standard deviation can be decreased 20-35%. Further study should include the extension of this analysis to multiple dimensions, as well as a cross-analysis (simultaneous varying of amplitude and width thresholds) to evaluate flow estimation performance. Also, the relationship between flow field coverage (feature existence) in space and time for different flow profiles should be examined.

Chapter 4
Resolving Lateral Blood Flow based on Speckle Size Estimation

4.1 Introduction

Conventional (Doppler-based) blood flow velocity measurement methods using ultrasound are capable of resolving the axial component (i.e., that aligned with the ultrasound propagation direction) of the blood flow velocity vector. However, these methods are incapable of detecting blood flow in the direction normal to the ultrasound beam. In addition, these methods require repeated pulse-echo interrogation at the same spatial location. A new method is introduced in this chapter, which estimates the lateral

component of blood flow within a single image frame using the observation that the speckle pattern corresponding to blood reflectors (typically red blood cells) stretches (i.e., is "smeared") if the blood is moving in the same direction as the electronically-controlled transducer line selection in a 2D image. The situation is analogous to the observed distortion of a subject photographed with a moving camera. In this chapter, the relationship between speckle size and blood flow velocity is investigated with both simulated flow data and measurements from a blood flow phantom. The observed results from this investigation include: 1) when the blood flow velocity is much greater than the "scan velocity" (spatial rate of A-line acquisition), the velocity will be significantly underestimated because of speckle decorrelation due to quick blood movement out of the ultrasound beam; 2) modeled flow gradients increase the average estimation error from a range between 1.4% and 4.4%, to a range between 4.4% and 6.8%; 3) estimation performance in a blood flow phantom where both flow gradients and random motion of scatterers are present increase the average estimation error to between 6.1% and 7.8%. Initial attempts at a multiple-scan strategy for estimating flow by a least-squares model suggest the possibility of increased accuracy using multiple scan velocities.

4.2 Materials

Both simulated and phantom blood flow data were collected. Data were simulated with and without lateral flow gradients (flow profiles). Four scan velocities were used in each experiment, the details of which follow.

The experimental setup for collecting blood flow data from the blood flow phantom is briefly described here. A commercial flow phantom (Optimizer RMI 1425,

Gammex, Middleton, WI), was used to simulate blood flow. This phantom contains a tube (5 mm inside diameter, 1.25 mm thickness) through which blood-mimicking fluid is pumped. The fluid has acoustic properties similar to blood (speed of sound 1550 m/s, density 1.03 g/cc). The tube is surrounded by tissue-mimicking material (speed of sound 1540 m/s, attenuation 0.5dB/cm/MHz).

4.2.1 Siemens SONOLINE Antares

The V13-5 transducer (192 elements, 9.5 MHz center frequency, the width and height of each element is 0.176 mm and 2.5 mm, the kerf (distance between two adjacent elements) is 25 μm and the transducer has an overall lateral aperture size as 3.38 cm) of a SONOLINE Antares Ultrasound Imaging System (Siemens Medical Solutions, Ultrasound Division, Issaquah, WA) was used for data acquisition. The tube is parallel to the surface of transducer, so only lateral flow data were collected. The Axius Direct Ultrasound Research Interface (URI) was employed to transfer ultrasound data (post-beamformation but before any downstream processing) to a computer for further analysis.

4.2.2 Field II simulation

To investigate the effects of flow gradient on speckle size estimation, we used the Field II simulation (Jensen and Svendsen 1992; Jensen and Munk 1996). As described by Jensen, “Field II is a program for simulating ultrasound transducer fields and ultrasound imaging using linear acoustics. The program uses the Tupholme-Stepanishen method for calculating pulsed ultrasound fields. The program is capable of calculating the emitted and pulse-echo fields for both the pulsed and continuous wave case for a large number of

different transducers. Also any kind of linear imaging can be simulated as well as realistic images of human tissue" (Jensen 2011).

To simulate blood flow data with and without a flow gradient, two flow conditions were simulated: the first had a parabolic velocity distribution in the flow which produces a similar lateral gradient to the flow velocity in the blood flow phantom. The parabolic flow has a velocity distribution as (4.1),

$$V_f = V_{\max}(1-\left(\frac{r}{R}\right)^2) \tag{4.1}$$

Where V_{max} is the maximum velocity in the vessel, r represents the distance from the vessel longitudinal axis and R represents the radius of the vessel, which is 5 mm. The flow gradient is then calculated as (4.2),

$$Flow\,Gradient = \frac{\partial V_f}{\partial r} = -2V_{\max}\frac{r}{R^2} \tag{4.2}$$

The second condition had a constant flow velocity distribution throughout the tube, simulating plug flow. The parameters of the ultrasound transducer and blood flow phantom were set the same as the commercial machine used in blood flow phantom data collection [See Table 4.1].

4.3 Methods

4.3.1 Speckle size calculation

In 2001, a patent suggested a technique of blood flow measurement which takes into account the observed stretching of the speckle pattern when viewed on a scanner whose line order was in the same direction as the moving blood (Hamilton et al. 2001).

The patent suggested a transform could be developed by comparing speckle size under conditions of no blood flow movement, with-scan movement, and against-scan movement. Such a transform was not developed in the patent.

TABLE 4.1. PARAMETERS OF TRANSDUCER AND BLOOD FLOW PHANTOM USED IN SIMULATION.

Transducer				**Blood Flow Phantom**	
Center Frequency	6.15 MHz	Number of Elements	192	Speed of Sound	1540 m/s
Element Height	2.5 mm	Focal Depth	20 mm	Depth of Tube	20 mm
Element Width	0.176 mm	Sampling Frequency	40 MHz	Diameter of Tube	5 mm
Kerf	25 μm			Flow Direction	Parallel to the surface of transducer

The second-order statistics of speckle in ultrasound B-scans was investigated in (Wagner et al. 1983). In that paper, a speckle "size" definition was proposed based on the autocovariance function (ACVF) of the speckle. In this chapter, we use a similar metric for speckle size: namely the full-width-half-maximum (FWHM) of the ACVF of a region-of-interest (ROI) in the US B-mode image, shown in Fig. 4.1. It can be estimated by the equation:

$$ACVF_{XX}(lag) = \frac{Sum((X(:,1:(end-lag)-) - \overline{X}).\times(X(:,(lag+1):end) - \overline{X}))}{N} \tag{4.3}$$

where X is the matrix of an ROI, $\overline{X}$ is the mean values of X, lag is the position shift with ranges from 0 to the width of the ROI, and N is the number of pixels included in the sum operation.

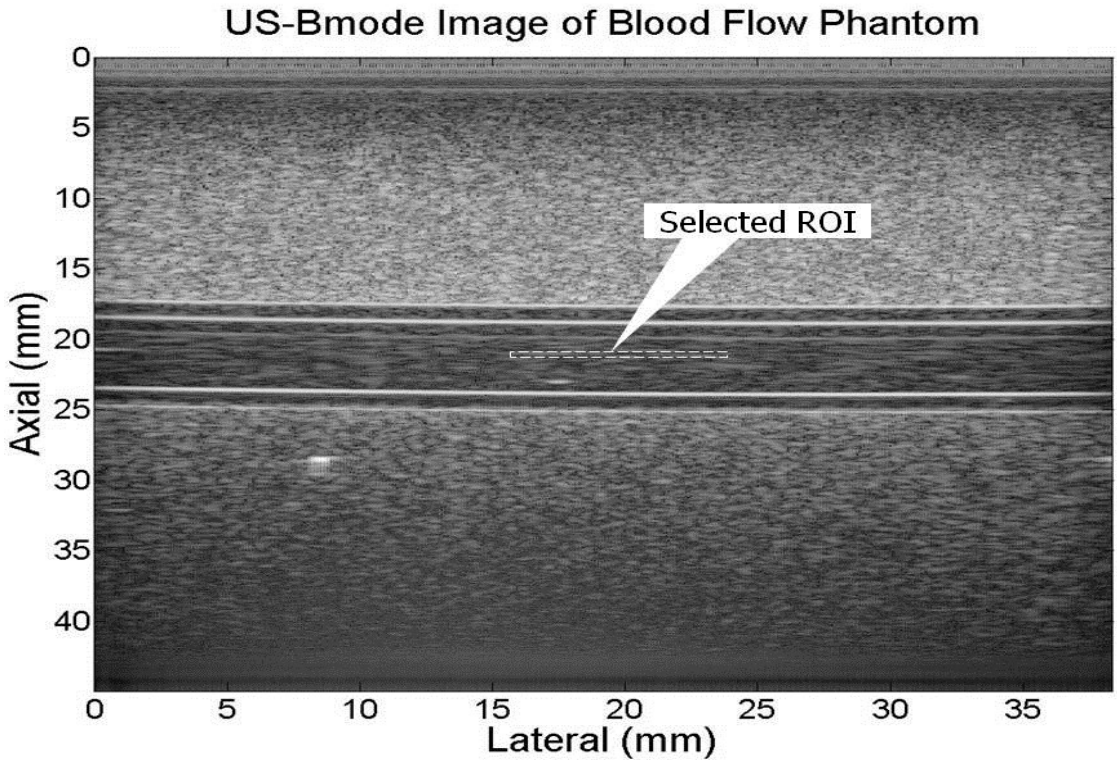

Fig. 4.1. Region-of-interest (ROI) which is the area in the dashed white line is selected from every US B-mode image of the blood flow phantom. It has a width of 50 pixels and height of 20 pixels, corresponding to 6.17 mm × 0.385 mm.

In general, a preferred algorithm would measure the lateral size of speckle corresponding to relative movement of matter in a subject under study, such as blood flow or tissue motion. Depending on the scan sequence direction, speckle corresponding to moving targets or matter will either expand or contract in the direction of motion (Hamilton et al. 2001). Comparing the expanded/compressed size relative to speckle corresponding to stationary targets potentially allows quantitative lateral flow velocity measurement.

In this chapter we call the "scan velocity" the spatial rate at which individual ultrasound A-lines are collected laterally across the transducer. When the scan velocity is greater than the blood flow velocity, the scanning geometry is shown in Fig. 4.2. The

blood flow is parallel to the surface of the transducer. Both scanning and blood flow have the same direction represented by solid arrows. D_1 is the distance traveled by blood flow (represented by a single scatterer) in one pulse period, which can be calculated as:

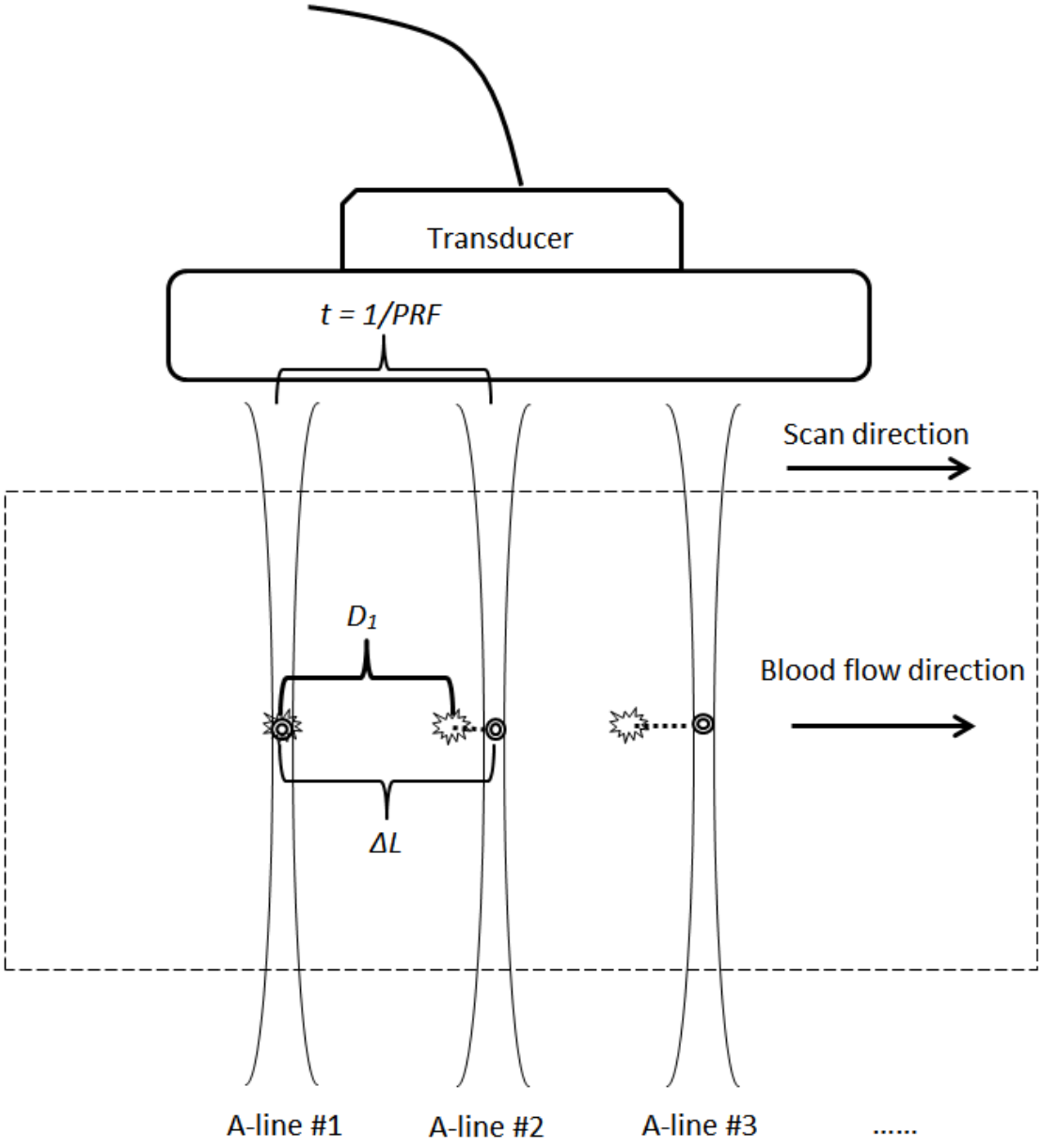

Fig. 4.2. Scanning geometry when the surface of transducer is parallel to the blood flow. "Burst" makers show actual position of an individual scatterer, and round circles show where the scatterer is interpreted as existing in the space.

$$D_1 = \frac{V_f}{PRF} \tag{4.4}$$

where V_f is the velocity of blood flow and PRF is the pulse repetition frequency. Then a stretch factor SF for different blood flow velocities can be derived as:

$$SF = \frac{\Delta L}{\Delta L - D_1} = \frac{1}{1 - \frac{V_f}{V_s}} \tag{4.5}$$

This stretch factor should be the factor the $ACVF$ changes (compresses or expands) due to the relationship between scan rate and blood flow velocity. If we denote the speckle size of non-flow condition as $FWHM\text{-}ACVF_0$, and the speckle size of blood flow is $FWHM\text{-}ACVF_v$, then SF of different blood flow velocities can also be represented as:

$$SF = \frac{FWHM - ACVF_v}{FWHM - ACVF_0} \tag{4.6}$$

Thus, a relationship between the blood flow velocity and speckle size can be derived when we combine (4.5) and (4.6) together, which gives us:

$$\frac{FWHM - ACVF_v}{FWHM - ACVF_0} = \frac{1}{1 - \frac{V_f}{V_s}} \tag{4.7}$$

Furthermore, a linear relationship will exist between the blood flow velocity and the ratio of speckle size between non-flow condition and dynamic blood flow when we take the inverse of both sides of (4.7), which is:

$$\frac{FWHM - ACVF_0}{FWHM - ACVF_s} = 1 - \frac{V_f}{V_s} \tag{4.8}$$

When the scan velocity is less than the blood flow velocity, the relationship between speckle size and blood flow velocity can be derived in a similar way. The result is:

$$\frac{FWHM - ACVF_0}{FWHM - ACVF_s} = \frac{V_f}{V_s} - 1 \tag{4.9}$$

4.3.2 Scanning setting and data acquisition

The scanning geometry is shown in Fig. 4.2. As shown in Fig. 4.1, the ROI is selected from the B-mode image, completely inside of an area corresponding to the phantom "blood vessel". The axial center of the ROI corresponds to the center of the vessel, and the axial width is chosen with respect to the amount of flow gradient desired in the data. In Fig. 4.1, a relatively narrow (axially) ROI is chosen, such that the flow gradient is relatively small and thus the flow velocity spectrum is relatively narrow. In experiments where a broader flow spectrum is desired (i.e., more flow gradients), a wider (axially) ROI may be chosen.

For the SONOLINE Antares ultrasound imaging system, the "Carotid" exam mode was used to scan the flow phantom. The focal depth was 2 cm where the tube is located in the phantom. The total imaging depth ranged from 3.5 to 5.5 cm (starting at 0 cm). In each image, 312 lines were collected. The URI includes header information to

allow researchers access to key parameters of the experimental setup. The frame rate can be found in the header information. Since 312 lines were collected in each image, the PRF can then be calculated by multiplying the number of lines with the frame rate. The number of lines per centimeter was found to be 81.0 lines/cm. The space interval ΔL between each line can then be calculated as the reciprocal of line density, which is 0.1234 mm, which is shown in Fig. 4.3.

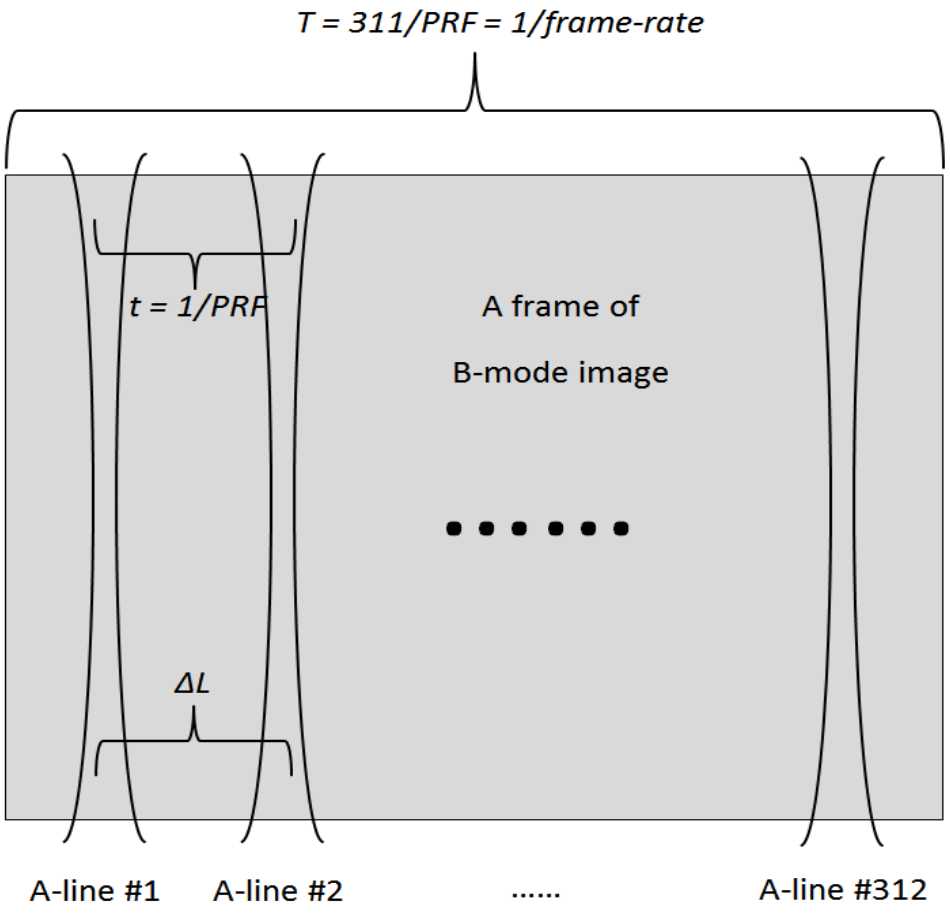

Fig. 4.3. A frame of B-mode image (collected within time *T*) contains 312 A-lines. The time interval between each pair of A-lines is the inverse of the PRF and the lateral space interval between each pair of A-lines is *ΔL*.

Thus, the "scan velocity", that is, the rate at which new ultrasound lines are formed in space, can be derived as:

$$V_s = \Delta L \times PRF \tag{4.10}$$

For each PRF setting, ten B-mode images of the flow phantom with velocity ranging from 10 to 100 cm/s were collected for study where the scan direction was the same as the blood flow. Furthermore, ten images of non-flow condition were collected at the same time. In each image, a region of interest (ROI) was selected from the middle of the tube, with an axial length of 20 pixels (0.39 mm) and a lateral length of 50 pixels (6.2 mm), as shown in Fig. 4.1. This ROI, which is represented as X in (4.3), was then used to calculate the mean and standard deviation of speckle size. The measured speckle size was used to estimate the flow velocity using (4.8) and (4.9). In addition, Field II simulation was also used to simulate blood flow data with and without a flow gradient for further experiment.

4.3.3 General least-squares optimization

From the results of our previous studies (Xu and Bashford 2009a; Xu and Bashford 2009b), we also hypothesized that different scan velocities will have effects on estimation performance. Generally, when the difference between scan velocity and blood flow velocity becomes large, the possibility of speckle decorrelation increases significantly since the blood flow moves out of the ultrasound beam more quickly. Thus, four PRFs (1492, 3241, 4862 and 6483 Hz), corresponding to four different scan velocities, were used in our experiment. For flow velocities ranging from 10 to 100 cm/s, data were collected using four different scan velocities. Our studies showed that the estimation performance varies according to scan velocity. Thus, potentially there is an optimal estimation incorporating different scan velocities. One of the ways to do this is to

assign weighting coefficients to the velocity estimations made by different scan velocities.

A general least–squares method (Lay and Stade 2005) was used to model this optimal solution, which can be represented by the formula as follows:

$$EV \times W = V \tag{4.11}$$

where EV represents the matrix of estimated velocities; each column contains different estimated results for the blood flow phantom ranging from 10 to 100 cm/s by a certain scan velocity. Since four scan velocities were used in our experiment, the matrix EV contains four columns, thus, its dimension is 10 × 4. The vector V represents actual velocities set to the blood flow phantom, which is a 10 × 1 vector. W is the vector of weighting coefficients we are seeking during the least-square modeling. It is a 4 × 1 vector where each element represents the weighting of estimation by each scan velocity. This least-square model finds the matrix W that minimizes the estimation error $||V - EV \times W||$.

4.4 Results

The stretch effect of the speckle between a non-flow condition (stationary) and flow conditions is shown in Fig. 4.4. From the graph, it can be seen that the speckle pattern of moving blood-mimicking material is stretched significantly compared with the non-flow condition. Furthermore, the stretch factor decreases as the absolute difference between flow velocity and scan velocity increases.

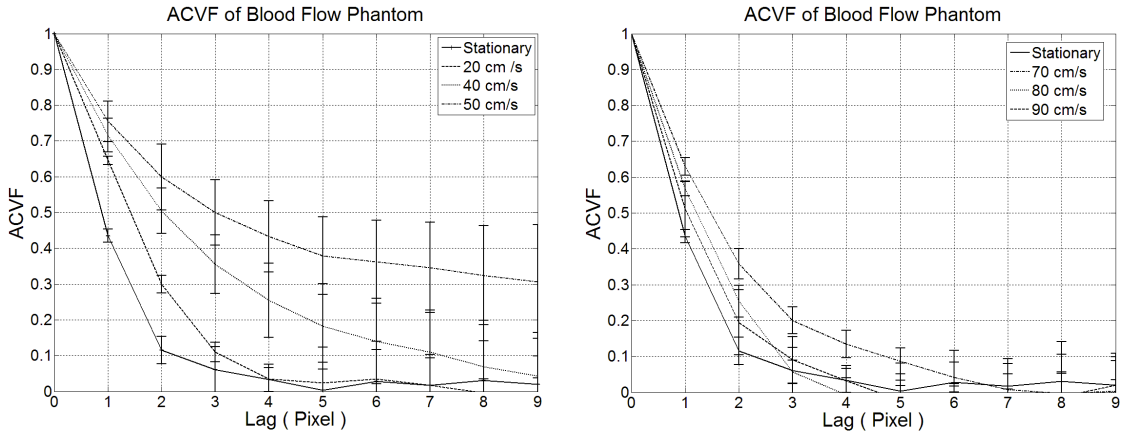

(a) (b)

Fig. 4.4. ACVF of blood flow phantom (scan velocity equals 64.8 cm/s). (a) Scan velocity is greater than the blood flow velocity; (b) Scan velocity is less than the blood flow velocity. Error bars show +/- one standard deviation.

The relationship between the reciprocal of stretch factor and flow velocity indicated by (4.8) and (4.9) is plotted in Fig. 4.5, Fig. 4.6 and Fig. 4.7. To investigate the effects of flow gradient on speckle size estimation, we started with simulation data in which the flow velocity is constant all over the tube. The results are shown in Fig. 4.5. It can be seen that the experimental data fit well to the theoretical lines when there is no velocity gradient in the flow. From part (a) of Fig. 4.5, when the flow velocity exceeds 40 cm/s, the experimental reciprocal stretch factor deviates from theoretical values and stays between 1.3 and 1.5 for the remaining flow velocities.

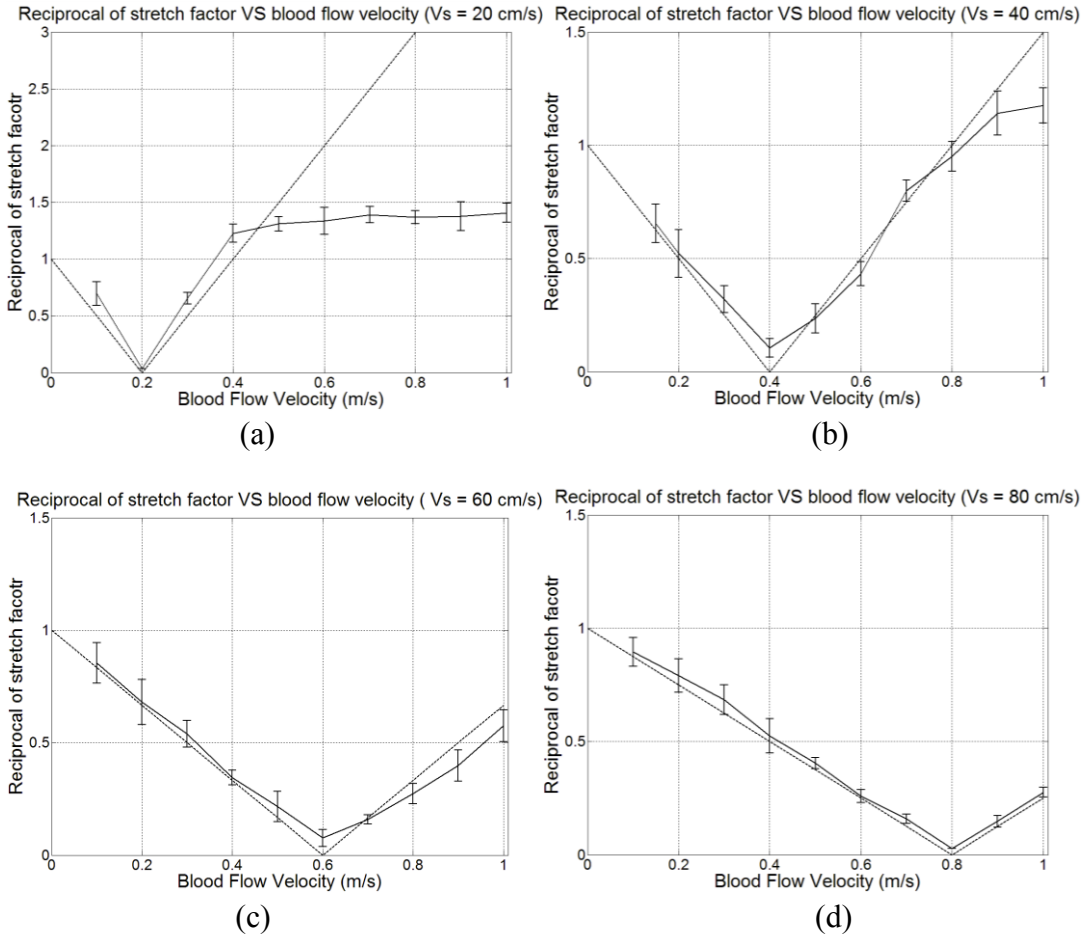

Fig. 4.5. Reciprocal of stretch factor with standard deviation (without flow gradient). Dashed lines are theoretical lines represented by (2) and (3). (a) Scan velocity is 20 cm/s, (b) Scan velocity is 40 cm/s, (c) Scan velocity is 60 cm/s, (d) Scan velocity is 80 cm/s.

Fig. 4.6 shows the relationship between stretch factor and simulated blood flow velocity when the simulated data include flow gradients. Compared with the results where there is no flow gradient in the tube, the deviation of experimental and theoretical values is more significant. The errors still exist when the scanning velocity is low, which can be seen in part (a) of Fig. 4.6. Moreover, in part (b) and (d), the reciprocal of stretch factors are overestimated compared with theoretical values when the flow velocity is less than the scan velocity.

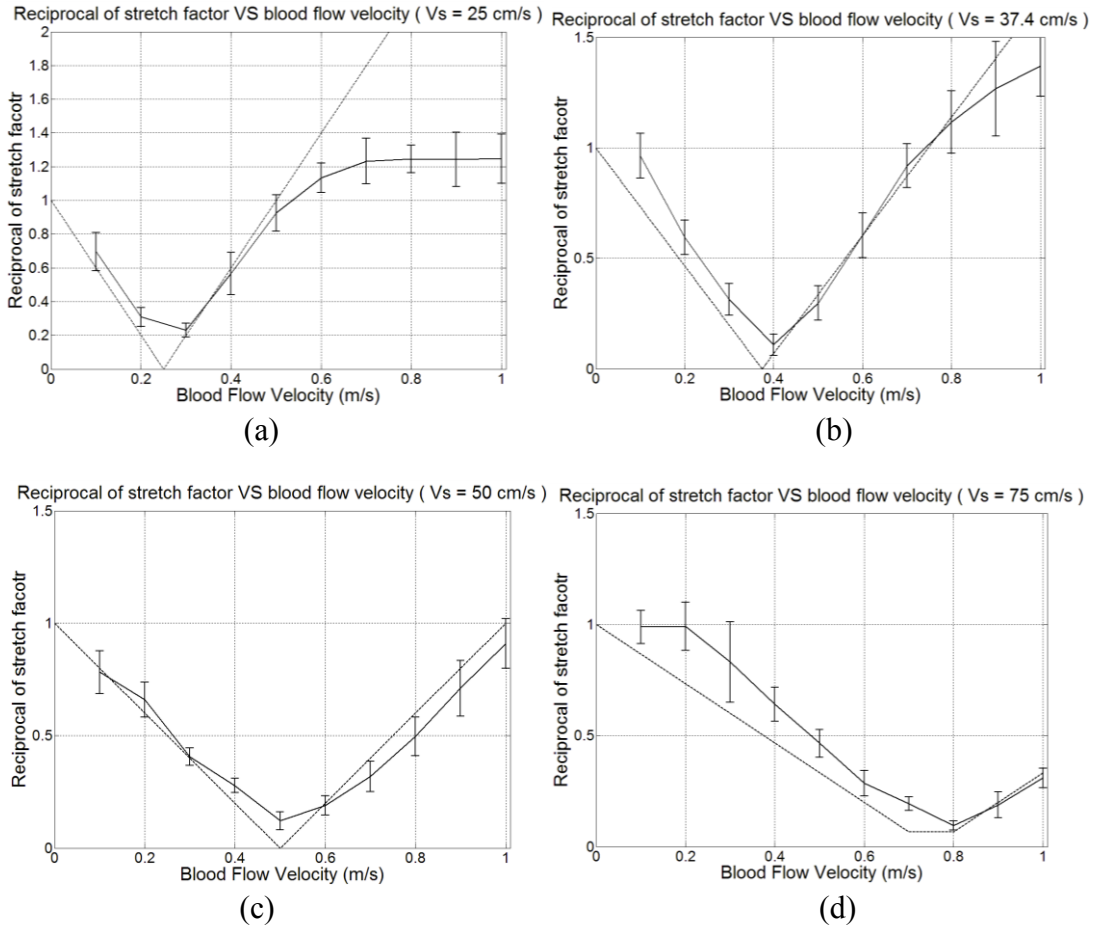

Fig. 4.6. Reciprocal of stretch factor with standard deviation (with flow gradient). Dashed lines are theoretical lines represented by (2) and (3). (a) Scan velocity is 25 cm/s, (b) Scan velocity is 37.4 cm/s, (c) Scan velocity is 50 cm/s, (d) Scan velocity is 75 cm/s.

Results of the blood flow phantom data are shown in Fig. 4.7. Compared with simulated data, the estimation errors are more significant for all four scan velocities. Specifically, the overestimation phenomenon is worse than results from Fig. 4.6. This can be seen from part (b) when the flow velocity is greater than the scan velocity and in part (c) and (d), the reciprocal of the stretch factor is always overestimated whether the flow velocity is greater or less than the scan velocity.

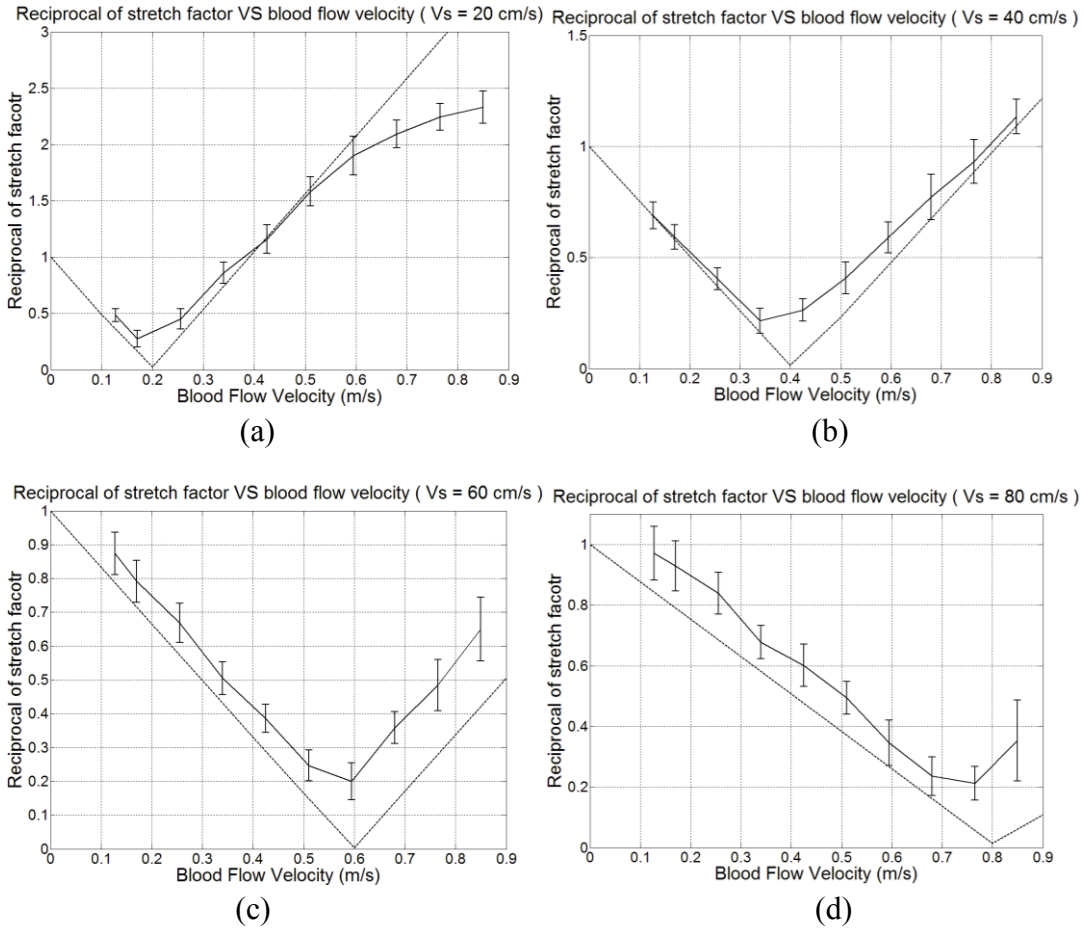

Fig. 4.7. Reciprocal of stretch factor with standard deviation (blood flow phantom). Dashed lines are theoretical lines represented by (2) and (3). (a) Scan velocity is 20 cm/s, (b) Scan velocity is 40 cm/s, (c) Scan velocity is 60 cm/s, (d) Scan velocity is 80 cm/s.

To see the performance of velocity estimation using speckle size more directly, the estimated velocities were plotted versus actual velocities in Fig. 4.8. Results in three conditions were shown here respectively. In each condition, the estimation results with standard deviation from four different scan velocities were plotted along with the reference line.

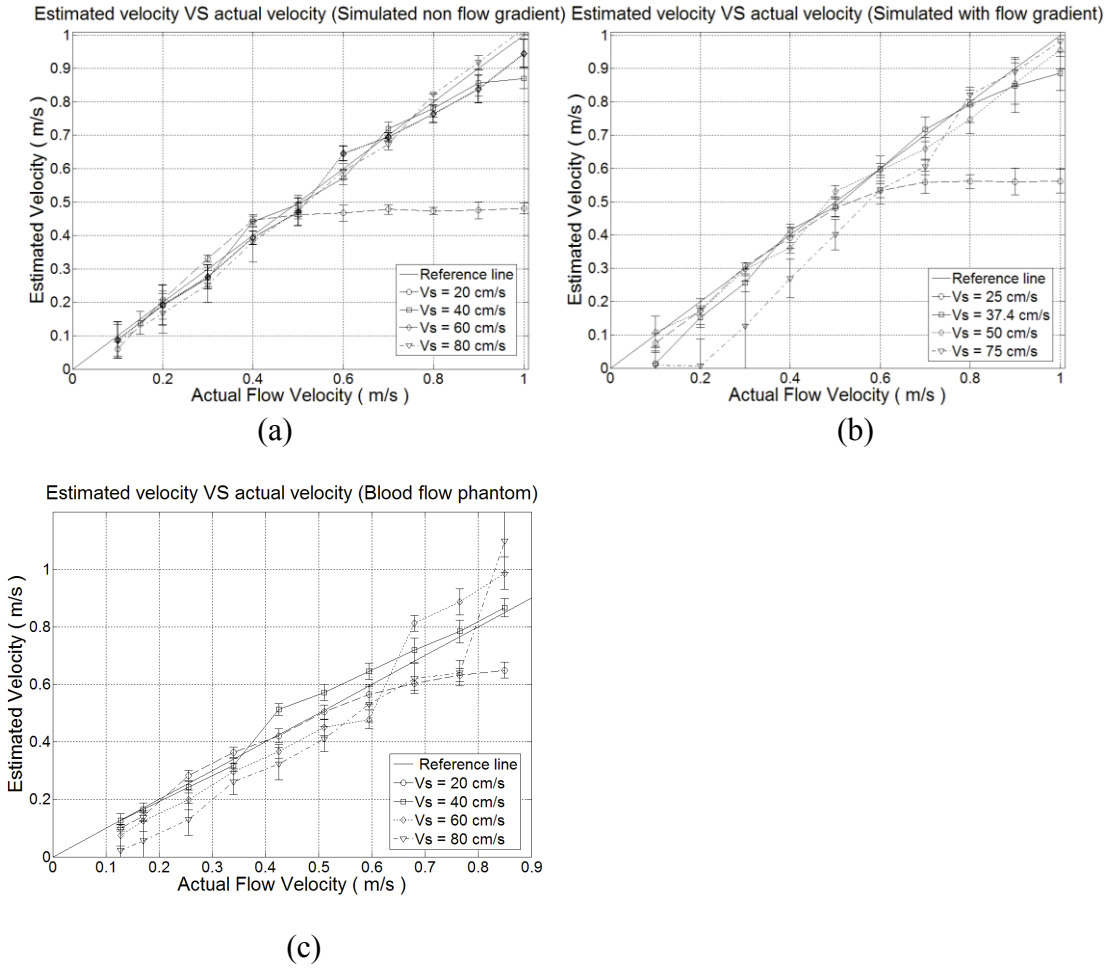

Fig. 4.8. Estimated velocities versus actual velocities. (a) Simulated data without flow gradient, (b) Simulated data with flow gradient, (c) Blood flow phantom data.

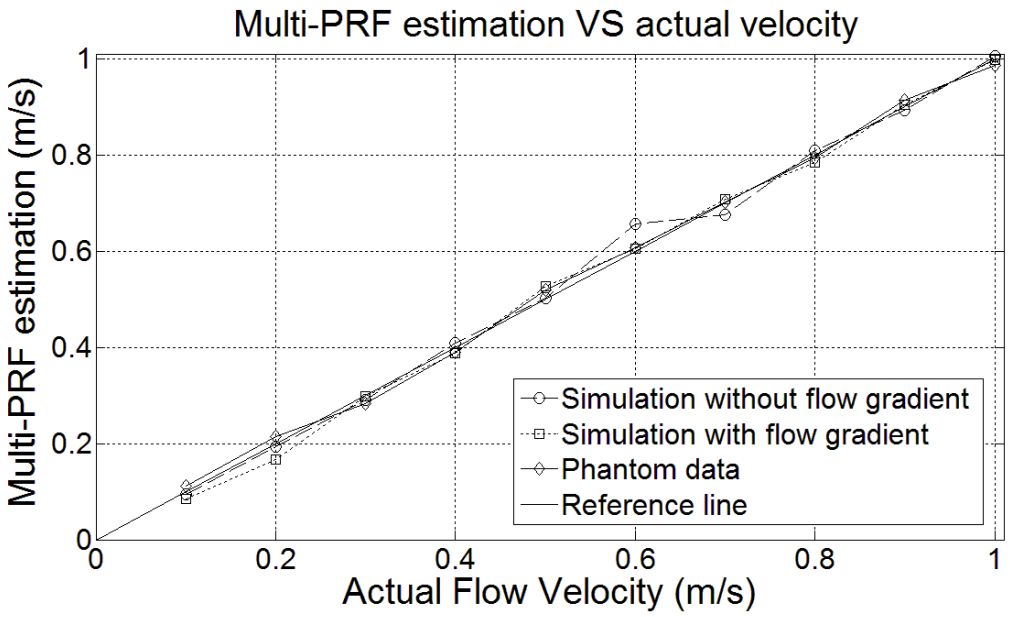

Fig. 4.9. Multi-PRF estimated velocities versus actual velocities.

Some initial results of the least-squares model are produced using the estimated results from both simulated data and phantom data. The weighting vector is $W_1 = \{0.2, -0.24, 0.2, 0.91\}$ from the simulated data without a flow gradient, and $W_2 = \{-0.36, 0.61, 0.95, -0.26\}$ from the simulated data with a flow gradient. When the phantom data were used, the weighting vector is $W_3 = \{0.52, 0.43, -0.09, 0.26\}$. Using these weighting parameters, the multi-PRF estimation results are calculated by (4.11) and plotted in Fig. 4.9.

4.5 Discussion

The results in Fig. 4.5, 4.6 and 4.7 show that there is an approximate linear relationship between the reciprocal of the stretch factor and flow velocity, as seen in (4.8) and (4.9). Generally, when there is no gradient in the flow, the experimental results fit the theoretical line well. Furthermore, experimental results from simulated data fit the theoretical line better as compared to phantom data.

From part (a) of Fig. 4.5, 4.6 and 4.7, it can be seen that the reciprocal of the stretch factors tend to remain constant around 1.3 to 1.5 in the simulated data and 2 to 2.5 in the blood flow phantom data. The reason for this phenomenon is that in simulated data, the speckle size of the non-flow condition was less than one correlation lag (about 0.7 lags by linear interpolation), which corresponds to one interval between every A-line. When the flow velocity is much faster than the scan velocity, the scatterers "leave" the interrogation beam in one frame quickly, leading to rapid decorrelation (Friemel et al. 1998). However, as the speckle pattern in one frame becomes more random, its speckle size will stop decreasing (does not become any more 'random') when it approaches a minimum value. A similar phenomenon happens when the transducer scans against the blood flow, the speckle size of blood flow and non-flow condition is within 95% of each other. In the simulated data, the minimum speckle size of blood flow is 0.5 lags, which gives a maximum reciprocal stretch factor of 1.4. In the data from the flow phantom, the speckle size of the non-flow condition was about 1.2 lags, and the minimum speckle size of flow was 0.5 lags, which gives a maximum reciprocal stretch factor of 2.4.

In Fig 4.6, when the scan velocity is 50 and 75 cm/s, compared with the results where the flow data do not have a flow gradient, the reciprocal of the stretch factor tends to be overestimated compared to the theoretical values when the flow velocity is less than the scan velocity, which means the speckle size is underestimated in this condition. This phenomenon can be explained by speckle decorrelation caused by the flow gradient. A flow gradient causes scatterers to move relative to one another, which will change their phase relationship. As a result, the speckle pattern in the reflected ultrasound signal will

decorrelate, which will produce a smaller speckle size as compared with the non-flow gradient condition.

In Fig. 4.7 where the data are from the blood flow phantom, the decorrelation effects are even more significant than the simulated data. One of the reasons should be the same as for the results from Fig. 4.6 since the flow gradient exists in the flow phantom. Another reason for the increased decorrelation phenomenon could be inherent random movement of scatterers in the flow phantom. During the simulation, the scatterers did not move in the axial or elevation dimension, while there is expected to be some random motion of the scatterers within the phantom.

The estimated velocities versus actual simulated and blood flow phantom velocities are plotted in Fig. 4.8. When the scan velocity is 20 cm/s, the estimation results follow the theoretical line well up to about 50 cm/s flow velocity, then deviate from the actual value with increasing flow velocity. The reason is the same as for the errors of the stretch factor reciprocal when the scan velocity is 20 cm/s. When the scan velocity is 40, 60 and 80 cm/s, the estimation results generally fit the reference line within the range of one standard deviation. To quantitatively evaluate the performance of estimation by different scan velocities, the mean value of estimation errors and standard deviation compared with the reference line is calculated and shown in Table 4.2.

All of the estimation error means are negative; this can be explained by speckle decorrelation which decreases the speckle size. The largest estimation error mean and standard deviation occurs when the scan velocity is the lowest in simulated data with and without a flow gradient. This is because the scatterer pattern rapidly decorrelates when

the flow velocity is much faster than the scan velocity. The overall mean value of estimation error is around 5%, where the maximum error is 7.8% and the minimum is 1.4%. Separately, when there is no flow gradient, the average estimation error is between 1.4% and 4.4%. However, when flow gradients are present, the average estimation error increased to between 4.4% and 6.8%, which means that speckle decorrelation caused by flow gradients increased the estimation error. The estimation performance was further degraded in the flow phantom data, where the average estimation error is between 6.1% and 7.8%. This phenomenon results from speckle decorrelation caused by the effects both of flow gradient and relative movement of scatterers in the blood flow phantom.

For the simulated data with a flow gradient, the weighting vector has the largest value when the scan velocity is 50 cm/s and lowest value (actually negative) when the scan velocity is 25 cm/s. This is in accordance with the estimation performance which can be seen in part (b) of Fig. 4.8. However, the initial weighting vector for the simulated data without flow gradient gives lowest weighting to the estimation when the scan velocity is 40 cm/s and highest weighting to the estimation when the scan velocity is 80 cm/s. In contrast, the weighting vector for the blood flow phantom has the largest value when the scan velocity is 20 cm/s and lowest value when the scan velocity is 60 cm/s. These results are mainly based on algorithm optimization, which are difficult to be intuitively associated with the estimation results shown in Fig. 4.8. A particularly interesting result is that some scan speeds are positively weighted while others can be negatively weighted. However, it suggests the possibility to make a more accurate estimation with multiple scan velocities. The mean value of multi-PRF estimation errors compared with the reference line is also calculated and shown in Table 4.3. It can be seen

that the estimation using multi-PRF significantly reduced the estimation error, which produced much more accurate estimations.

TABLE 4.2. THE MEAN AND STANDARD DEVIATION OF ESTIMATION ERROR. (A) SIMULATED DATA WITHOUT FLOW GRADIENT, (B) SIMULATED DATA WITH FLOW GRADIENT, (C) BLOOD FLOW PHANTOM DATA.

Scan Velocity (cm/s)	20	40	60	80
Mean Error (% of actual)	81.3%	4.4%	3.2%	1.4%
S.D. of Error (% of actual)	98.3%	12.3%	5.1%	3.0%

(a)

Scan Velocity (cm/s)	25	37.4	50	75
Mean Error (% of actual)	51.8%	6.8%	4.4%	4.9%
S.D. of Error (% of actual)	62.8%	10.4%	5.6%	8.4%

(b)

Scan Velocity (cm/s)	20	40	60	80
Mean Error (% of actual)	22.9%	6.1%	7.2%	7.8%
S.D. of Error (% of actual)	35.9%	8.9%	9.2%	8.9%

(c)

TABLE 4.3. THE MEAN OF ESTIMATION ERRORS OF MULTI-PRF ESTIMATION.

Data Source	Simulation with a flow gradient	Simulation without a flow gradient	Phantom data
Mean Error (% of actual)	2.9%	0.4%	1.5%

4.6 Conclusion

This chapter investigated the relationship between speckle size and (simulated or blood-mimicking) flow velocity during conventional B-mode acquisition. A linear relationship was developed between the reciprocal of stretch factor and flow velocities. The results quantified estimation performance degradation when speckle decorrelation occurred, whether by shear gradients or rate of scatterer movement out of the ultrasound beam. Initial attempts at a multiple-scan strategy for estimating flow by a least-squares model suggest the possibility of increased accuracy taking into account more than one frame of data.

Chapter 5

Optimization of Speckle Size Estimation

5.1 Introduction

An algorithm which measures the lateral blood flow velocity using speckle size change with scan velocity was developed in the previous chapter. In contrast to Doppler based blood flow measurement methods, which detect the phase change of successive ultrasound blood flow signals, this method can detect the lateral component of blood flow using the apparent speckle size change that occurs when scatterers are moving relative to the spatial rate of A-line acquisition. In the previous chapter, we showed that there is a linear relationship between the apparent speckle size and the spatial rate of A-line acquisition. A region of interest (ROI) was selected from the blood flow image for velocity estimation, and results showed that the estimation error of this algorithm

increases mainly with two factors. The first factor is flow gradient which simulates the axial spatial velocity variation in fully developed laminar flow in a straight vessel, and the other factor is random scatterer movement, simulating the turbulent component of flow. In this chapter, the relationship between blood velocity estimation using equation (4.8) and (4.9) for flow purely lateral to the ultrasound beam and flow gradient, random scatterer movement and ROI size is investigated and quantitatively assessed. Simulated lateral blood flow data with and without flow gradient and random scatterer movement were generated by the Field II simulation program. The flow gradient is introduced by a parabolic flow profile in the simulated vessel and the random scatterer movement is generated by adding Gaussian noise to the scatterers' position with a standard deviation as much as one-tenth of the resolution cell size in each direction (lateral, elevation, and axial). In addition, phantom lateral blood flow with inherent flow gradient and random scatterer movement was also analyzed in this chapter. In the end, blood flow velocity estimation for flow purely lateral to the ultrasound beam was compared between speckle size estimation and speckle tracking. Our results showed that: 1) in plug flow, estimation error decreases with increasing ROI size, with an average minimum bias below 5%. An optimal ROI size exists in both directions, which is 2.5 axial resolution cell lengths axially and 30 lateral resolution cell widths laterally; 2) the estimation bias increases up to 10% with flow gradient. An optimal lateral ROI size still exists given the presence of a flow gradient and the estimation error increases with increasing axial ROI size since the correlation length shortens by the introduction of a flow gradient; 3) in addition to the previous results, when random scatterer movement is introduced into the blood flow, the average estimation bias is worse by about a factor of three than data without random

scatterer movement, which can be seen both in the simulation and phantom data; and 4) speckle size estimation can measure blood flow velocity over a larger range by choosing an optimal ROI size compared with speckle tracking. These results may help researchers select optimal conditions for blood flow measurement using speckle size estimation according to specific flow conditions.

5.2 Materials and Methods

A commercial flow phantom (Optimizer RMI 1425, Gammex, Middleton, WI), was used to simulate parabolic blood flow with random scatterer movement. The blood-mimicking fluid which has acoustic properties similar to blood (speed of sound 1550 m/s, density 1.03 g/mL) was pumped through a tube (5 mm inside diameter, 1.25 mm thickness) in the phantom, and the tube was surrounded by tissue mimicking material (speed of sound 1540m/s, attenuation 0.5 dB/cm/MHz). A SONOLINE Antares ultrasound imaging system (Siemens Medical Solution, Ultrasound Division, Issaquah, WA) was used for data acquisition. The VF13-5 linear array transducer (192 elements, 6.15 MHz center frequency) was set to focus on the tube located 2 cm deep in the blood flow phantom, with a total imaging depth of 4.5 cm. The Axius Direct Ultrasound Research Interface (URI) was employed to transfer ultrasound data (post-beamformation but before any down-stream processing) to a computer for further analysis. Imaging parameters can be accessed from the header information given by the URI, including frame rate, number of A-lines and beam spacing. Thus, the scan velocity can be calculated given the values of these parameters. In our experiments, the frame rate was about 12-15 frames/sec. Each image contains 312 lines with a beam spacing of 0.1234 mm; thus, the scan velocity was 50 cm/s.

In addition, a Field II simulation (Jensen and Svendsen 1992; Jensen 1996b) was also used to generate blood flow data for the experiments. The parameters used in the simulation are similar to the SONOLINE Antares Ultrasound Imaging System and the flow phantom as mentioned above. The complete parameter list can be seen in Table 5.1.

TABLE 5.1. PARAMETERS OF TRANSDUCER AND BLOOD FLOW PHANTOM USED IN SIMULATION.

Transducer	
Center frequency	6.15 MHz
Element height	2.5 mm
Element width	0.176 mm
Kerf	25 μm
Number of elements	192
Transmit focus	20 mm
Sampling frequency	40 MHz
Blood flow phantom	
Speed of sound	1550 m/s
Depth of vessel	20 mm
Diameter of vessel	5 mm
Flow direction	Parallel to the surface of the transducer

Four flow conditions were simulated: the first flow condition had a plug flow distribution with velocities of 20, 40, 60, 80 and 100 cm/s. The second flow condition had a parabolic velocity distribution in the flow with maximum velocity at the center (80, 90 and 100 cm/s) and decreasing to zero at the boundary of the vessel. The third flow

condition had a plug flow distribution as in the first condition, but the scatterers underwent random movement in the elevation, lateral and axial directions. These random movements had zero mean, and the standard deviation was one-tenth of the resolution cell size in each direction. The fourth flow condition had the same parabolic velocity distribution as in the second condition, but the scatterers underwent random movement in the elevation, lateral and axial direction. These random movements also had zero mean, and the standard deviation was one-tenth of the resolution cell size in each direction.

Based on the imaging parameters, the lateral resolution cell length is about the same size as the distance between each A-line; thus, estimation results based on these data had a large variance since the sampling was quantized at the beam (A-line) spacing. In most commercial machines, lateral data during 1-D flow measurement can be undersampled without affecting 1-D blood flow estimation performance. To mitigate this problem during simulation, the flow data was oversampled by a factor of ten along the lateral direction (auto-covariance direction) using linear interpolation before speckle size estimation.

To investigate the relationship between performance of velocity estimation for flow purely lateral to the ultrasound beam and ROI size, different ROI sizes and positions were selected for each flow condition. For plug flow, the ROI was selected at the center of the vessel, the lateral ROI size was varied from 5 to 60 times the lateral resolution cell length and the axial ROI size was varied from 1 to 3 times the axial resolution cell width. In parabolic flow, the ROI was positioned at three different sites where the distance from the vessel longitudinal axis was 1.35, 0.7 and 0 mm. For each position, the lateral ROI size

was varied from 5 to 60 times the lateral resolution cell length and the axial ROI size was varied from 1 to 3 times the axial resolution cell width.

5.2.1 Flow gradient

To investigate the relationship between estimation performance for flow purely lateral to the ultrasound beam and flow gradient, instead of using three sites, the ROI was positioned at seven sites within the parabolic profile to maximize the axial span range in the vessel, which is shown in Fig. 5.1, where distance from the vessel longitudinal axis was ±1.8, ±1.2, ±0.6 and 0 mm. The parabolic flow has a velocity defined as,

$$V_f = V_{\max}\left(1-\left(\frac{r}{R}\right)^2\right) \tag{5.1}$$

Where V_{max} is the maximum velocity in the vessel, r represents the distance from the vessel longitudinal axis and R represents the radius of the vessel, which is 5 mm. The flow gradient is then calculated as (5.2),

$$Flow\,Gradient = \frac{\partial V_f}{\partial r} = -2V_{\max}\frac{r}{R^2} \tag{5.2}$$

The ROI size at these positions was fixed according to the information gained from the relationship between estimation performance and ROI size.

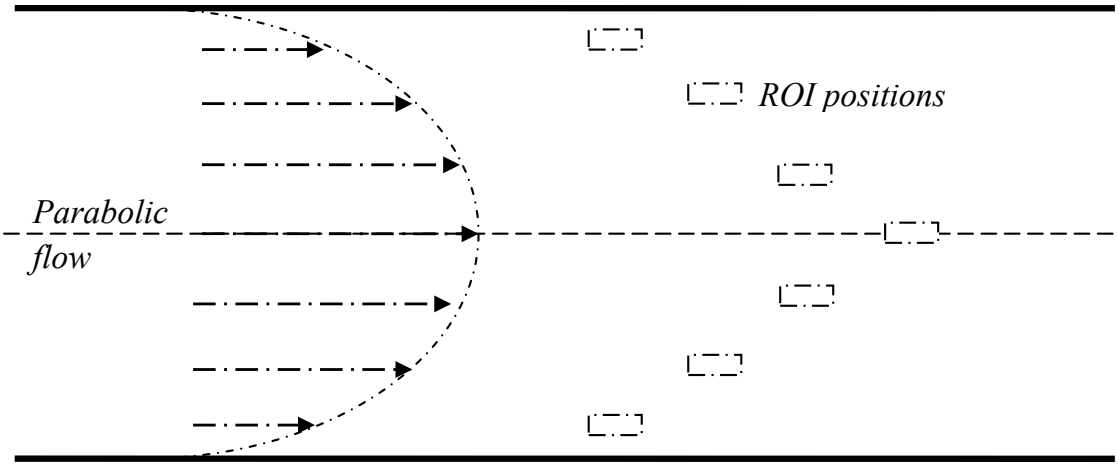

Fig. 5.1. The seven positions of ROI in parabolic flow

5.2.2 Random scatterer movement

In addition to flow gradient in actual *in vivo* blood flow, random movement of scatterers occurs occasionally, especially in vessel bifurcation areas where turbulent flow potentially develops. Thus, all the analyses above were performed both on flow data modeled with and without random scatterer movement. The effect of random scatterer movement on the velocity estimation for flow purely lateral to the ultrasound beam can be determined by comparing the estimation results of these two conditions.

Identical analyses were performed on the data collected from the blood flow phantom. The only difference is that the axial ROI size was varied from 1 to 10 times the axial resolution cell width in the phantom data, since the axial resolution cell width of the SONOLINE Antares Ultrasound Imaging System is about one fourth of the axial resolution cell width of the Field II simulation. The reason is that B-mode images were collected by the imaging system where the impulse response of the transducer is shorter to improve axial resolution

Finally, the performance of velocity estimation for flow purely lateral to the ultrasound beam using speckle size estimation was compared to speckle tracking using data from a blood flow phantom. Since speckle tracking requires two successive frames to estimate the displacement of a regional pattern within an ROI, there must be at least partial overlap of the speckle pattern within the ROI. This requirement limits the highest blood flow velocity which can be detected given a certain imaging frame rate. For the commercial scanner in our lab, based on imaging parameters set for speckle size estimation, the highest blood flow velocity that can be detected using speckle tracking is 45 cm/s. Thus, flow data with velocities of 15, 30 and 45 cm/s were collected from the blood flow phantom, and velocities were estimated by speckle size estimation and speckle tracking simultaneously to compare their performance.

5.3 Results

The relationship between estimation performance and ROI size is shown in Fig. 5.2. Part (a) shows the relationship between the estimation error and axial ROI size and part (b) shows the relationship between the estimation error and lateral ROI size. Ten data sets were used for the estimation and the error bars show ± one standard deviation of the estimation bias. Plug flow with no random scatterer movement is used for this result. With increasing axial ROI size, the maximum estimation bias decreases from 13% to 3% and the maximum standard deviation of bias decreases from 3% to 1%. With increasing lateral ROI size, the maximum estimation bias decreases from 8% to 3% and the maximum standard deviation of bias decreases from 4% to 1%.

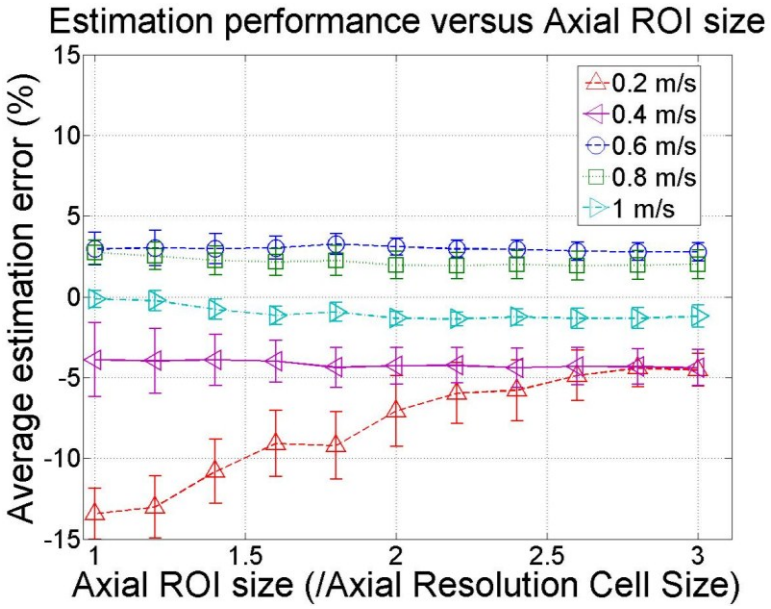

(a)

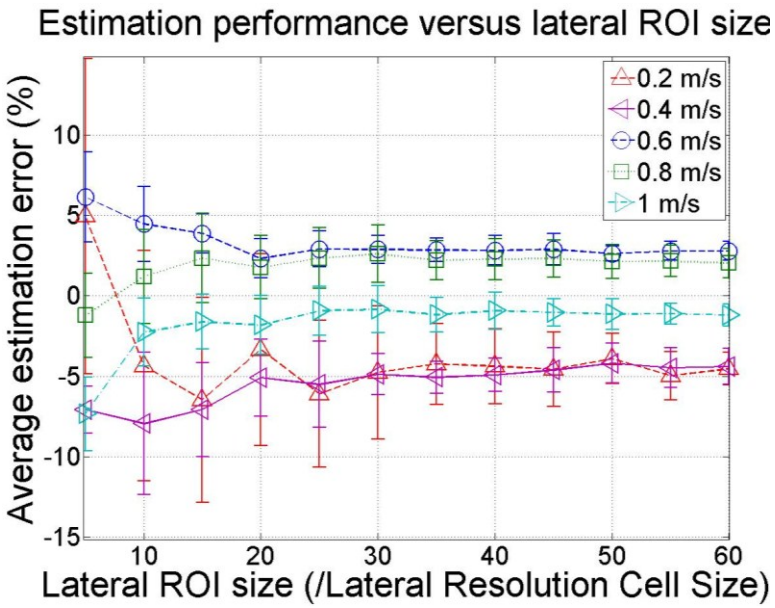

(b)

Fig. 5.2. The relationship between estimation error and (a) axial ROI size, (b) lateral ROI size. Simulated plug flow.

Fig. 5.3 shows the relationship between the estimation error and the magnitude of the flow gradient. In parabolic flow profile, the flow gradient increases from the center to the boundary of the vessel. When the maximum velocity in the parabolic flow profile is 1

m/s, the maximum estimation bias decreases from 13% to 3%, and the standard deviation of bias decreases from 3% to 1%. A similar relationship exists when the maximum velocity is 0.9 m/s and 0.8 m/s.

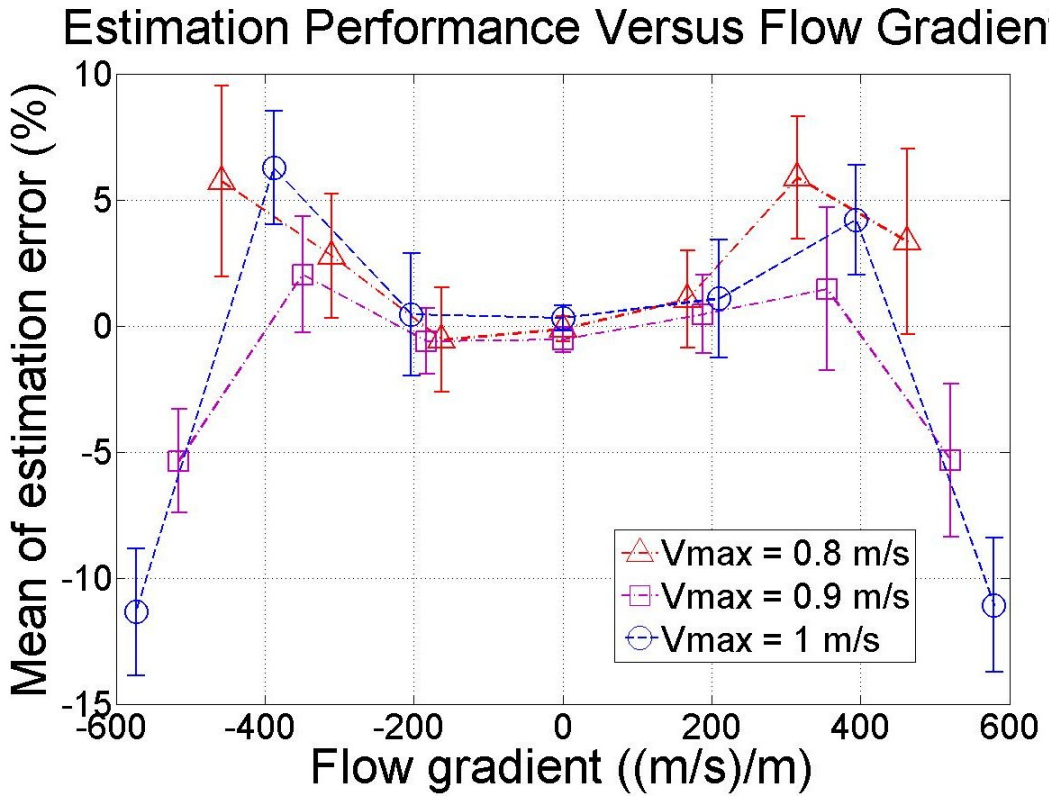

Fig. 5.3. The relationship between estimation error and flow gradient. Simulated parabolic flow.

The relationship between estimation error and ROI size was also investigated given the presence of a flow gradient, which can be seen in Fig. 5.4. Part (a) and (d) show the relationship between estimation error and lateral/axial ROI size at the position where distance from the vessel longitudinal axis was 1.35 mm (the magnitude of flow gradient is 345, 388 and 432 (m/s)/m when the velocity is 0.8, 0.9 and 1 m/s). Part (b) and (e) shows the relationship between estimation error and lateral/axial ROI size at the position where distance from the vessel longitudinal axis was 0.7 mm (the magnitude of flow

gradient is 179, 201 and 224 (m/s)/m when the velocity is 0.8, 0.9 and 1 m/s). Part (c) and (f) shows the relationship between estimation error and lateral/axial ROI size at the center of the vessel.

A similar analysis was done on the simulated flow data which included random scatterer movement and blood flow phantom data. These results can be seen in Figs. 5.5 to Fig. 5.9. Fig. 5.5 shows the relationship between estimation error and ROI size in plug flow with random scatterer movement. Fig. 5.6 shows the relationship between estimation error and flow gradient in parabolic flow with random scatterer movement and Fig. 5.7 shows the relationship between estimation error and ROI size in parabolic flow with random scatterer movement. Fig. 5.8 shows the relationship between estimation error and flow gradient in the blood flow phantom and Fig. 5.9 shows the relationship between estimation error and ROI size in the blood flow phantom.

Fig. 5.10 shows a comparison of the estimation performance between speckle size estimation and speckle tracking. The same ROI was used for both methods. Parts (a) and (b) show the relationship between estimation performance and ROI size for blood flow velocity estimation using speckle size estimation. Comparison of estimation performance can be seen in parts (c) and (d), showing the relationship between estimation performance and ROI size using the speckle tracking method.

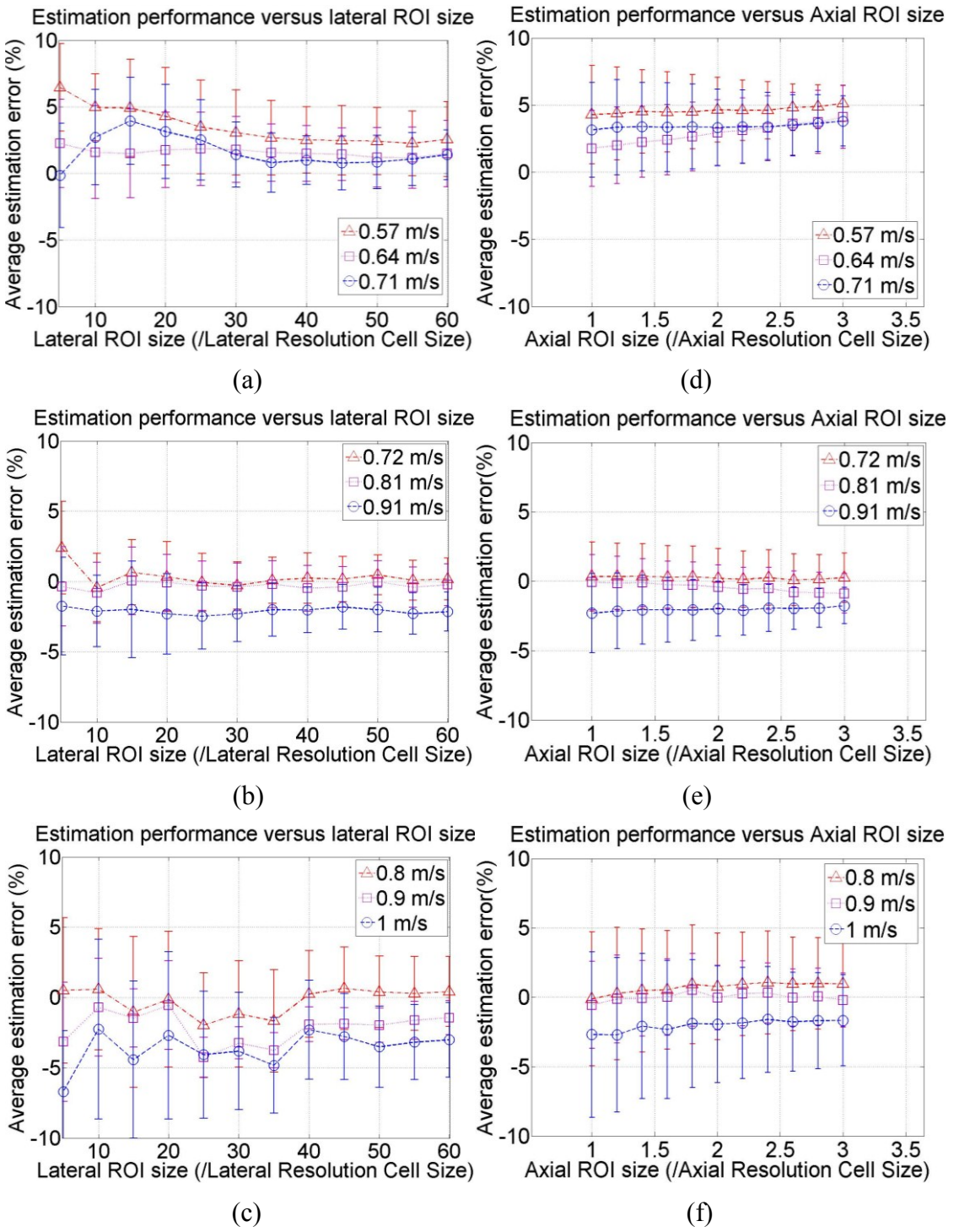

Fig. 5.4. The relationship between estimation error and (a) lateral ROI size at *r = 1.35 mm*, (b) lateral ROI size at *r = 0.7 mm*, (c) lateral ROI size at *r = 0 mm*, (d) axial ROI size at *r = 1.35 mm*, (e) axial ROI size at r = *0.7 mm*, (f) axial ROI size at *r = 0 mm*. Simulated parabolic flow.

5.4 Discussion

The results in Fig. 5.2 show that the estimation bias and its standard deviation decrease with increasing ROI size. It can be seen that the average estimation error is significant when the ROI size is small, either in the lateral direction or the axial direction. Then the estimation error decreases when the ROI size increases. The reason for this is that a larger ROI includes more speckle pattern information, in which correlation properties can be better preserved for speckle size estimation. On the contrary, a small ROI is less capable of providing sufficient correlation information for speckle size estimation; a higher estimation error will occur in this case. Furthermore, there is a value for the ROI size which minimizes the estimation bias (within the parameters explored) both axially and laterally. In the axial direction, the estimation performance approaches an asymptote when the axial ROI size is about 2.5 axial resolution cell widths. In the lateral direction, the estimation performance approaches an asymptote when the lateral ROI size is about 30 lateral resolution cell lengths. The reason for this is that sufficient correlation information has been included in the ROI when the ROI size reaches these optimal values, thus, little improvement of the estimation performance can be attained afterwards.

Fig. 5.3 shows the relationship between estimation error and flow gradient. It can be seen that for three different parabolic flow profiles, the average estimation error increases with increasing flow gradient, the minimum error occurs at the center of the vessel where less flow gradient is present and the estimation error increases towards the boundary of the vessel. One reason for this is that the flow gradient deceases from the

boundary to the center of the vessel. Another reason is that the blood flow velocity in the area where the distance from the vessel longitudinal axis equals 1.8 mm is close to the scanning velocity, on which condition the estimation is prone to have increased error as discussed in our previous studies (Xu and Bashford 2010).

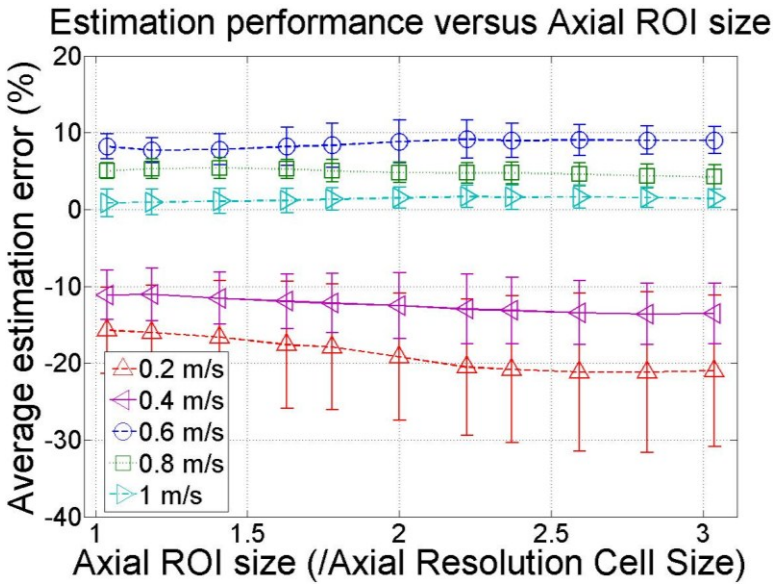

(a)

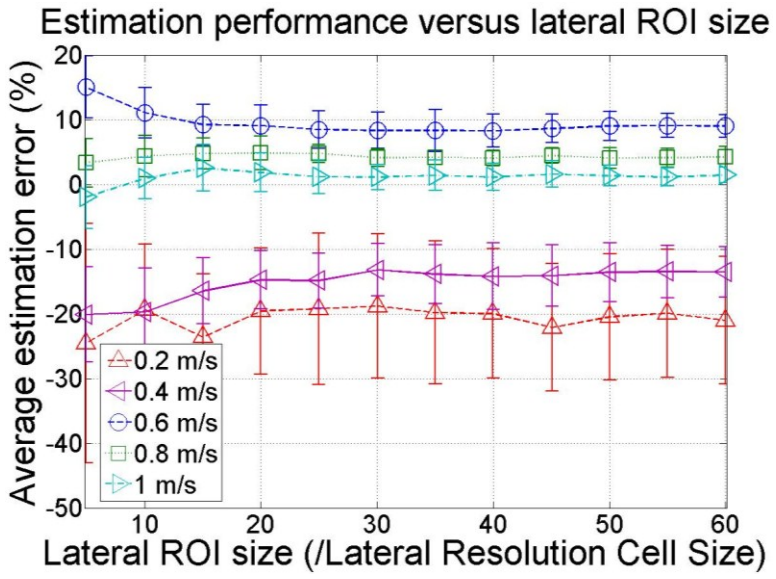

(b)

Fig. 5.5. The relationship between estimation error and (a) axial ROI size, (b) lateral ROI size. Simulated plug flow with random scatterer movement.

Fig. 5.4 shows the relationship between estimation error and ROI size with flow gradient. In parts (a), (b) and (c), it can be seen that the estimation error decreases with increasing lateral ROI size, which is similar to the results in Fig. 5.2(b), since more information is included in a larger ROI. Also, an optimal threshold value exists for the lateral ROI size, which is around 35 lateral resolution cell lengths.

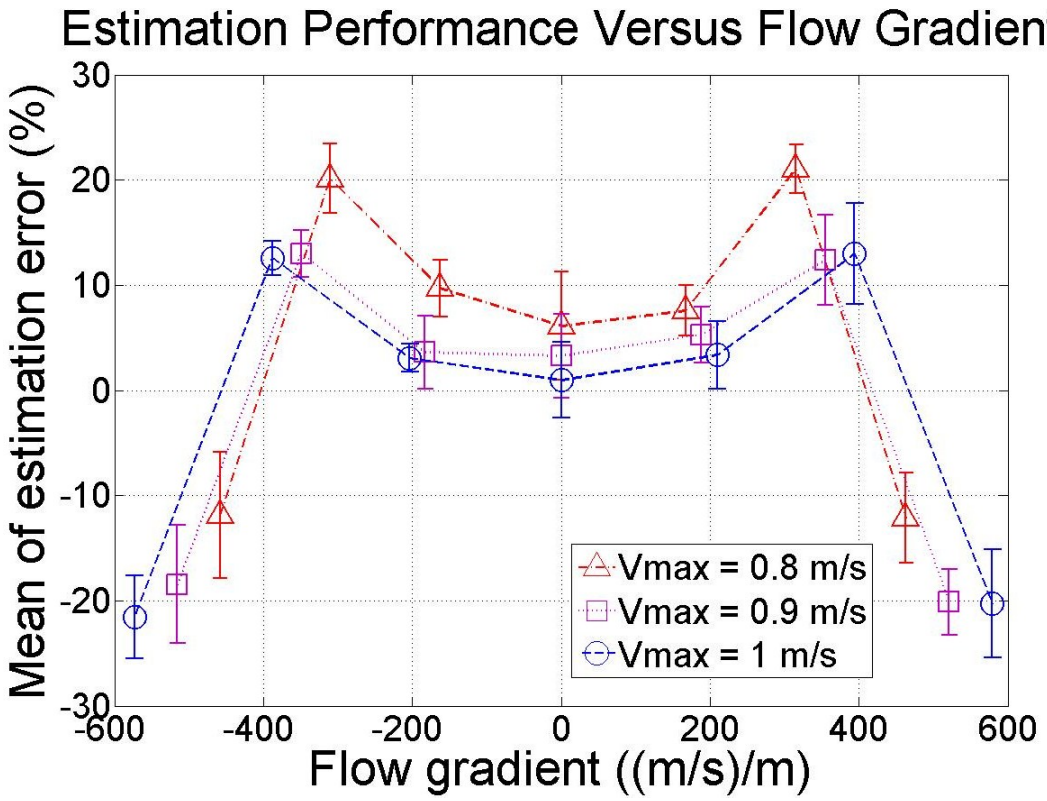

Fig. 5.6. The relationship between estimation error and flow gradient. Parabolic flow with random scatterer movement.

However, in parts (d), (e) and (f), which represent the relationship between estimation error and axial ROI size, the estimation error increases with the axial ROI size, instead of approaching an asymptote after an optimal value. We reason that increasing axial ROI size will introduce more flow gradient into the ROI and degrade the correlation information for speckle size estimation. This can be clearly seen in part (d), where the

estimation bias increases by 2% with the increase of axial ROI size. In parts (e) and (f), a slight decrease of estimation bias with axial ROI size occurs when the peak velocity is 0.91 and 1 m/s. The reason is that the flow gradient decreases in the ROI at these positions, and the estimation bias becomes nearly constant for different axial ROI size.

Fig. 5.5 shows the relationship between estimation error and ROI size when random scatterer movement is included in the plug flow. It can be seen that the average estimation error is higher than the results shown in Fig. 5.2 where no random scatterer movement exists in the plug flow. The reason for this is that the random scatterer movement shortens the speckle size, thus introducing error into speckle size estimation. In the axial direction, estimation performance cannot be further improved with the increase of axial ROI size. In the lateral direction, estimation error decreases with increasing lateral ROI size and an optimal lateral ROI size, which is about 30 lateral resolution cell lengths, exists similar to in the results in Fig. 5.2. We reason that since the speckle size estimation is calculated from the auto-covariance function of the ROI laterally, the correlation property in the lateral direction has stronger effect speckle size estimation. Thus, increasing the lateral ROI size can still increase estimation performance, given the presence of random scatterer movement.

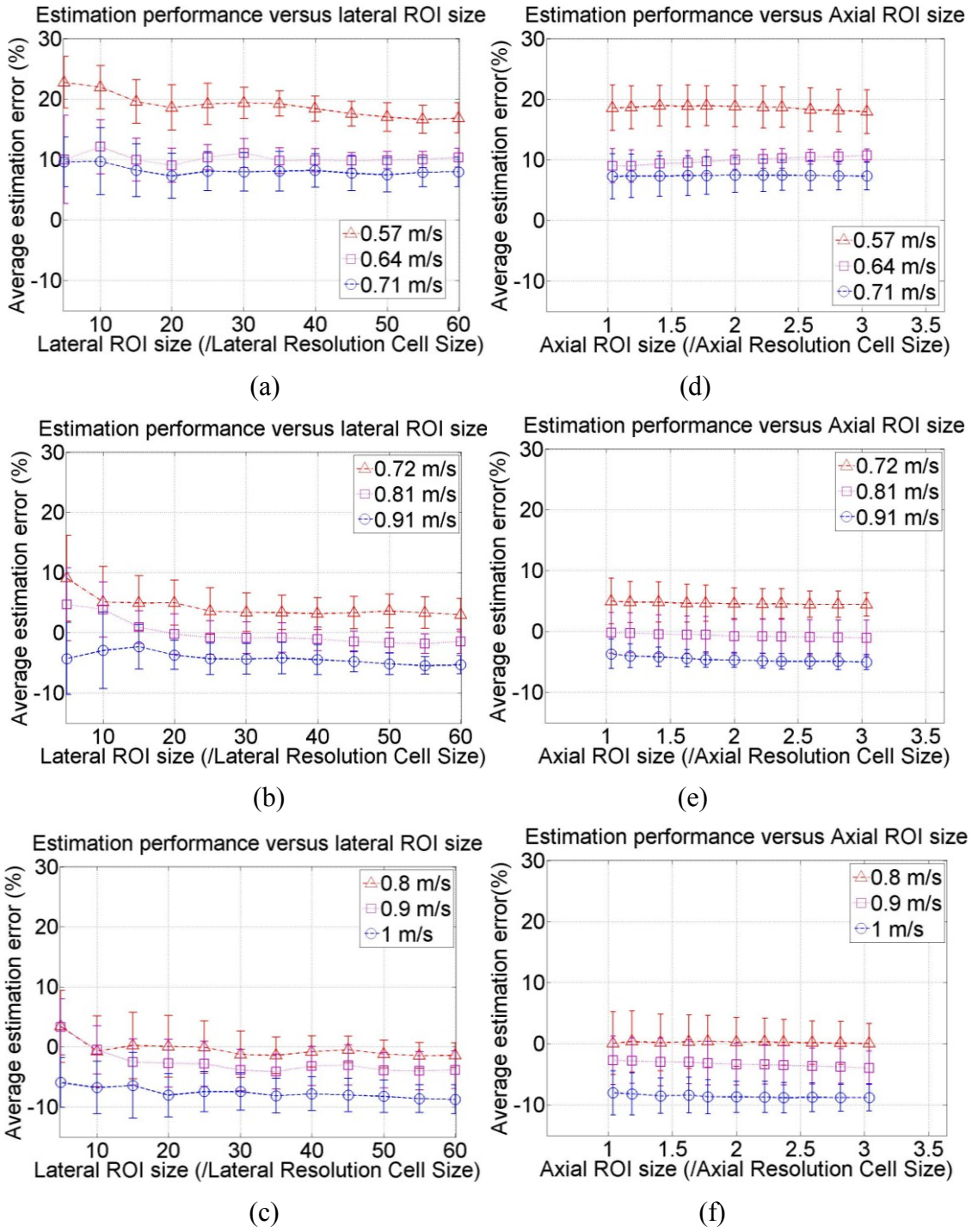

Fig. 5.7. The relationship between estimation error and (a) lateral ROI size at r = 1.35 mm, (b) lateral ROI size at r = 0.7 mm, (c) lateral ROI size at r = 0 mm, (d) axial ROI size at r = 1.35 mm, (e) axial ROI size at r = 0.7 mm, (f) axial ROI size at r = 0 mm. Simulated parabolic flow with random scatterer movement.

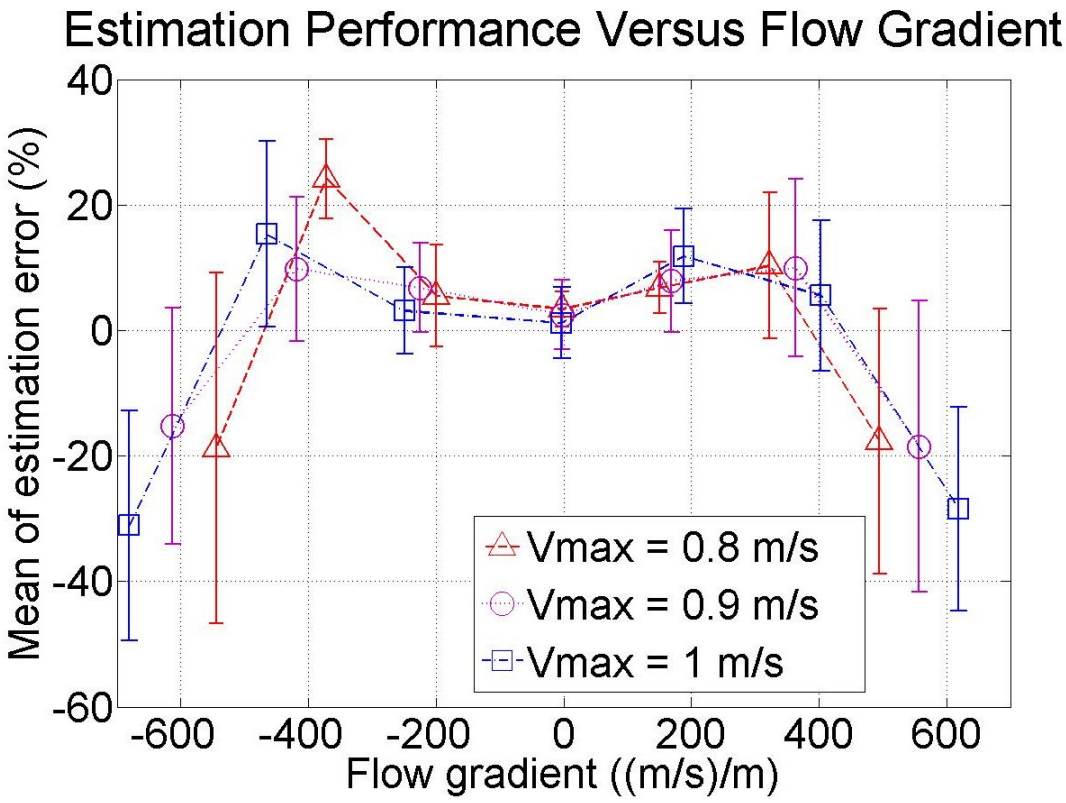

Fig. 5.8. The relationship between estimation error and flow gradient in blood flow phantom.

Fig. 5.6 shows the relationship between estimation performance and flow gradient in the parabolic flow with random scatterer movement. It can be seen that the estimation error increases with the flow gradient, which is similar to the results shown in Fig. 5.3. However, the average estimation error for each blood flow profile is around three times that of the results shown in Fig. 5.3 due to random scatterer movement. Fig. 5.7 shows the relationship between estimation performance and ROI size in parabolic flow with random scatterer movement. Generally, the relationships are similar to the results shown in Fig. 5.4. However, since random scatterer movement has been introduced into the blood flow, it can be seen that the average estimation error is around three times that of the results shown in Fig. 5.4.

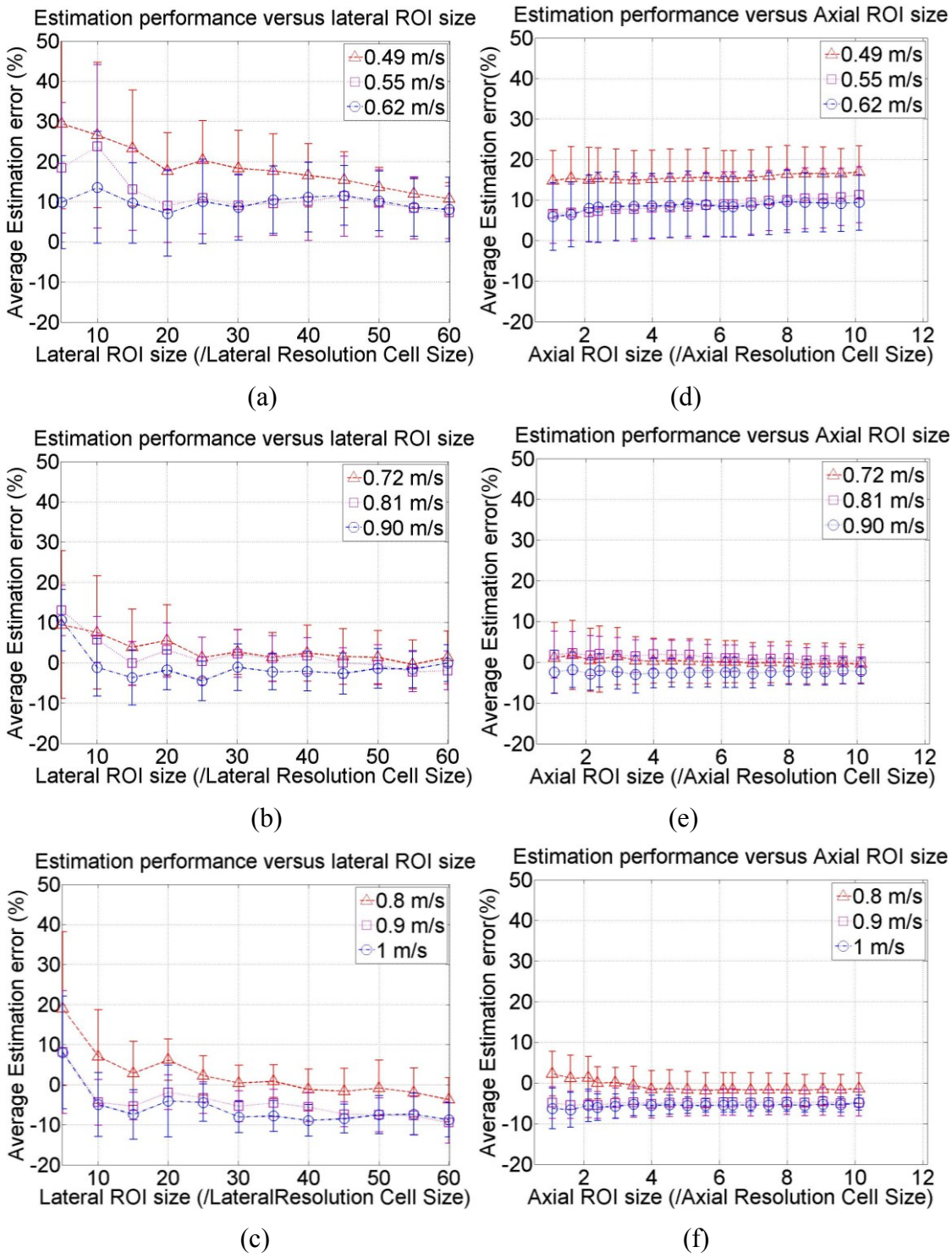

Fig. 5.9. The relationship between estimation error and (a) lateral ROI size at r = 1.35 mm, (b) lateral ROI size at r = 0.7 mm, (c) lateral ROI size at r = 0 mm, (d) axial ROI size at r = 1.35 mm, (e) axial ROI size at r = 0.7 mm, (f) axial ROI size at r = 0 mm. Blood flow phantom.

Fig. 5.8 shows the relationship between estimation performance and flow gradient in the blood flow phantom. The estimation error range is similar to that in Fig. 5.6; however, the estimation error is greater than the simulated flow when the flow gradient is high. We reason that the increase of estimation error is due to less-than-ideal parabolic flow, which will decrease the accuracy of speckle size estimation. Fig. 5.9 shows the relationship between estimation performance and ROI size in the blood flow phantom. The estimation range is similar to the results in Fig. 5.7. When the flow gradient is high, the estimation error increases with axial ROI size, which can be seen in Fig. 5.9 part (d). The optimal axial ROI size is greater than the value in the simulation, which is around six axial resolution cell widths since the axial resolution cell width of the ultrasound imaging system is much smaller than the simulation.

These results may help interested users select optimum conditions for blood flow measurement using speckle size estimation. For example, when the blood flow is close to plug flow (almost no flow gradient), Fig. 5.2 suggests that by choosing an optimal ROI size, the estimation bias can be limited below 5%. Choosing larger ROI sizes will result in increased computation time and expense without improving the estimation accuracy. In flow including a flow gradient, one can increase the lateral ROI size to an optimal value; however, the axial ROI size does not need to exceed one axial resolution cell width since the estimation error increases with axial ROI size. When random scatterer movement exists in the blood flow, the estimation error is greater than the results from blood flow without random scatterer movement, even with optimization of ROI size. The effect of random scatterer movement is difficult to minimize by only adjusting ROI size. Furthermore, the results showed that the asymptotic bias varies for different peak

velocities. The reason is that different peak velocities will result in different flow gradients and introduce different magnitudes of decorrelation. With one scan velocity, the apparent speckle size will be different for different peak velocities. Different magnitudes of decorrelation result in variation of estimation bias. In future work, we plan to investigate other ways to solve these problems, including keeping estimation accuracy in low signal-to-noise-ratio (SNR) environments and implementing this algorithm on phased or curved arrays. One potential method is multi-PRF scanning described in our previous studies (Xu and Bashford 2010).

Comparison of estimation performance between speckle size estimation and speckle tracking can be seen in Fig. 5.10. Similar to results shown above, estimation error decreases with increasing lateral ROI size for speckle size estimation with an optimal value around 45 lateral resolution cell widths, which can be seen in part (a), and the estimation error increases with increasing axial ROI size for speckle size estimation, which can be seen in part (b). The optimal ROI sizes also exist in speckle tracking both laterally and axially, since speckle tracking is done by cross-correlation of the same region from two successive frames, which relies on the correct correspondence of the same region in two images. An appropriate ROI size is necessary for tracking between fames, and more decorrelation will be included in the larger ROI, which will decrease the accuracy of cross-correlation between two images. This can be seen in part (c), where the minimum estimation error occurs when the lateral ROI size is about 20 lateral resolution cell lengths and the optimal axial ROI size is about eight axial resolution cell widths in part (d). It can also be seen in parts (c) and (d) that speckle tracking has better performance for slower blood flow. The estimation performance decreases with the

increasing of flow velocity, and this cannot be corrected by changing the ROI size. The reason for this is that the movement of scatterers in the blood will be increased with higher blood flow velocity, which will introduce more decorrelation over time and space. However, by choosing a proper ROI size, speckle size estimation can optimize blood flow velocity estimation over a larger spatial area.

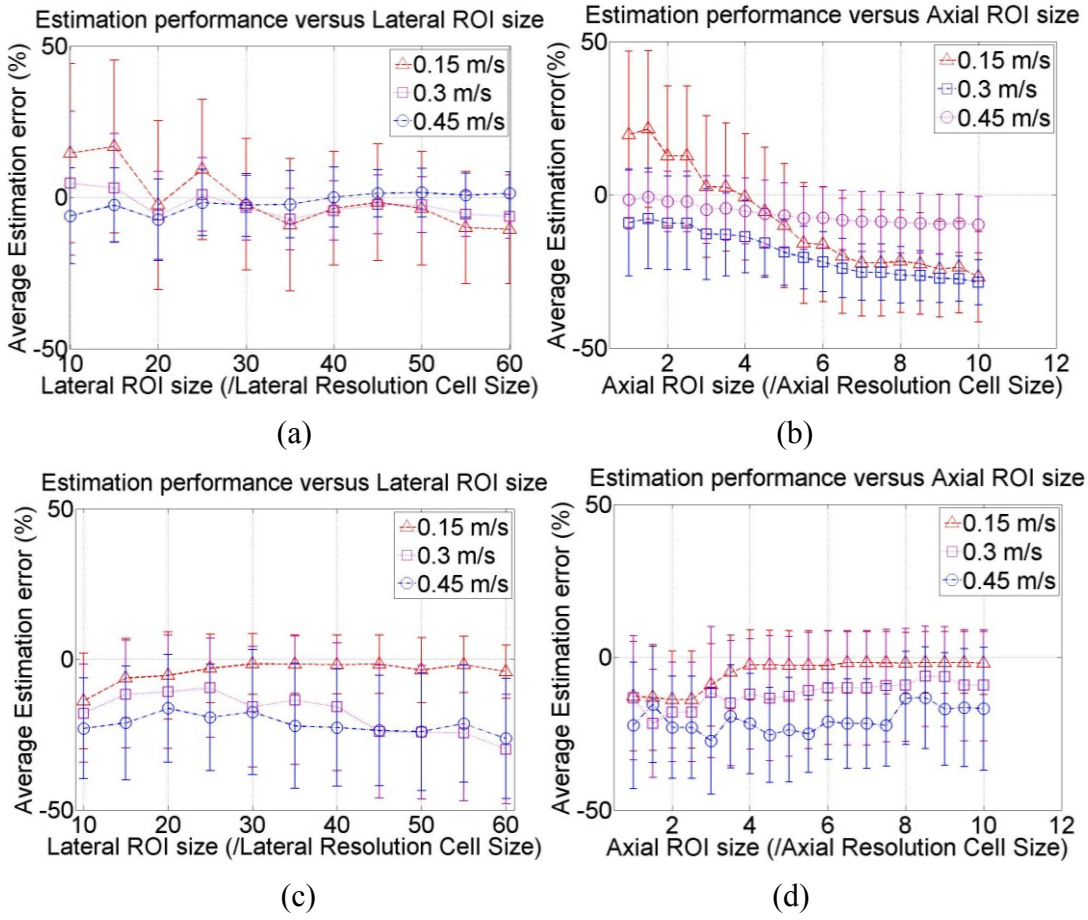

Fig. 5.10. The relationship between estimation error and (a) lateral ROI size using speckle size estimation, (b) axial ROI size using speckle size estimation, (c) lateral ROI size using speckle tracking, (d) axial ROI size using speckle tracking. Blood flow phantom.

5.5 Conclusion

This chapter investigated the relationship between blood flow velocity estimation for flow purely lateral to the ultrasound beam based on speckle size estimation and flow gradient, ROI size and random scatterer movement. Our results showed that an optimal ROI size exists both in the lateral and axial directions in plug flow, which is about 2.5 axial resolution cell widths axially and 30 lateral resolution cell lengths laterally. The estimation error increases with increasing flow gradient in parabolic flow. An optimal lateral ROI size still exists given the presence of a flow gradient; however, in the axial direction, the estimation error increases with axial ROI size because of introduced decorrelation. Similar results are shown in the simulation when random scatterer movement is introduced into the blood flow and blood flow phantom; however, the average estimation error is about 3 times that from blood flow without random scatterer movement. The comparison of blood velocity estimation for flow purely lateral to the ultrasound beam between speckle size estimation and speckle tracking shows that the accuracy of speckle tracking decreases with increasing blood flow velocity with optimal ROI size while speckle size estimation can measure blood flow velocity over a larger range. One may use these results to select an optimal ROI size for blood flow measurement using speckle size estimation.

Chapter 6

Blood Flow Measurement of the Human Jugular Vein *in vivo*

6.1 Introduction

In the previous chapters, an algorithm for resolving the lateral component of blood flow has been investigated and tested by simulation and a commercial blood flow phantom. In this chapter, this algorithm is tested with jugular vein blood flow data collected from human subjects *in vivo*. Ten subjects (5 male, 5 female) were recruited with a University of Nebraska at Lincoln (UNL) Institutional Review Board (IRB)

approval. Right jugular vein blood flow data were collected by an Antares Ultrasound Imaging System (Siemens Medical Solutions, Ultrasound Division, Issaquah, WA) and transferred to PC via the Axius Ultrasound Research Interface (URI), which enables collection of post-beamformed RF data before any further processing (e. g., demodulation, envelope detection). The scanning velocity was 90 cm/s, which is above the jugular vein blood flow velocity amplitude (Veyseller et al. 2010). Due to the pulsatility of jugular vein blood flow, about four seconds of jugular vein blood flow data were collected from each subject to cover several complete cardiac cycles. To evaluate the estimation performance of speckle size estimation, the conventional spectral Doppler data were also collected from each subject. The results showed that the estimated blood flow velocity ranges from 5 to 35 cm/s for both methods due to the pulsatility of the jugular vein blood flow. A Wilcoxon signed-rank test was used to compare the estimation results of speckle size estimation and spectral Doppler. The results showed that there is no evidence of a difference between the mean estimated velocities of speckle size estimation and spectral Doppler, which means the estimation results of speckle size estimation and spectral Doppler are comparable to each other. An initial comparison was performed on computational complexity and data acquisition time between speckle size estimation and Doppler based methods, which showed the potential time savings of blood flow velocity estimation using speckle size estimation.

During previous studies based on computer simulation and a blood flow phantom, the lateral component of blood flow was shown to be accurately resolved using the change of apparent speckle size due to the direction and spatial rate of scanner A-line acquisition (Chapter 4 and (Xu and Bashford 2009a; Xu and Bashford 2009b; Xu and

Bashford 2010)). It has been shown that the speckle size estimation method permits accurate blood flow estimation based on traditional B-mode images, which suggests that it has potential to provide a fast way of blood flow detection in real time.

To measure blood flow purely lateral to the ultrasound beam axis *in vivo* using speckle size estimation, it is appropriate to collect blood flow from a vessel close to the skin and purely lateral to the ultrasound beam axis. The carotid artery is also a potential place for data collection; however, the blood flow velocity profile in the carotid artery is complex and quickly changes with respect to time during cardiac cycles, which makes it difficult to compare its estimation results with spectral Doppler measurement. Therefore, the jugular vein blood flow data were used in this experiment since the blood flow profile shape in the jugular vein is relatively steady with respect to time.

In this chapter, data are presented from ten subjects, who were recruited and imaged by the Antares Ultrasound Imaging System in our lab. The blood flow data in the right jugular vein were acquired by a linear array for velocity estimation using speckle size estimation. Additionally, spectral Doppler data of the jugular vein were also collected for comparison. The purpose of this chapter is to show the performance of *in vivo* blood flow velocity measurement using speckle size estimation, and demonstrate it to be comparable to spectral Doppler.

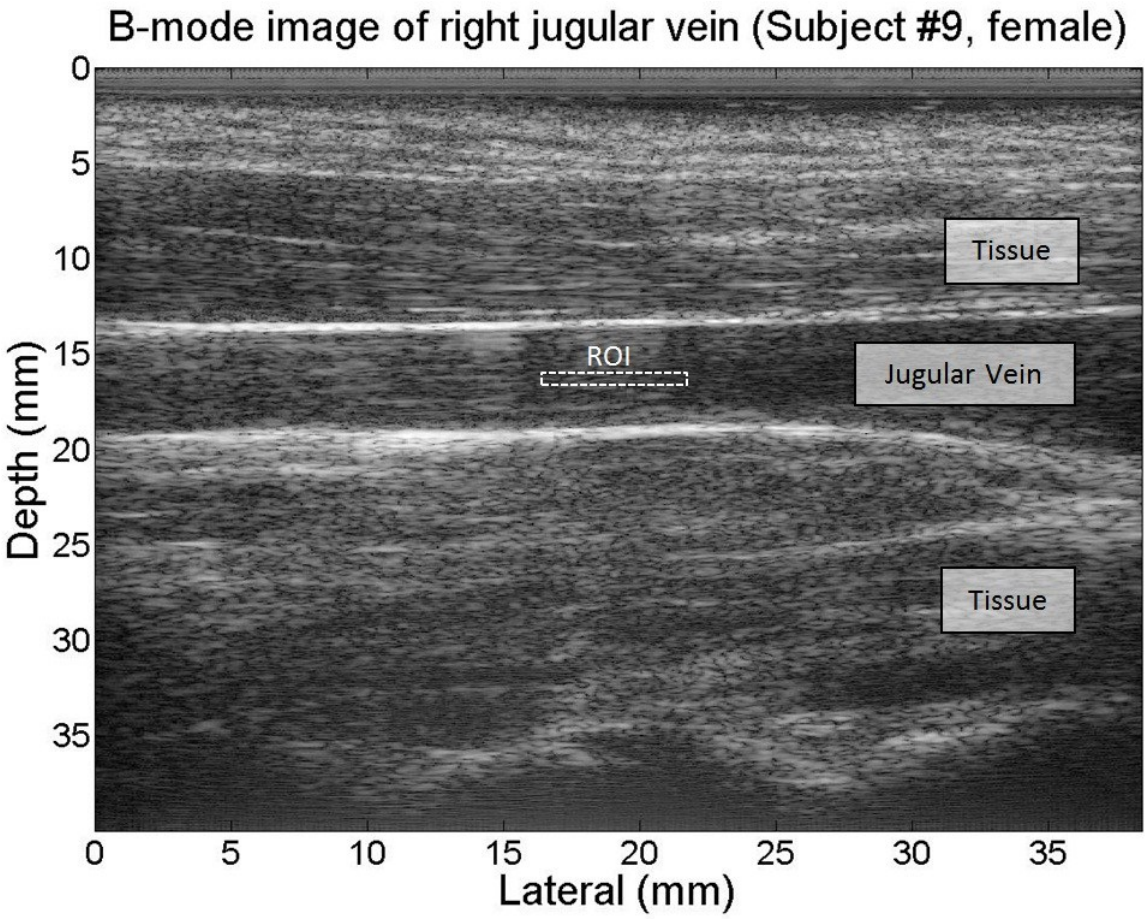

Fig. 6.1. Sample image of the right jugular vein of a female human subject collected by Siemens Antares Ultrasound Imaging System, the scan velocity is 90 cm/s. The jugular vein is corresponding to the dark area at the depth from 13 to 20 mm.

6.2 Materials and Methods

6.2.1 Subjects recruitment

Ten subjects (5 male, 5 female) were recruited from the Department of Biological Systems Engineering, University of Nebraska-Lincoln and imaged in the Biomedical Imaging and Biosignal Analysis Lab (BIBA) under an UNL IRB approval. A Siemens SONOLINE Antares Ultrasound Imaging System was used to acquire jugular vein blood flow data *in vivo*. A linear transducer (Siemens VF 13-5 transducer, center frequency

8.89 MHz, fractional bandwidth 90%) was used for data acquisition. To collect blood flow purely lateral to the ultrasound beam, the position and angle of the transducer was carefully adjusted to scan the jugular vein laterally with the scanning geometry shown in Fig. 4.2 from Chapter 4. An example of a B-mode jugular vein image can be seen in Fig. 6.1.

In chapter 4, it can be seen that when the scan velocity is greater than the lateral blood flow velocity, the relationship between the speckle size and blood flow velocity is represented by equation (4.8) and when the scan velocity is less than the lateral blood flow velocity, the relationship between the speckle size and blood flow velocity is represented by equation (4.9). For *in vivo* experiments in this chapter, since there is not *a priori* knowledge about the amplitude of blood flow velocity in the human subjects' jugular vein, it is difficult to switch between these two equations during the experiment. Thus, the scan velocity was set as 90 cm/s throughout the data acquisition, which is above the normal range of the amplitude of jugular vein blood flow velocity. As a result, equation (4.8) was used in this experiment for blood flow velocity estimation. In computer simulation and blood flow phantom experiments in Chapter 4, it is easy to calculate the speckle size of non-flow condition ($FWHM\text{-}ACVF_o$) if we set the blood flow velocity as 0 cm/s. However, it is impossible to collect blood flow data in non-flow condition *in vivo.* To solve this problem, the speckle size of non-flow condition ($FWHM\text{-}ACVF_o$) was replaced by the speckle size of blood flow collected by scanning against it ($FWHM\text{-}ACVF_a$) in equation (4.8) since $FWHM\text{-}ACVF_o$ and $FWHM\text{-}ACVF_a$ are within 95% each other as discussed in Chapter 4. As a result, the equation used for blood flow velocity estimation is shown as follows:

$$\frac{FWHM-ACVF_a}{FWHM-ACVF_s} = 1 - \frac{V_f}{V_s} \tag{6.1}$$

The complete details of the scanning parameters can be seen in Table 6.1. The "Gain" refers to the relative amplification and brightness of a B-mode image and "R/S" refers to the line density of a B-mode image, which is about 132 lines/cm when "R/S" equals five.

TABLE 6.1. PARAMETERS OF SCANNING CONFIGURATON

Transducer	
Element height	2.5 mm
Element width	0.176 mm
Kerf	25 μm
Number of elements	192
Sampling frequency	40 MHz
B-mode	
Center frequency	8.89 MHz
Exam mode	"Carotid"
Gain	9 dB
Depth of image	4 cm
R/S	5
Focal Position	2 cm
Spectral Doppler	
Gate size	1 mm
Center frequency	6.2 MHz
PRF	3720 Hz

6.2.2 Scanning protocol and data acquisition

The blood flow images of the right jugular vein were collected from ten participants after they signed an informed consent form. Ten blood flow images of the jugular vein were collected scanning both with and against the blood flow. Furthermore, spectral Doppler data of the jugular vein were also collected to compare with the blood flow velocity measurement results by speckle size estimation. The procedures of the data acquisition can be described as follows:

1) Ask the subjects to lie on an examination bed and turn their heads to their left side at an angle of 45^{o}.

2) Position the VF 15-3 transducer on the neck.

3) Carefully adjust the angle of the transducer to locate the right internal jugular vein.

4) Adjust the transducer position to make the jugular vein appear horizontal in the image.

5) Scan the jugular vein with the blood flow (from head to neck) and save the data.

6) Repeat procedures 1 and 4, change the direction of scanning (from neck to head) and save the data.

7) Repeat procedures 1 and 2, activate spectral Doppler and collect the spectral Doppler data from the same position of the jugular vein.

Since the speckle-stretch data and the spectral Doppler data were taken within 20-30 minutes of each other, with the subjects always at rest position on the examination bed, it is not expected that the mean and standard deviation of the flow pulsatility would change significantly. All the data (coded by subject) were transferred to a PC via the Axius Research Ultrasound Interface for further analysis.

As described in Chapter 4, for blood flow velocity estimation using speckle size estimation, a region of interest (ROI) corresponding to the center of the jugular vein was selected from each B-mode image, with an axial length of 0.4 mm (20 pixels) and a lateral length of 5.2 mm (60 pixels). This ROI, which is represented as *X* in the equation (4.3), was then used to calculate the mean and standard deviation of speckle size. The measured speckle size was used to estimate the flow velocity using equation (6.1).

The spectral Doppler data were used to compare with the blood flow velocity estimated by speckle size estimation. To simplify the comparison between the estimation results by spectral Doppler and speckle size estimation, the first moment of the spectral Doppler estimation was calculated as follows:

$$\bar{v} = \frac{\sum_{v_{min}}^{v_{max}} v \cdot S(v)}{\sum_{v_{min}}^{v_{max}} S(v)} \tag{6.2}$$

where $\bar{v}$ is the first moment of the spectral Doppler estimation, v is the velocity estimated by spectral Doppler and $S(v)$ is the amplitude of the velocity spectrum at velocity v. The v_{min} is the minimum velocity included in the summation, which is five cm/s here to avoid artifacts around the baseline, which can be seen in Fig. 6.4. The v_{max} is the maximum velocity included in the summation, which is 70 cm/s in our experiments.

6.3 Results

Fig. 6.2 shows the cyclic change in apparent speckle size within an ROI selected from the jugular vein blood flow images of subject #10. It can be seen that the apparent speckle size is greater when the image was scanned with the blood flow than the apparent speckle size when the image was scanned against the blood flow. The stretch effect is used by equation (6.1) for blood flow velocity estimation. The dashed lines are the raw data of speckle sizes. The solid lines are filtered data of speckle sizes with low-pass filter

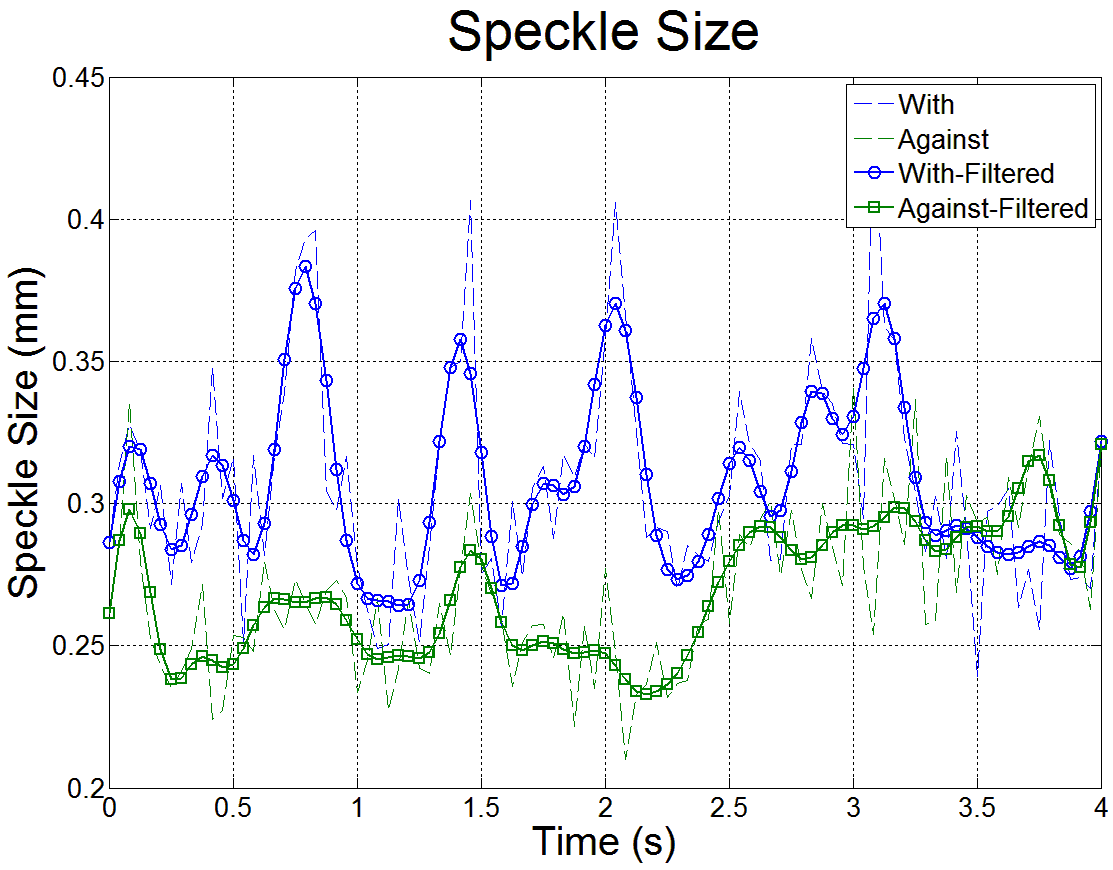

Fig. 6.2. Speckle size of the jugular vein blood flow images collected with (top signal) and against (bottom signal) the blood flow in (different) four-second intervals. The dashed lines are the raw data of speckle size of the ROI and the solid lines are the filtered data of speckle sizes with a low pass filter, subject #8.

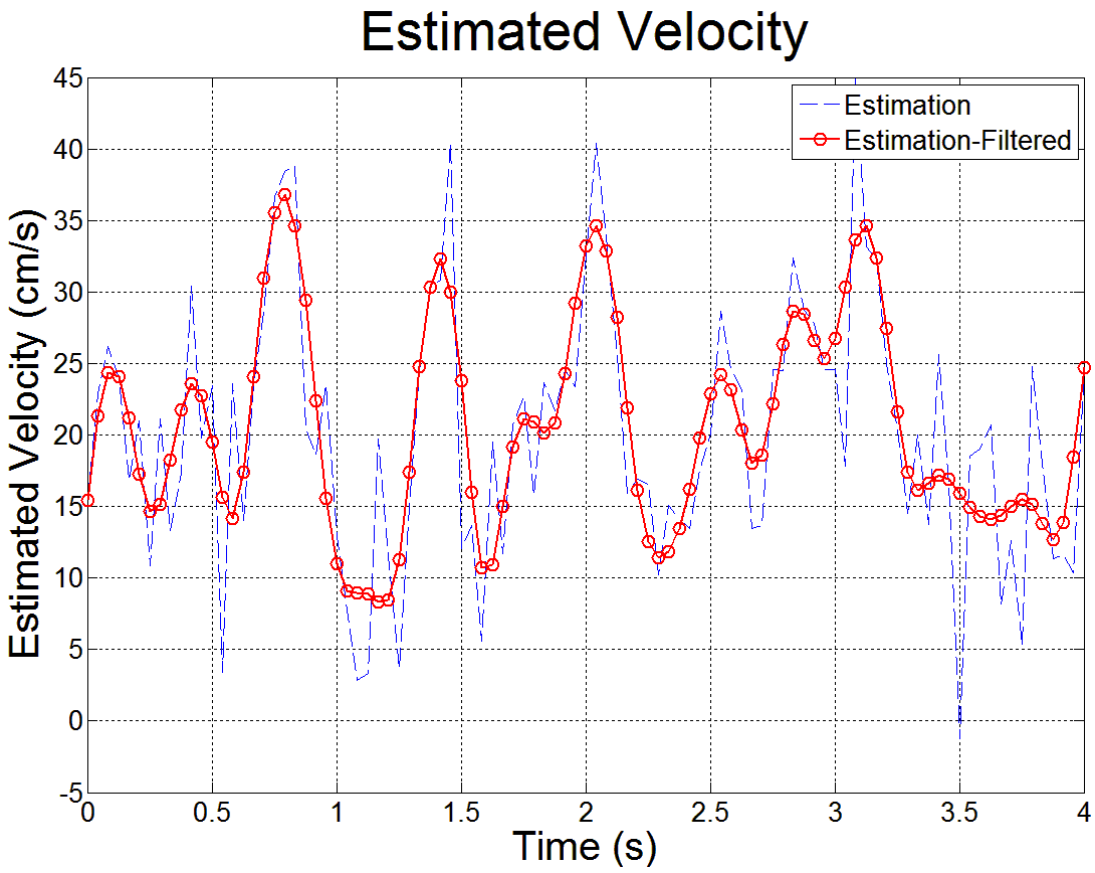

Fig. 6.3. Estimated blood flow velocity in the jugular vein using speckle size estimation. The dashed line is the raw estimated blood flow velocity data and the solid line is estimated blood flow velocity data after low-pass filtering. Subject #8.

(5^{th} order low-pass IIR Butterworth filter, -3dB cutoff frequency = 3.6 Hz) to reduce the noise of each signal. Fig. 6.3 shows the estimated blood flow velocity by speckle size estimation. Here, the dashed line is the raw estimated blood flow velocity data and the solid line is the estimated blood flow velocity data after a low-pass filtering. Spectral Doppler data were collected from the same subject. The velocity spectrum of the jugular vein blood flow is shown in Fig. 6.4 and the first moment of the velocity spectrum is shown in Fig. 6.5. It is important to note that the data were not taken during the same four-second interval, therefore the local maxima and minima of the velocity estimated by

speckle size estimation is not expected to correlate with the spectral Doppler data. The comparison is mainly useful to show that the average energy in each signal is different.

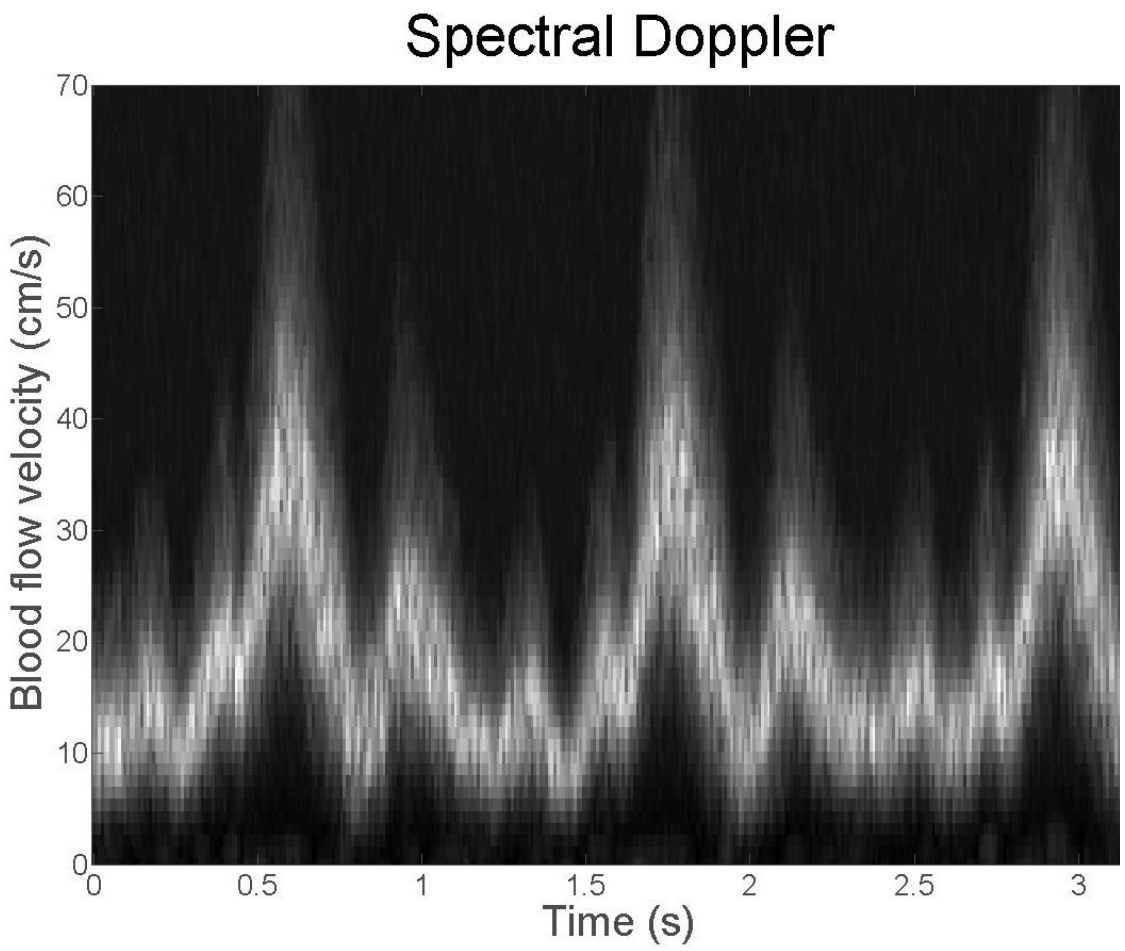

Fig. 6.4. Spectral Doppler data of the jugular vein blood flow. Subject #8.

The same analyses were done on data collected from each of the other subjects. To evaluate the performance of blood flow velocity measurement using speckle size estimation, the mean velocities estimated by speckle size estimation and spectral Doppler were both calculated and plotted in Fig. 6.6. For each subject, the mean and standard deviation of the estimated blood flow velocity (ten observations of four-second intervals each) were plotted side by side for direct comparison.

6.4 Discussion

Four seconds of blood flow data were collected from each subject to cover several full cardiac cycles. It can be seen from Fig. 6.2 that the speckle size of the blood flow changes over time since the jugular vein blood flow velocity changes over time during each cardiac cycle. This can also be seen in Fig. 6.4, which contains three complete cardiac cycles in three seconds. As a result, the estimated blood flow velocity in the jugular vein using speckle size estimation also changes over time, which can be seen in Fig. 6.3. The estimated blood flow velocity ranges from 10 to 35 cm/s, which is similar to the range of results produced by spectral Doppler in Fig. 6.5.

A more detailed representation of the estimation performance of speckle size estimation can be seen in Fig. 6.6. The mean and standard deviation of the estimated blood flow velocity using speckle size estimation and spectral Doppler were plotted side by side for ten subjects. The mean jugular vein blood flow velocity is different for different subjects, which ranges from 10 to 35 cm/s. For each subject, it can be seen that estimated blood flow velocities using speckle size estimation and spectral Doppler are comparable to each other. The minimum difference between the mean estimated velocities is as low as 1.62 cm/s (8% and 9% of the mean velocity estimated by speckle size estimation and spectral Doppler respectively), which can be seen from subject six. The maximum difference between the mean estimated velocities is 6.6 cm/s (20% and 25% of the mean velocity estimated by speckle size and spectral Doppler respectively), which can be seen from subject three. Due to the pulsatility of the jugular vein blood flow, the estimated velocities of each subject are oscillating around the average values in different four-second intervals, which can be represented by the standard deviation of the

estimated velocities for each subject. The average standard deviation of the velocities estimated by speckle size estimation is 7.8 cm/s and the average standard deviation of the velocities estimated by spectral Doppler is 4.4 cm/s.

A non-parametric statistical hypothesis test, Wilcoxon signed-rank test, is used here to compare the estimation results between speckle size estimation and spectral Doppler (Wilcoxon 1985). We assume that the median difference between mean velocities estimated by speckle size estimation and spectral Doppler equals zero throughout ten subjects. The null and alternative hypotheses for this two-tail test can be defined as follows:

$$H_0\colon M_d = 0 \quad and \quad H_1\colon M_d \neq 0 \tag{6.2}$$

where M_d is the median difference between mean velocities estimated by speckle size estimation and spectral Doppler. Through the Wilcoxon signed-rank test, the calculated test statistic *W* is *11*. Since the number of subjects is *n = 10*, given a significance level α = 0.05 for this two-tail test, $z_{critical}$ is 1.86. Because $z = 0.53 < z_{critical}$, we would not reject the null hypothesis since there is no evidence of a difference between mean estimated velocities of speckle size estimation and spectral Doppler. The details of Wilcoxon test can be seen in the Appendix.

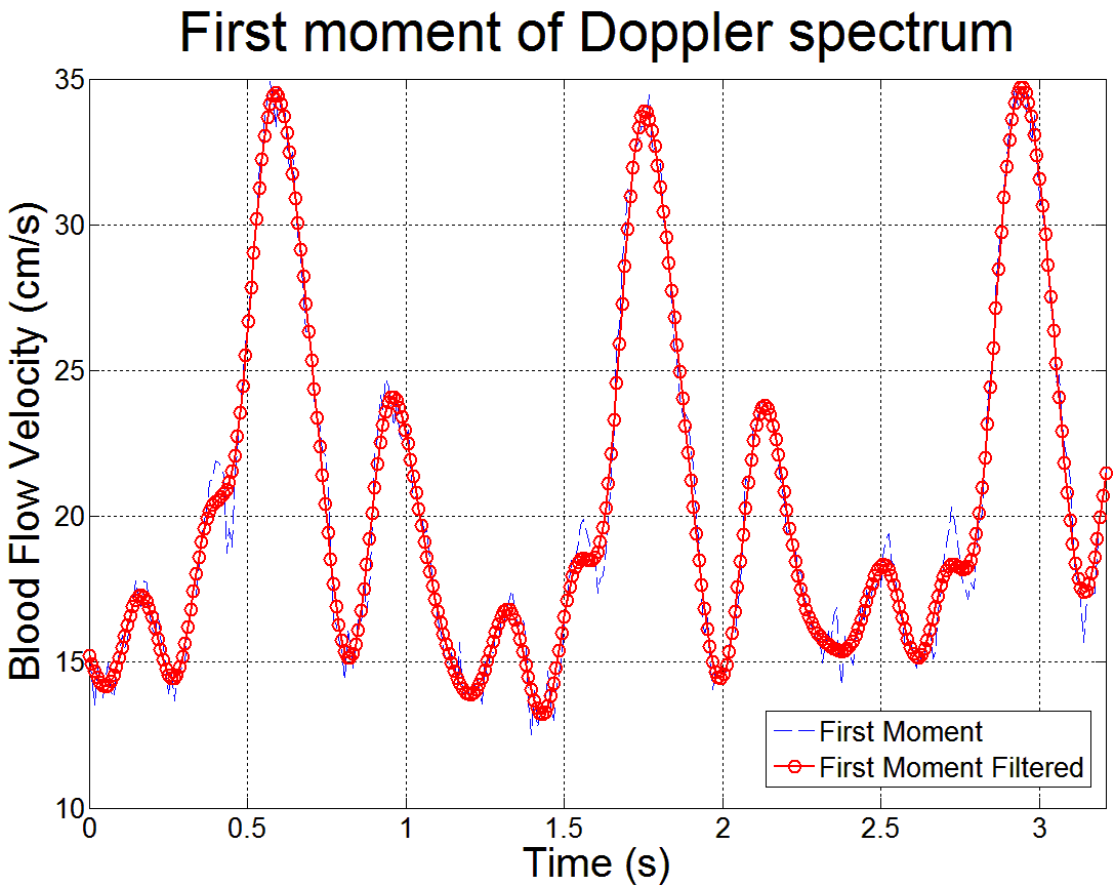

Fig. 6.5. The first moment of the velocity spectrum of the jugular vein blood flow. The dashed line is the first moment of the velocity spectrum and the solid line is the first moment of the velocity spectrum after low-pass filtering. Subject #8.

Speckle size estimation is based on the autocovariance function over the ROI and searching for the positional change which corresponds to the half maximum of the autocovariance function. For one estimation at a specific location, an ROI which has *M* pixels axially and *N* pixels laterally will be used for velocity estimation. The speckle size estimation requires $M(Lag_{half}+1)(2N-Lag_{half})/2$ multiplications and $M(Lag_{half}+1)(2N-Lag_{half})/2-(Lag_{half}+1)$ summations, where the Lag_{half} represents the position change which corresponds to the half maximum of the auto-covariance function. During the experiments, when the A-line increment of B-mode

scanning is about half the beam width of the transducer, the typical value of Lag_{half} is four to seven. For example, when the Lag_{half} is six, the number of multiplications required during speckle size estimation is *7MN – 21M* and the number of summations required during speckle size estimation is *7MN - 21M – 7*. In our experiments, the ROI for speckle size estimation has 20 pixels axially and 60 pixels laterally, so the number of multiplications is 7980 and the number of summations is 7973. For a comparable estimation at a specific location in color Doppler scenario, assume that 12 A-lines of blood flow are collected in succession, a resolution cell with axial length of *K* pixels is extracted from each A-line for autocorrelation and phase detection. The number of

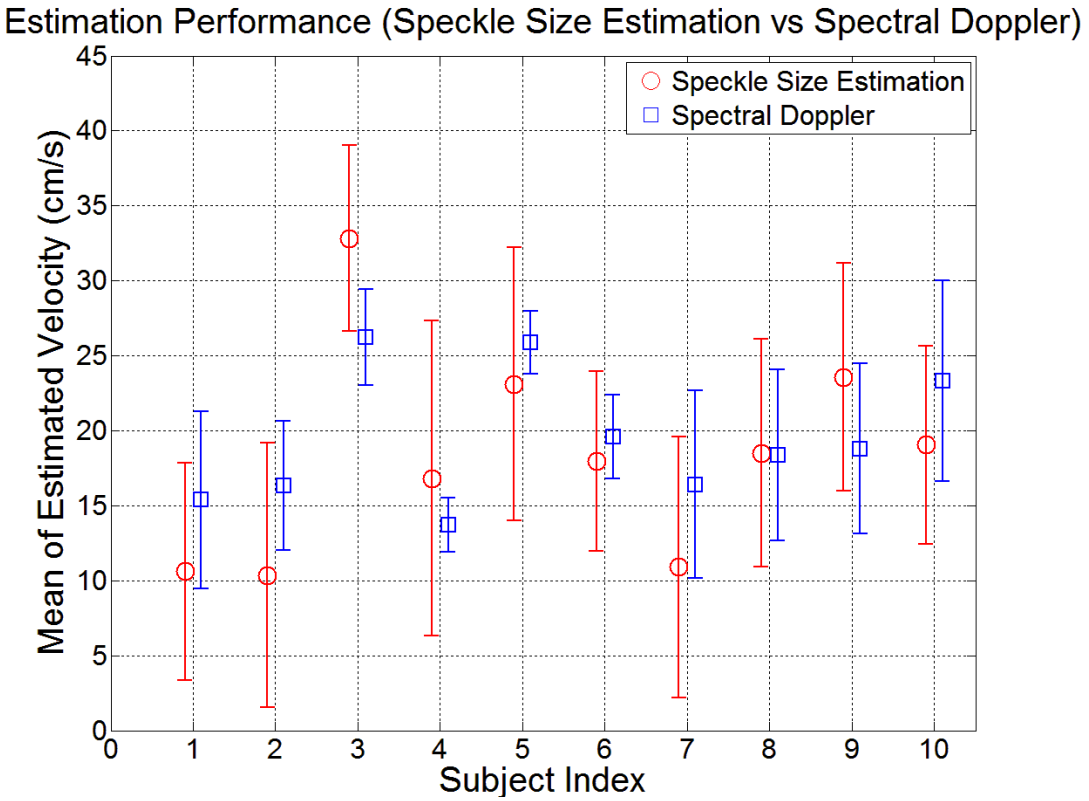

Fig. 6.6. The mean and standard deviation of estimated blood flow velocity using speckle size estimation and spectral Doppler, ten subjects.

multiplications required for autocorrelation is *11* and the number of summations required for autocorrelation is *12K+10*. For a typical color Doppler setup in the Antares Ultrasound Imaging System (sampling frequency = 40 MHz, center frequency = 5 MHz, number of pulse cycles = 20), the axial resolution cell has 40 pixels, so the number of multiplications required for autocorrelation is 11 and the number of summations required for autocorrelation is 491.

Comparing only the numbers of arithmetic operations does not show the computational complexity advantage of speckle size estimation compared with the color Doppler method. In particular, repeated data acquisition is required for Doppler based method. In spectral Doppler, 64-128 beams are repeatedly emitted and received to produce a full velocity spectrum. Similarly, 8-12 repeated frame acquisitions are required for velocity estimation in color Doppler. For speckle size estimation, only one B-mode image frame of the blood flow is required for the blood flow velocity measurement, which significantly reduces the time for data acquisition by a factor of seven to eleven compared with spectral Doppler method (that many fewer frame acquisition). The speed of arithmetic operations can be improved with growing computational power of modern ultrasound imaging systems (completing all the arithmetic operations for speckle size estimation before the next frame acquisition), while the repeated data acquisition time required by color Doppler method depends on the PRF, whose improvement is inherently limited by the speed of sound in human tissues. These initial analyses show the potential time savings of blood flow velocity estimation using speckle size estimation. A full investigation of the comparison between speckle size estimation and Doppler based

methods for a full frame blood flow measurement needs further experiments, which is out of the scope of this dissertation.

6.5 Conclusion

In this chapter, lateral blood flow velocity estimation based on speckle size estimation was tested on the human jugular vein *in vivo* and demonstrated to be comparable to spectral Doppler. Jugular vein blood flow data were collected from ten human subjects using a commercial ultrasound imaging system. Spectral Doppler data of the jugular vein blood flow were collected at the same time to compare with the estimation results of speckle size estimation. A Wilcoxon signed-rank test was used to compare the estimation results of speckle size estimation and spectral Doppler. The result showed that estimation results of speckle size estimation and spectral Doppler are comparable to each other. Instead of repeated beam emitting and receiving in Doppler based methods, speckle size estimation only requires one frame of a general B-mode image, which simplifies the system configuration and indicates potential time savings.

Appendix

Wilcoxon signed-rank test: "The Wilcoxon signed-rank test is a non-parametric statistical hypothesis test used when comparing two related samples, matched samples, or repeated measurements on a single sample to assess whether their population mean ranks differ (i.e. it's a paired difference test)" (Lowry, 2011). As described by Dowdy's book (Shirley et al. 2004), the procedure of Wilcoxon test can be described as follows:

"Let *N* be the sample size, the number of pairs. Thus, there are a total of *2N* data points. For *i = 1* to *N*, let $x_{1,i}$ and $x_{2,i}$ denote the measurements. Given the null hypothesize:

$$H_0: \text{median difference between the pairs is zero}$$

$$H_1: \text{median difference is not zero}$$

1. For *i = 1* to *N*, calculate $\left|x_{2,i} - x_{1,i}\right|$ and $sgn(\left|x_{2,i} - x_{1,i}\right|)$, where *sgn* is the sign function.
2. Exclude pairs with $\left|x_{2,i} - x_{1,i}\right| = 0$. Let N_r be the reduced sample size.
3. Order the remaining N_r pairs from smallest absolute difference to largest absolute difference.
4. Rank the pairs, staring with the smallest as 1. Ties receive a rank equal to the average of the ranks by span. Let R_i denote the rank.
5. Calculate the test statistic *W* (the absolute value of the sum of the singed ranks):

$$W = \left|\sum_{i=1}^{N_r} sgn(x_{2,i} - x_{1,i}) \cdot R_i\right|$$

6. As N_r increases, the sampling distribution of W converges to a normal distribution. Thus, for $N_r \geq 10$, a z-score can be calculated as follows:

$$z = \frac{W - 0.5}{\sigma_W}, \quad \sigma_W = \sqrt{\frac{N_r(N_r + 1)(2N_r + 1)}{6}}$$

If $z > z_{critical}$, reject H_0. For $N_r < 10$, W is compared with a critical value from the Wilcoxon signed-rank test reference table, if $W \geq W_{critical,N_r}$, reject H_0. Alternatively, a p-value can be calculated from enumeration of all possible combinations of W given N_r."

Chapter 7

2-D Blood Flow Velocity Estimation Using Apparent Speckle Pattern Angle

7.1 Introduction

In previous chapters, the change of apparent speckle size due to the direction and spatial rate of scanner A-line acquisition (scan velocity) was investigated. An algorithm which measures the lateral blood flow velocity was developed based on the speckle stretch effect. In this Chapter, the change of the apparent dominant angle of the speckle pattern in a straight vessel was investigated and a new method of two-dimensional blood

flow velocity estimation will be introduced. Different scan velocities were used for data acquisition from blood flow traveling at an angle relative to the ultrasound beam. The apparent angle of the speckle pattern changes with different scan velocities due to mis-registration between the ultrasound beam and scatterers. The apparent angle of the speckle pattern was resolved by line-to-line cross-correlation in the fast time (axial) direction on a region-of-interest (ROI) in each blood flow image and used to align the ROI. The resulting speckle size within the aligned ROI was calculated. The lateral component of the blood flow is shown to be closest to the scan velocity which gives the maximum speckle size and the apparent angle of speckle pattern collected by this scan velocity is the best estimate for the actual angle of blood flow. These two components produce two-dimensional blood flow velocity estimations. This method was studied through both computer simulation and experiments with a blood flow phantom. Nine scan velocities were used to collect blood flow data with velocity ranging from 33 to 98 cm/s and four beam-to-flow angles. In the simulated plug blood flow, the mean bias of angle estimation is below 2% with an average standard deviation of 3.6%. In the simulated parabolic blood flow, the angle of blood flow is overestimated due to the speckle correlation caused by flow gradients and the estimation bias increases with decreasing beam-to-flow angle, which has an average value of 8.8% and standard deviation of 10%. Due to the complexity of flow profiles in the blood flow phantom, the angle of blood flow is also overestimated and the mean bias is increased by a factor of two compared with simulated parabolic flow. For the velocity estimation results, the mean bias is below 5% with an average standard deviation of 4.6% in the simulated plug blood flow. In the simulated parabolic flow and blood flow phantom, the velocity is

underestimated due to speckle decorrelation. The mean bias of velocity estimation in the simulated parabolic flow is -6% with an average standard deviation of 11.2%. In the blood flow phantom, the mean bias of the velocity estimation is -5% with a higher average standard deviation of 21.5%. This method can resolve the angle and amplitude of two-dimensional blood flow simultaneously. The accuracy of the estimation can be further improved by using more scanning velocities.

In the previous chapters, flow purely lateral to the ultrasound beam was collected by scanning in the same direction as the blood flow. A similar scanning geometry was used in this chapter to collect data from blood flow with a specific angle relative to the ultrasound beam axis. Different scan velocities were used for data acquisition. An ROI was selected from each B-mode image, which can be seen in Fig. 7.1. Line-by-line cross-correlation in the fast time (axial) direction was used to resolve the apparent angle of speckle pattern, which can be described as follows:

$$R_{xy}(s) = \begin{cases} \sum_{n=0}^{N-s-1} x_{n+s} y_n^* & s \geq 0 \\ R_{yx}^* & s < 0 \end{cases} \tag{7.1}$$

where x and y represent two successive A-lines from the ROI and s is the lag between these two A-lines. The cross-correlation coefficient was calculated for each s, and the value s which gives the maximum cross-correlation coefficient between x and y was recorded as their distance shift d_{xy}. This process was done for every pair of successive A-lines in the ROI and the d_{xy} with the highest frequency (mode) of occurrence was set as the overall distance shift of the ROI, which is d_{ROI}. Given the line increment of scanning, which is represented by d_{incre}, the apparent dominant angle of the speckle pattern was calculated as:

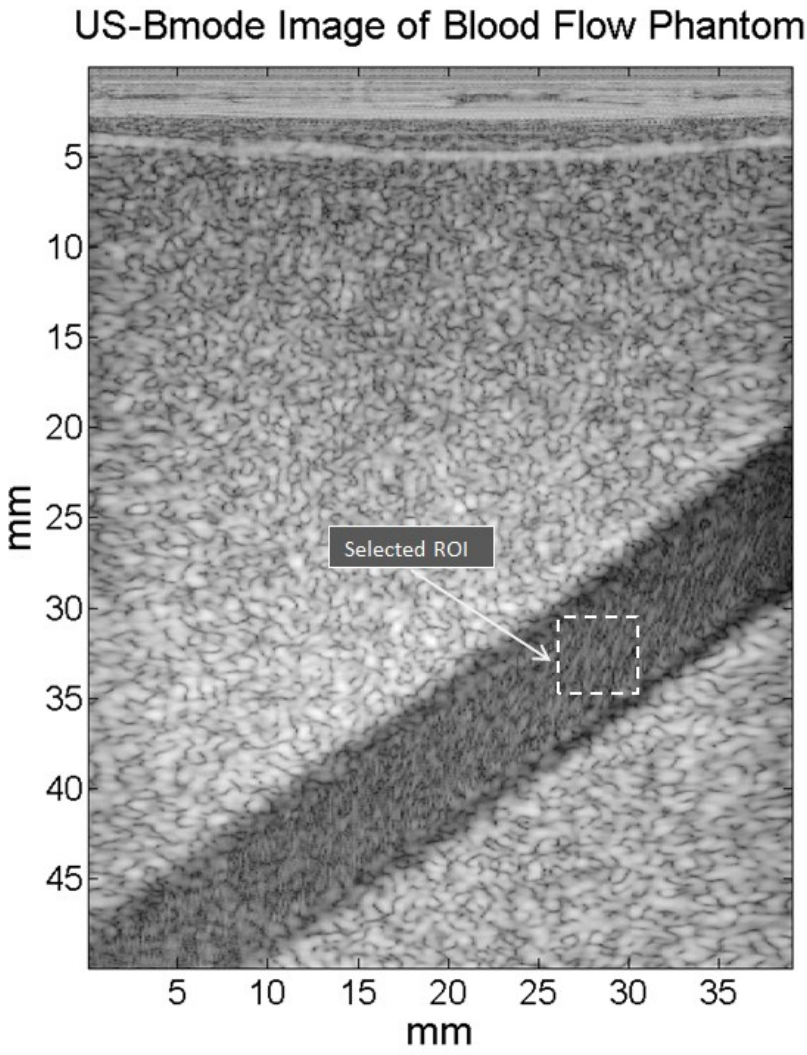

Fig. 7.1. A Region-of-interest (ROI) is selected from every US B-mode image of the blood flow phantom, which covers an area corresponding to 3 mm × 4.2 mm.

$$\theta_a = tan^{-1}(\frac{d_{ROI}}{d_{incre}}) \tag{7.2}$$

As described above, the apparent dominant angle of speckle pattern is estimated by line-to-line cross-correlation in the fast time (axial) direction on the speckle pattern of the blood flow images. However, our experiments showed that the apparent angle θ_a is not always the same as the actual blood flow angle θ. They only equal each other when

the lateral component of blood flow is the same as scan velocity. The relationship between these two angles can be shown as follows:

$$\begin{cases} \theta_a < \theta & (V_{lateral} > V_{scan}) \\ \theta_a = \theta & (V_{lateral} = V_{scan}) \\ \theta_a > \theta & (V_{lateral} < V_{scan}) \end{cases} \tag{7.3}$$

The reason for this phenomenon is visually demonstrated in Fig. 7.2. The θ is the actual angle of blood flow, and θ_a is the apparent angle of the blood flow. When the lateral component of blood flow is lower than the scan velocity, which is shown in Fig. 7.2, the ultrasound beams are collecting data laterally faster than the scatterers are moving. Since the ultrasound beam is broad in space, the transducer can receive the reflected ultrasound echo even if the scatterers are not precisely at the focal position of each beam. The correct depth information of the scatterers can be preserved; however, errors will occur in the lateral positions of these scatterers. In Fig. 7.2, since the lateral component of blood flow velocity is less than the scan velocity, the apparent lateral position of the scatterers will be shifted to the right. As shown by the circles, these positions will be interpreted as the scatterers' positions by the transducer. As a result, the apparent angle of speckle pattern will be greater than the actual blood flow angle. A similar phenomenon will occur when the lateral component of blood flow velocity is greater than the scan velocity. In this condition, the apparent angle of speckle pattern will be less than the actual blood flow angle.

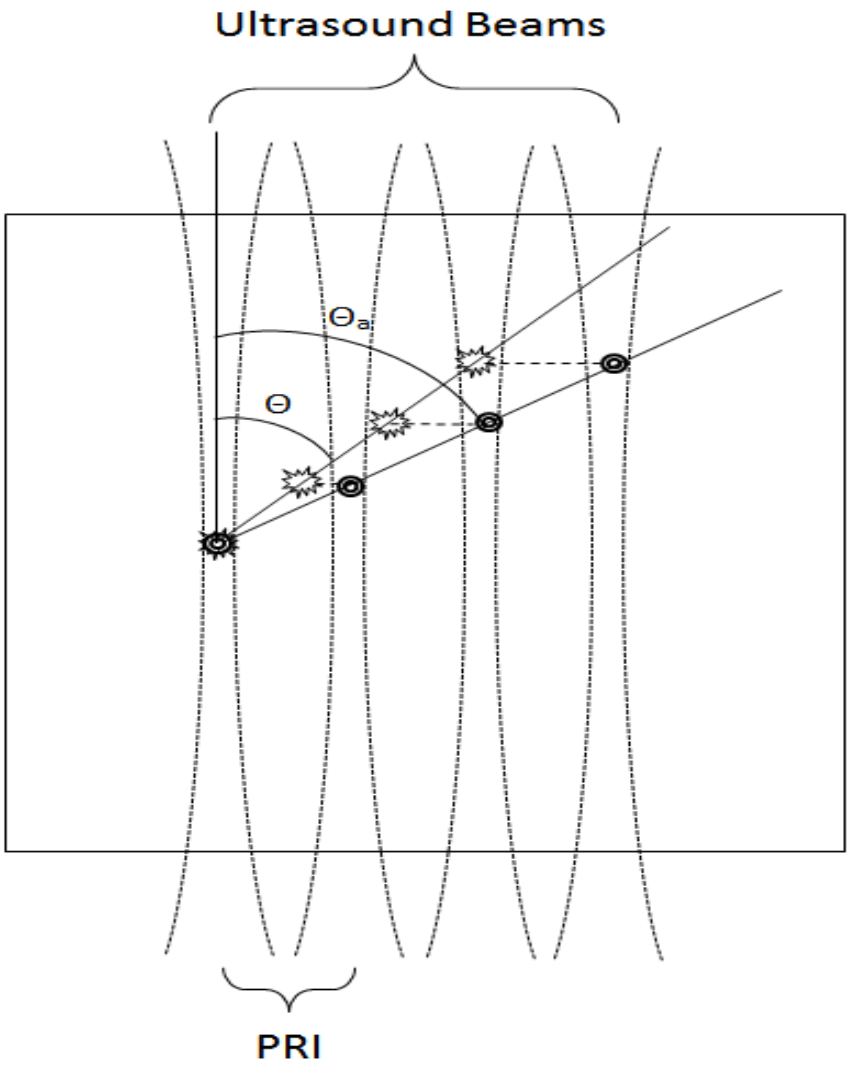

Fig. 7.2. Representation of the difference between apparent blood flow angle and actual blood flow angle. “Burst” makers show actual position of an individual scatterer, and round circles show where the scatterer is interpreted as existing in the space.

As discussed in previous chapters, the apparent speckle size increases when the scan velocity is close to the lateral component of blood flow since the lateral rate of ultrasound beam movement becomes completely correlated with the movement of scatterers. To compare the apparent speckle size of blood flow images collected by different scan velocities, the ROI was first aligned by the apparent angle of the speckle pattern, which means shifting each A-line by d_{ROI} to make the speckle pattern in the ROI

to be purely lateral, as shown in Fig. 7.3. Then the speckle size is calculated by the full-width at half-maximum (FWHM) of the autocovariance function (ACVF) of the ROI (Xu and Bashford 2009a). The speckle size will change for different scan velocities. When the speckle size reaches its maximum value, the lateral component of the blood flow equals the scan velocity and the apparent speckle angle equals the actual blood flow angle. Thus, in this method, two-dimensional blood flow velocity estimates are made.

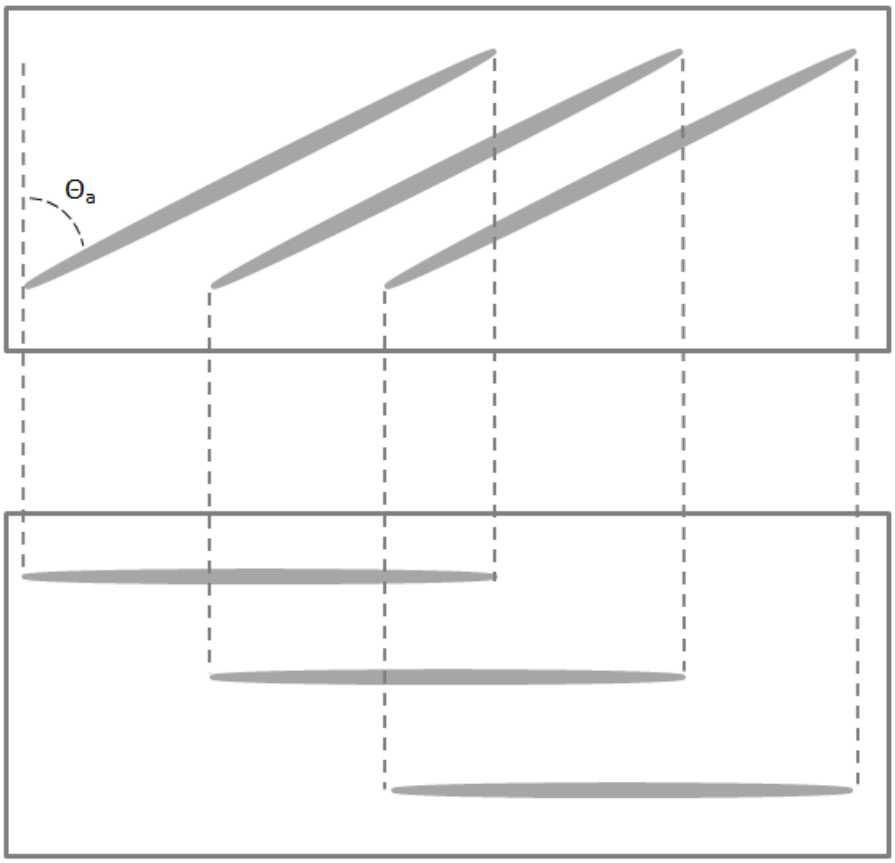

Fig. 7.3. Each ROI is aligned by cross-correlation, and the apparent flow angle θ_a is calculated during alignment.

7.2 Materials and Methods

7.2.1 Multi-PRF scanning and data acquisition

A commercial flow phantom (Optimizer RMI 1425, Gammex, Middleton, WI), was used to simulate blood with a parabolic flow profile. The blood-mimicking fluid which has acoustic properties similar to blood (speed of sound 1550 m/s, density 1.03 g/mL) was pumped through a tube (5 mm inside diameter, 1.25 mm thickness, 40^{o} from horizontal) in the phantom, and the tube was surrounded by tissue mimicking material (speed of sound 1540m/s, attenuation 0.5 dB/cm/MHz). A SONOLINE Antares ultrasound imaging system (Siemens Medical Solution, Ultrasound Division, Issaquah, WA) was used for data acquisition. The VF7-3 linear array transducer (192 elements, 3.33 MHz center frequency) was set to focus on the tube located in the blood flow phantom, with a total imaging depth of 5 cm. The Axius Direct Ultrasound Research Interface (URI) was employed to transfer ultrasound data (post-beamformation but before any down-stream processing) to a computer for further analysis. Imaging parameters can be accessed from the header information given by the URI, including frame rate, number of A-lines and beam spacing. Thus, the scan velocity can be calculated given the values of these parameters. In our experiments, nine scan velocities were used, which were 22, 26, 31, 37, 46, 52, 63, 75 and 91 cm/s. Six different flow velocities were set to the flow phantom, which were 33, 41, 55, 65, 80 and 98 cm/s. Two angles between the blood flow and the ultrasound beam were used, which were 50^{o} and 70^{o}.

A Field II simulation (Jensen 1996b; Jensen 1998) was also used to generate blood flow data for the experiments. Ten scatterers were assigned to each resolution cell over a

3-D volume to produce a fully developed scatterer field. Four angles between the blood flow and the ultrasound beam were simulated, which were 10^o, 30^o, 50^o and 70^o. Other parameters used in the simulation are similar to the SONOLINE Antares Ultrasound Imaging System and the flow phantom as mentioned above, which can be seen in Table 7.1. Two flow conditions were simulated: the first flow condition had a plug flow distribution in the vessel. The second flow condition had a parabolic velocity distribution in the flow with maximum velocity at the center and decreasing to zero at the boundary of the vessel, producing a similar lateral gradient to the flow velocity in the blood flow phantom.

TABLE 7.1. PARAMETERS OF TRANSDUCER AND BLOOD FLOW PHANTOM USED IN SIMULATION.

Transducer	
Center frequency	3.33 MHz
Element height	7.5 mm
Element width	0.203 mm
Kerf	25 μm
Number of elements	192
Sampling frequency	40 MHz
Blood flow phantom	
Speed of sound	1550 m/s
Angle of vessel	50 degrees relative to the ultrasound beam axis
Diameter of vessel	5 mm
Blood flow velocity	33, 41, 55, 65, 80 and 98 cm/s

7.2.2 Resolving flow angle and lateral flow component

Ten images were simulated or collected for each scan. In each image, an ROI was selected from the tube, with an axial length of 3 mm and a lateral length of 4.2 mm, as shown in Fig. 7.1. This ROI was then used to calculate the apparent dominant angle of the speckle pattern. After ROI-alignment by the dominant angle of the speckle pattern, the speckle size of the blood flow images collected by different scan velocities was then calculated to resolve the lateral component and actual angle of the blood flow.

7.3 Results

Fig. 7.4 shows the apparent angle of the speckle pattern and the speckle size of aligned blood flow images when the angle between blood flow and ultrasound beam axis is 50^{o}. Fig. 7.4(a) shows the apparent angle of the speckle pattern of simulated plug flow collected by different scan velocities. Fig. 7.4(b) shows the apparent angle of the speckle pattern of simulated parabolic flow collected by different scan velocities, and Fig. 7.4(c) shows the apparent angle of the speckle pattern of blood flow phantom collected by different scan velocities. It can be seen that the apparent angle of speckle pattern is less than the actual blood flow angle when the scan velocity is less than the lateral component of blood flow and greater than the actual blood flow angle when the scan velocity is greater than the lateral component of blood flow. When the scan velocity equals the lateral component of blood flow, the apparent angle of the speckle pattern equals the actual angle of blood flow.

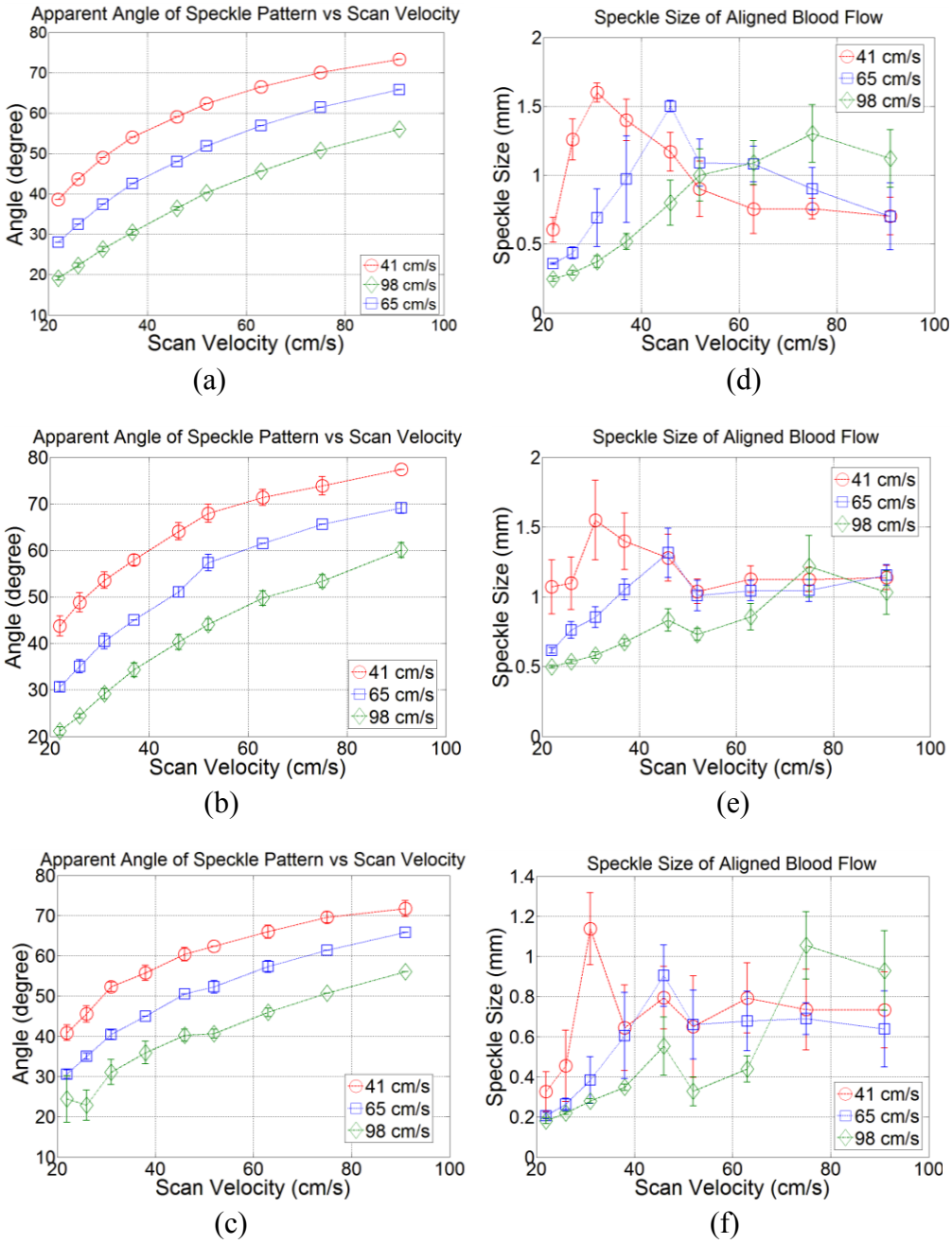

Fig. 7.4. (a) – (c) the apparent angle of the speckle pattern of the blood flow (41, 65 and 98 cm/s, 50^{o} relative to the ultrasound beam) collected by different scan velocities. (a) Simulated plug flow, (b) Simulated parabolic flow and (c) Blood flow phantom. (d) – (f) the speckle size of the aligned blood flow image. (d) Simulated plug flow, (e) Simulated parabolic flow and (f) Blood flow phantom.

Fig. 7.4(d) shows the speckle size of the aligned blood flow image of simulated plug flow. Fig. 7.4(e) shows the speckle size of the aligned blood flow image of simulated parabolic flow and Fig. 7.4(f) shows the speckle size of the aligned blood flow image of the blood flow phantom. It can be seen that the speckle size of aligned blood flow is changing with different scan velocities and it reaches the maximum value when the scan velocity equals the lateral component of blood flow.

Similar results on blood flow with an angle of 70^{o} relative to the ultrasound beam axis are shown in Fig. 7.5. The relationship between the apparent angle of the speckle pattern and scan velocities is shown in Fig. 7.5(a), Fig. 7.5(b), Fig. 7.5(c) for simulated plug flow, simulated parabolic flow and blood flow phantom. The relationship between the speckle size of the aligned blood flow image and scan velocities is shown in Fig. 7.5(d), Fig. 7.5(e) and Fig. 7.5(f) for simulated plug flow, simulated parabolic flow and blood flow phantom.

In Fig. 7.4 and Fig. 7.5, the lateral component of blood flow and actual blood flow angle can be estimated by searching for the peak speckle size of the aligned blood flow image collected by different scan velocities. Using these results, the estimated velocities were plotted versus actual velocities in Fig. 7.6. Fig. 7.6(a) shows the reference line and estimated velocities versus actual velocities in simulated plug flow. Fig. 7.6(b) shows the reference line and estimated velocities versus actual velocities in simulated parabolic flow and Fig. 7.6(c) shows the reference line and estimated velocities versus actual velocities in the blood flow phantom. These graphs show the mean and standard deviation of estimated velocities. Additional results including the mean and standard deviation of estimation bias can be seen in Table 7.2.

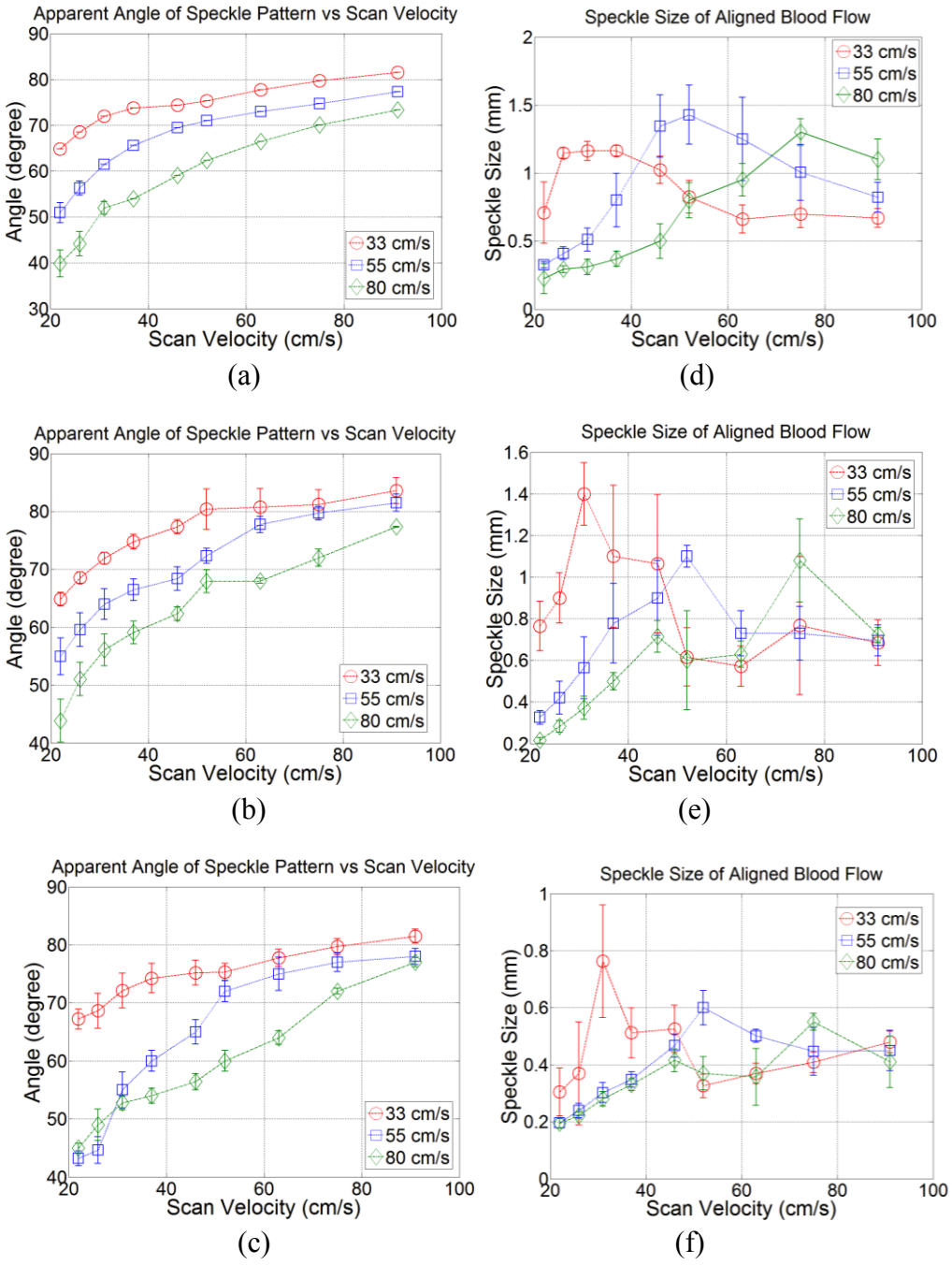

Fig. 7.5. (a) – (c) the apparent angle of the speckle pattern of the blood flow (33, 55 and 80 cm/s, 70^{o} relative to the ultrasound beam) collected by different scan velocities. (a) Simulated plug flow, (b) Simulated parabolic flow and (c) Blood flow phantom. (d) – (f) the speckle size of the aligned blood flow image. (d) Simulated plug flow, (e) Simulated parabolic flow and (f) Blood flow phantom.

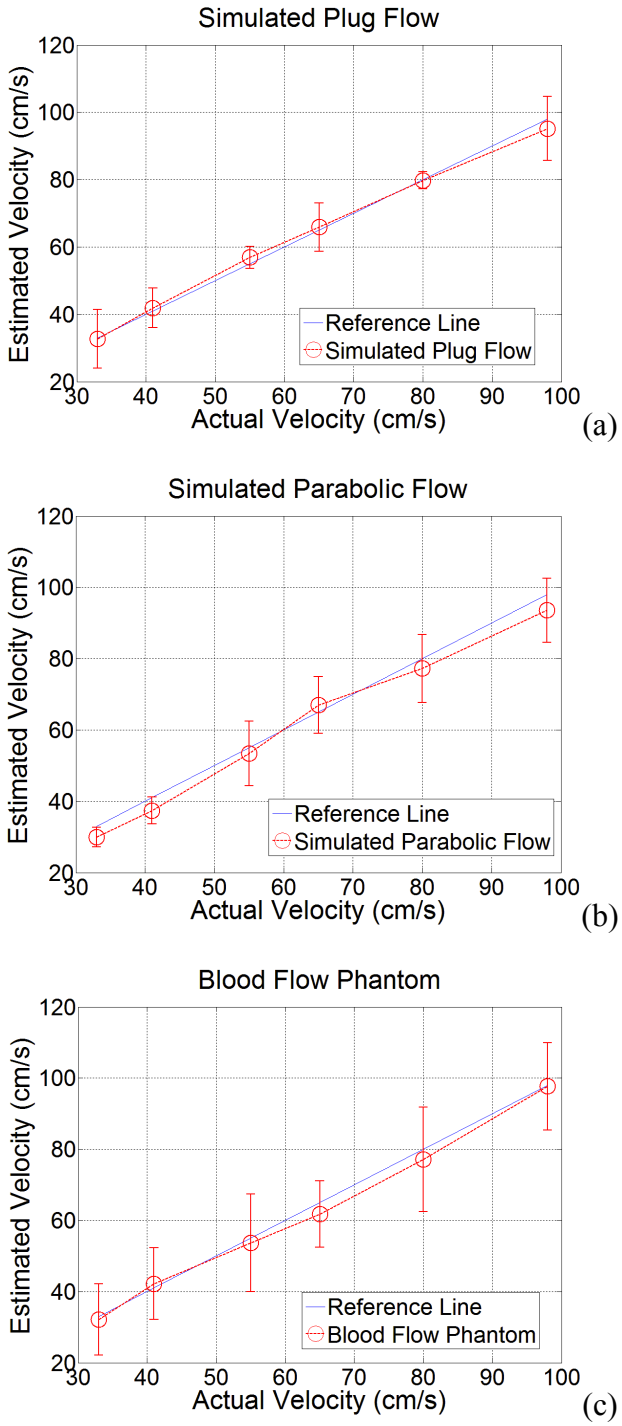

Fig. 7.6. Estimated velocities versus actual velocities. (a) Simulated plug flow, (b) simulated parabolic flow, (c) blood flow phantom.

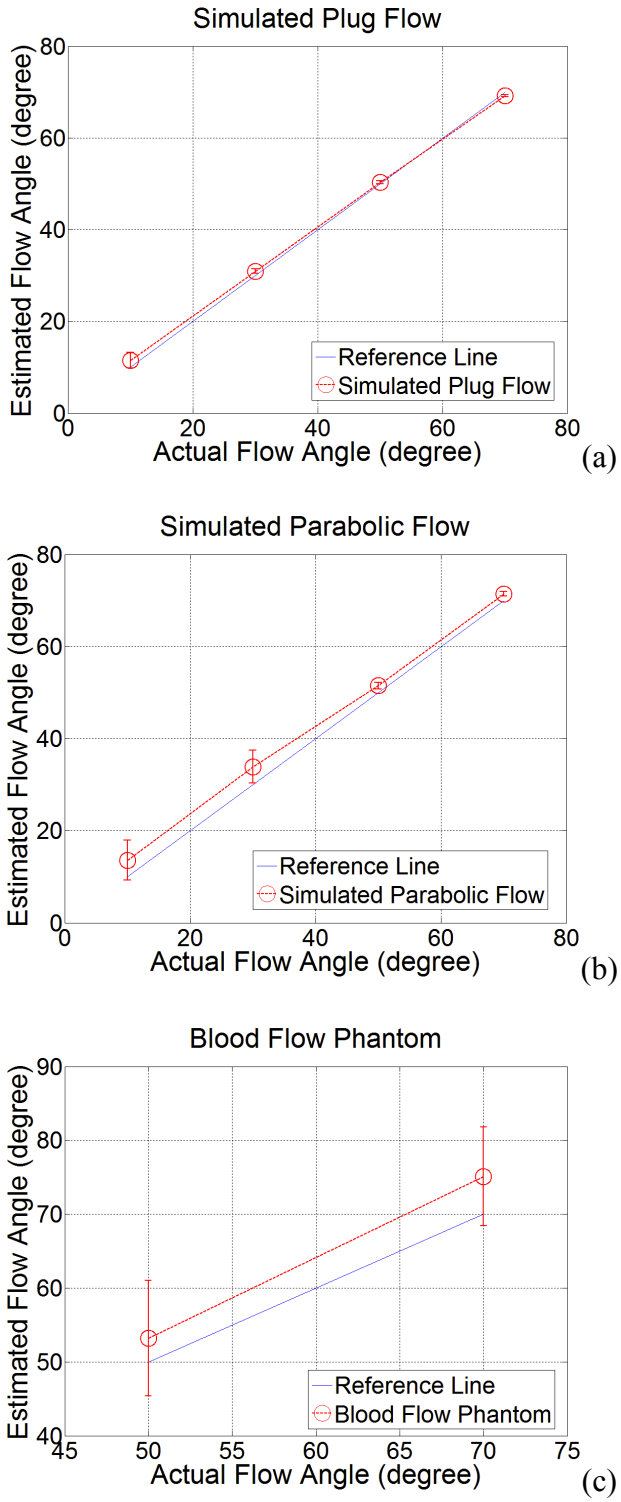

Fig. 7.7. Estimated flow angle versus actual flow angle. (a) Simulated plug flow, (b) simulated parabolic flow, (c) blood flow phantom.

TABLE 7.2. THE MEAN AND STANDARD DEVIATION OF VELOCITY ESTIMATION BIAS

Simulated Plug Flow						
Actual velocity (cm/s)	33	41	55	65	80	98
Mean bias (% of actual)	-0.9	2.2	3.4	1.4	-0.3	-2.9
SD of bias (% of actual)	6.5	1.4	5.9	1.3	2.1	9.6
Simulated Parabolic Flow						
Actual velocity (cm/s)	33	41	55	65	80	98
Mean bias (% of actual)	-12.2	-7.8	-8.3	3.4	-5.9	-4.6
SD of bias (% of actual)	8.3	9.1	16.4	12.1	11.9	9.2
Blood Flow Phantom						
Actual velocity (cm/s)	33	41	55	65	80	98
Mean bias (% of actual)	-3.4	6.1	-8.5	-15.1	-6.8	-3.5
SD of bias (% of actual)	30.5	24.7	24.9	18.3	17.3	12.5

TABLE 7.3 THE MEAN AND STANDARD DEVIATION OF ANGLE ESTIMATION BIAS

Simulated Plug Flow				
Actual angle (degree)	10	30	50	70
Mean bias (% of actual)	1.5	0.3	0.3	0.6
SD of bias (% of actual)	3.2	2.1	5.1	4.1
Simulated Parabolic Flow				
Actual angle (degree)	10	30	50	70
Mean bias (% of actual)	16.3	11.2	4.5	3.2
SD of bias (% of actual)	23.4	8.2	7.5	3.15
Blood Flow Phantom				
Actual angle (degrees)	50		70	
Mean bias (% of actual)	7.1		7.3	
SD of bias (% of actual)	9.4		4.5	

Fig. 7.7 shows the relationship between the estimated blood flow angle and actual blood flow angle. Fig. 7.7(a) shows the estimated blood flow angle versus actual blood flow angle in the simulated plug flow data. Fig. 7.7(b) shows the estimated blood flow angle versus actual blood flow angle in the simulated parabolic flow and Fig 7.7(c) shows

the estimated blood flow angle versus actual blood flow angle in the blood flow phantom. They were plotted with a reference line to represent the estimation accuracy. Further details of the flow angle estimation bias can be seen in Table 7.3.

7.4 Discussion

The speckle size of the aligned blood flow image changes with different scan velocities, which can be seen in Fig. 7.4(e)-(f) and Fig. 7.5(e)-(f). Generally, the maximum speckle size of aligned blood flow is around 1.5 mm in the simulated plug flow. In the simulated parabolic flow and blood flow phantom, this value decreased to 1.2 mm and 1.0 mm separately. The reason is that the flow gradients in the simulated parabolic flow and blood flow phantom cause speckle decorrelation, which decreases the speckle size. Nevertheless, since the speckle pattern will be maximally correlated when the scan velocity equals the lateral component of blood flow, searching for the maximum speckle size of aligned blood flow image can resolve the lateral component of blood flow velocity. In Fig. 7.4, the maximum speckle size of aligned blood flow image occurs when the scan velocities are 31, 52 and 75 cm/s. These scan velocities are equal to the lateral component of blood flow with an angle of 50^{o} relative to the ultrasound beam axis ($41 \times \sin 50^{o} = 31$, $65 \times \sin 50^{o} = 50$ and $98 \times \sin 50^{o} = 75$ cm/s). Similar results can be seen in Fig. 7.5. When the scan velocities are 31, 52 and 75 cm/s, the speckle size of the aligned blood flow image reaches its maximum value since these scan velocities equal the lateral component of blood flow with an angle of 70^{o} relative to the ultrasound beam axis ($33 \times \sin 70^{o} = 31$, $55 \times \sin 70^{o} = 52$ and $80 \times \sin 70^{o} = 75$ cm/s).

The results in Fig. 7.4(a)-(c) and Fig. 7.5(a)-(c) show that the apparent angle of speckle pattern increases with scan velocity. The reason is the mis-registration between the ultrasound beam scan and scatterer movement (refer to Section 7.1). When the scan velocities are 31, 52 and 75 cm/s, which give the maximum speckle size of aligned blood flow image, the apparent angle of speckle pattern equals the actual angle of blood flow, which is 50^o in Fig. 7.4 and 70^o in Fig. 7.5. In the simulated plug flow, the estimation error of blood flow angle is low, which can be seen in Fig. 7.4(a) and Fig. 7.5(a). In Fig. 7.4(a), the estimated blood flow angle is 49.2^o, 51.3^o and 50.7^o when the angle between the blood flow and ultrasound beam axis is 50^o. In Fig. 7.5(a), the estimated blood flow angle is 71.3^o, 70.8^o and 70.1^o when the angle between the blood flow and ultrasound beam axis is 70^o. However, in simulated parabolic flow and the blood flow phantom, the estimated blood flow angle is generally greater than the actual angle of blood flow. The reason is that the flow gradient causes speckle decorrelation in the axial direction, which will reduce d_{ROI} during cross-correlation. Since the apparent angle of speckle pattern is calculated by (7.2), when d_{ROI} decreases, the estimated angle of blood flow will be greater than the actual angle of blood flow. This can also be seen in Fig. 7.7. Fig. 7.7(a) shows that the estimated angle of simulated plug flow is close to the actual angle with mean bias below 2%. However, in the simulated parabolic flow, the estimation bias increases due to the flow gradient. Furthermore, the estimation bias increases with decreasing angle angle between the blood flow and ultrasound beam axis. We reason that decorrelation in the axial direction caused by the flow gradient in a parabolic flow increases with decreasing angle between blood flow and the ultrasound beam axis. Since the angle of blood flow is estimated by axial cross-correlation on the ROI, when the angle between the blood flow

and ultrasound beam axis decreases, the angle estimation bias increases. Fig. 7.7(c) shows the estimated flow angle versus actual flow angle in the blood flow phantom. Compared with simulated parabolic flow, it can be seen that the estimation bias increases due to the increasing complexity of the flow profile in the blood flow phantom. Details of the angle estimation bias can be seen in Table 7.3. It shows that the mean bias of angle estimation ranges from 0.3% to 1.5% with an average value of 0.4%. The standard deviation of bias ranges from 2.1% to 5.1% with an average value of 3.6%. In the simulated parabolic flow, due to the flow gradient, the mean bias of angle estimation ranges from 3.2% to 16.3% with an average value of 8.8%. The standard deviation of bias ranges from 3.15% to 23.4% with an average value of 10.5%. As discussed above, the estimation bias increases by a factor of six when the angle between the blood flow and the ultrasound beam axis decreases from 70^{o} to 10^{o}. In the blood flow phantom, the estimation bias is increased by a factor of two compared with simulated parabolic flow due to the complexity of the flow profile in the blood flow phantom.

The relationship between estimated velocities and actual velocities can be seen in Fig. 7.6. In simulated plug flow, the estimated velocities distribute close to the reference line. However, in the simulated parabolic flow and blood flow phantom, most of the estimated velocities are lower than the actual blood flow velocities; the reason is that axial speckle decorrelation causes overestimation of blood flow angle as discussed above. Given the lateral component of blood flow velocity, when the angle of blood flow is overestimated, the blood flow velocity will be underestimated. Details of the estimation bias can be seen in Table 7.2. In simulated plug flow, the mean of the estimation bias ranges from -3% to 4%, with an average value of 2% and the standard deviation of the

estimation bias ranges from 1.3% to 9.6%, with an average value of 4.6%. Due to the flow gradient in the simulated parabolic flow, the mean of the estimation bias ranges from -12.2% to 3.4%, with an average value of -5.9%. Most of the estimation bias is negative since the blood flow velocities were underestimated as discussed above. The standard deviation of estimation bias also increased, which ranges from 8.3% to 16.4%, with an average value of 11.2%. In the blood flow phantom, the complexity of flow profile causes more speckle decorrelation. As a result, the mean of the estimation bias ranges from -15.1% to 3.1%, with an average value of -5.2%. The standard deviation of estimation bias ranges from 12.5% to 30.5%, with an average value of 21.5%. Since the underestimation of blood flow velocity is a result of speckle decorrelation, future studies may quantitatively investigate and compensate the underestimation to improve the accuracy of velocity estimation.

Spectrum analysis was also investigated in this experiment. An ROI was selected from the blood flow image, the 2-D power spectrum of the ROI was calculated and compare for different scan velocities. The results showed that when the scan velocity equals the lateral component of the blood flow, the speckle pattern of the blood flow image was most spatially coherent since the scatterers and ultrasound beam were most correlated in this condition, and the power spectrum of the blood flow image was more concentrated. When the scan velocity was higher or lower than the lateral component of blood flow, the speckle pattern was complex due to mis-registration between scatterers and the ultrasound beam. As a result, the power spectrum of the blood flow image was less concentrated, which can be seen in Fig. 7.8 and Fig. 7.9. Fig. 7.8 shows the results from Filed II simulation where the A-line increment was less than one-fourth of the

lateral beam width. It can be seen that the power spectrum is most concentrated when the scan velocity (50 cm/s) is close to the lateral component of the blood flow ($70 \times \sin 50^{o} = 53$ cm/s). Fig. 7.9 shows the results from phantom experiments, where the A-line increment ranges from one half to one of the lateral beam width due to the limitation of the Antares ultrasound imaging system. It can be seen that the power spectrum is most concentrated when the scan velocity (52 cm/s) is close to the lateral component of the blood flow ($65 \times \sin 50^{o} = 50$ cm/s). However, aliasing occurs since the blood flow was not adequately sampled (the maximum lateral spatial frequency of the speckle pattern is greater than the Nyquist frequency). These results indicate another potential method for 2-D blood flow velocity estimation. A high lateral resolution ultrasound imaging system may be used for data acquisition in future studies, which will eliminate aliasing for spectrum analysis.

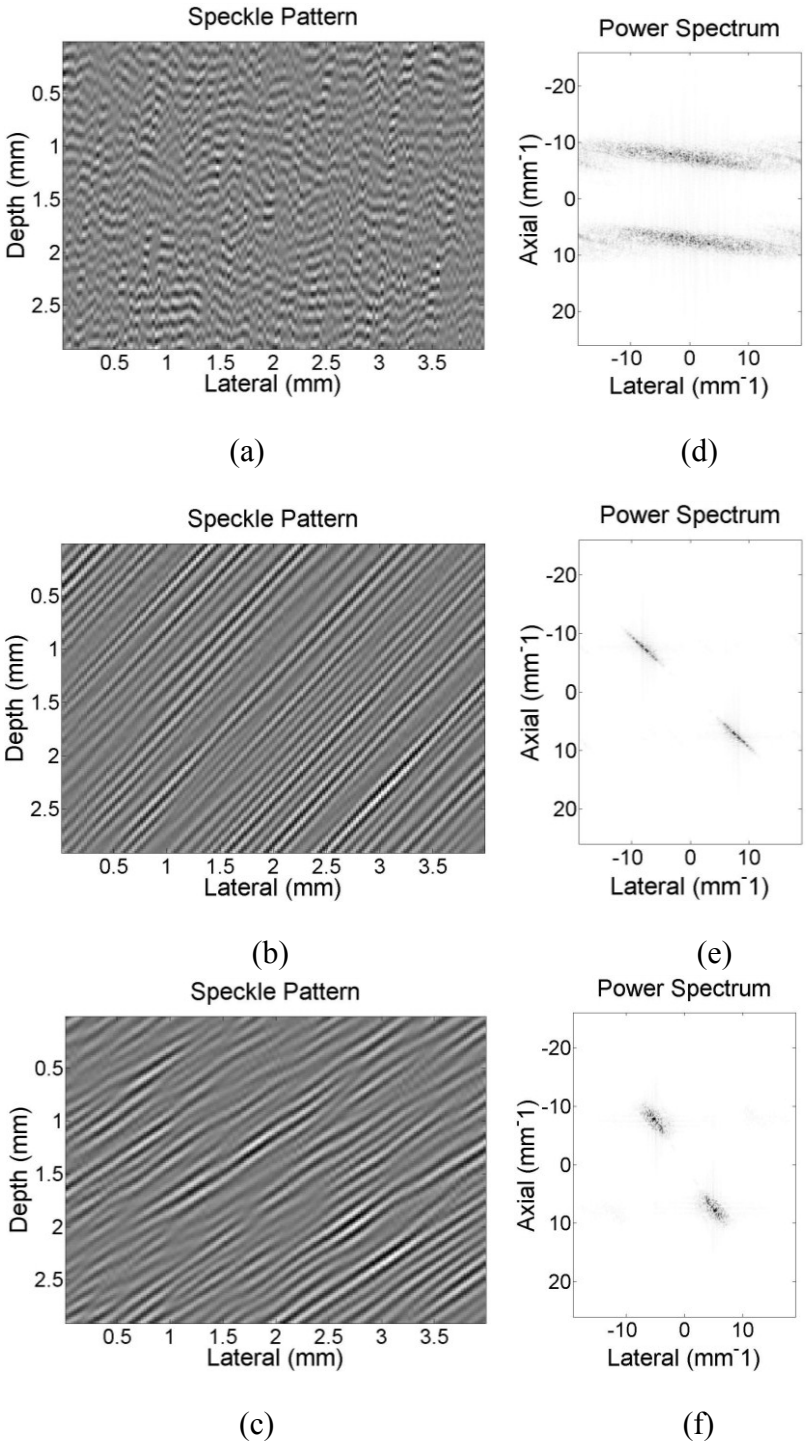

Fig. 7.8. (a) – (c) the speckle pattern of the blood flow (70 cm/s, 50^{o} relative to the ultrasound beam) collected by different scan velocities. Scan velocity is (a) 20 cm/s, (b) 50 cm/s and (c) 80 cm/s. (d) – (f) the power spectrum of the speckle pattern. Scan velocity is (d) 20 cm/s, (e) 50 cm/s and (f) 80cm/s. Simulated plug blood flow with A-line increment equal to one-fourth of the lateral beam width.

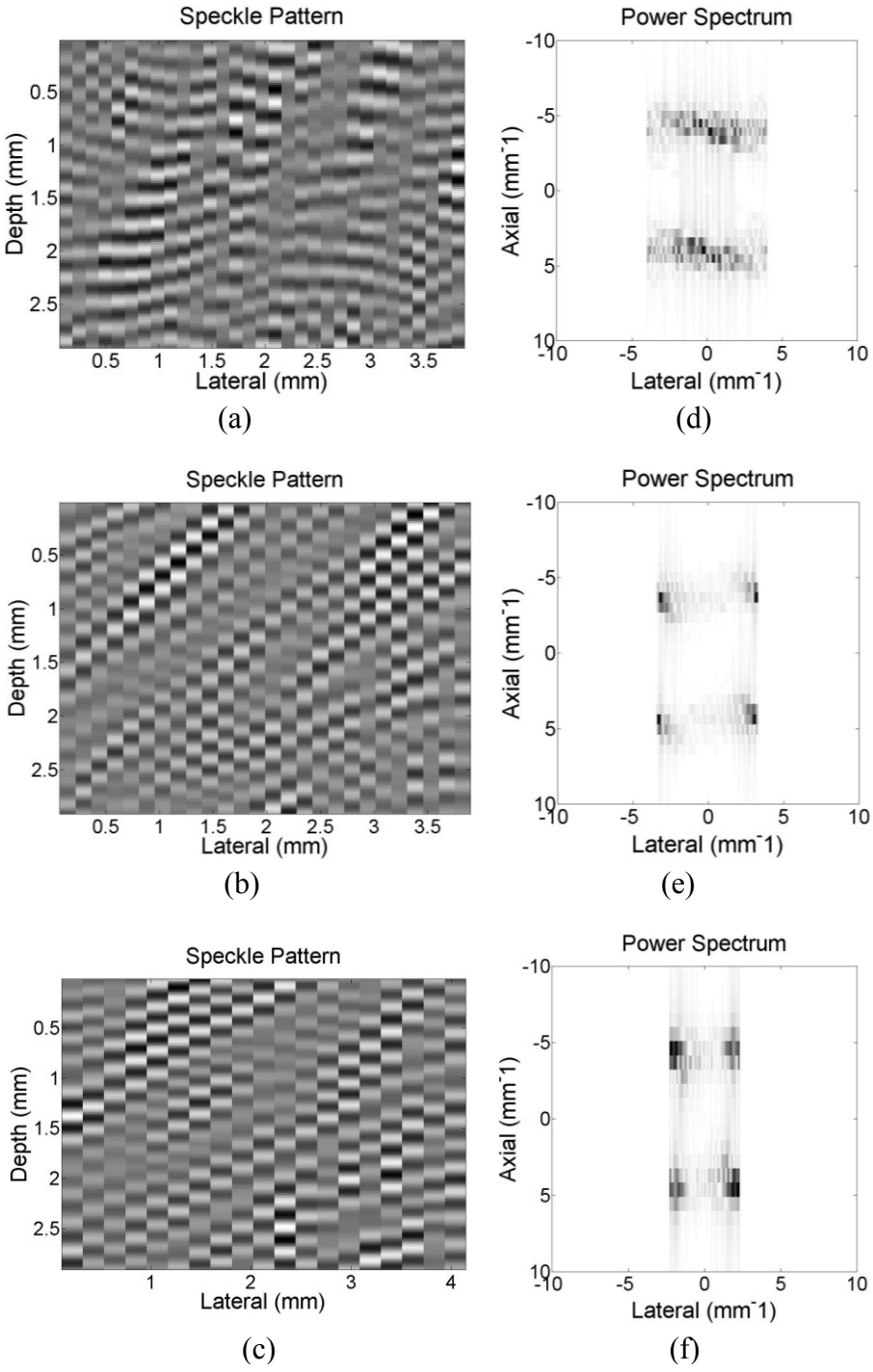

Fig. 7.9. (a) – (c) the speckle pattern of the blood flow (65 cm/s, 50^{o} relative to the ultrasound beam) collected by different scan velocities. Scan velocity is (a) 22 cm/s, (b) 52 cm/s and (c) 75 cm/s. (d) – (f) the power spectrum of the speckle pattern. Scan velocity is (d) 22 cm/s, (e) 52 cm/s and (f) 75 cm/s. Blood flow phantom with A-line increment equal to one half of the lateral beam width ((a), (b), (d), (e)), and one of the lateral beam width ((c), (f)).

7.5 Conclusion

This chapter investigated a new algorithm for two-dimensional blood flow velocity estimation using apparent speckle pattern angle. The apparent angle of speckle pattern changes with different scan velocities due to the mis-registration between the ultrasound beam and scatterers. When the scan velocity equals the lateral component of the blood flow, the apparent angle of the speckle pattern will equal the actual angle of blood flow and the aligned blood flow has a maximum speckle size since the speckle pattern is most spatially correlated in this condition. Blood flow data from computer simulation and flow phantom experiments were both investigated. Our results showed that this algorithm can resolve the amplitude and angle of the blood flow simultaneously. The angle and velocity estimation bias is below 5% in the simulated plug flow. Due to the speckle decorrelation in the simulated parabolic flow and blood flow phantom, the angle of the blood flow will be overestimated and the velocity will be underestimated. The angle and velocity estimation bias increases with decreasing angle between blood flow and the ultrasound beam axis. This chapter provides a new algorithm for two-dimensional blood flow velocity estimation. Only nine scan velocities were used in this chapter. More scan velocities may be applied by an advanced ultrasound imaging system to improve the estimation accuracy.

Chapter 8

Summary

8.1 Objective evaluation

In this dissertation, we investigated and optimized three algorithms for blood flow velocity measurement. The first method optimized was feature tracking, which was previously proposed for three-dimensional blood flow velocity measurement. Optimal thresholds were investigated to select trackable features to minimize flow estimate

variance while providing sufficient spatial and temporal coverage of the flow area (Chapter 3).

Conventional (Doppler-based) blood flow velocity measurement methods using ultrasound are only capable of resolving the axial component of the blood flow velocity vector. Thus, a new method was introduced in Chapter 4 to resolve the lateral component of blood flow within a B-mode image using the observation that the speckle pattern corresponding to blood reflectors (typically red blood cells) stretches (i.e., is "smeared") if the blood is moving in the same direction as the electronically-controlled transducer line selection in a 2-D image. The situation is analogous to the observed distortion of a subject photographed with a moving camera. The results showed that there is a linear relationship between the speckle size and the blood flow velocity, which can be used to resolve the lateral component of the blood flow velocity. Estimation accuracy degraded when speckle decorrelation occurred, whether by shear gradients or rate of scatterer movement out of the ultrasound beam. This method is significantly different than Doppler based methods, since it measures the blood flow velocity using information over space rather than information across time. Repeated data acquisition is not required in this method, which indicates potential time savings for blood flow velocity estimation using speckle size estimation.

The relationship between blood flow velocity estimation for flow purely lateral to the ultrasound beam based on speckle size estimation and flow gradient, ROI size and random scatterer movement was studied in Chapter 5. The results showed that an optimal ROI size exists both in the lateral and axial direction in the flow profile without flow gradient and random scatterer movement. In simulated parabolic flow and blood flow

phantom experiments, an optimal lateral ROI size exists while the estimation error increases with axial ROI size. The comparison of blood velocity estimation for flow purely lateral to the ultrasound beam between speckle size estimation and speckle tracking shows that the accuracy of speckle tracking decreases with increasing blood flow velocity with optimal ROI size while speckle size estimation can measure blood flow velocity over a larger range. This allows researchers to select ROI sizes which minimize computational complexity while preserving estimation accuracy according to specific flow conditions.

The method of blood flow velocity estimation using speckle size estimation was further tested *in vivo* with jugular vein blood flow from human subjects in chapter 6. The jugular vein blood flow data were collected from ten human subjects using a commercial ultrasound imaging system. Spectral Doppler estimates of jugular vein blood flow were collected at the same time compared with the estimation performance of speckle size estimation. A Wilcoxon signed-rank test was used to compare the estimation results of speckle size estimation and spectral Doppler. The results showed that estimation results of speckle size estimation and spectral Doppler are comparable to each other. Instead of repeated beam emitting and receiving in Doppler based methods, speckle size estimation only requires one frame of a general B-mode image, which simplifies the system configuration and indicates potential time savings.

Finally, a two-dimensional blood flow velocity estimation algorithm using apparent speckle pattern angle was proposed in Chapter 7. The apparent angle of speckle pattern changes with different scan velocities due to mis-registration between the ultrasound beam and scatterers. When the scan velocity equals the lateral component of

the blood flow, the apparent angle of the speckle pattern will equal the actual angle of blood flow and the aligned blood flow has a maximum speckle size since the speckle pattern is most spatially-correlated in this condition. Results showed that this algorithm can resolve the amplitude and angle of the blood flow simultaneously.

8.2 Research publications

Published:

[1] Xu, T and Gregory R. Bashford, "Optimal Threshold of Feature Tracking for Blood Velocity and Tissue Motion Estimation," *IEEE Trans. Ultrason, Ferroelectr. Freq. Control*. vol. 56, no. 12, pp. 2624-2629, December, 2009. (Chapter 3)

[2] Xu, T and Gregory R. Bashford, "Resolving the lateral component of blood flow velocity based on ultrasound speckle size change with scan direction and speed," *Proceedings, Annual International Conference of the IEEE Engineering in Medicine and Biology Society*, pp.491-494, 3-6 Sept. 2009. (Chapter 4)

[3] Xu, T and Gregory R. Bashford, "Further progress on lateral flow estimation using speckle size variation," *Proceedings, 2009 IEEE International Ultrasonics Symposium (IUS),* pp.1383-1386, 20-23 Sept. 2009. (Chapter 4)

[4] Xu, T. and G. R. Bashford, "Lateral blood flow velocity estimation based on ultrasound speckle size change with scan velocity," *IEEE Trans.*

Ultrason. Ferroelect. Freq. Control, vol. 57, no. 12, pp. 2695-2703, 2010. (Chapter 4)

[5] Xu T and Gregory R. Bashford, "Effect of flow gradient, ROI size and random scatterer movement during speckle size estimation based blood flow measurement." *IEEE International Ultrasonics Symposium Proceedings*, October, 2011. (Chapter 5)

[6] Xu, T and Gregory R. Bashford, "Two-Dimensional Blood Flow Velocity Estimation Using Apparent Speckle Pattern Angle Dependence on Scan Velocity," *IEEE International Ultrasonics Symposium,* 2012. (Chapter 7)

In review:

[7] Xu, T and Gregory R. Bashford, "Effect of Flow Gradient, ROI Size and Random Scatterer Movement during Speckle Size Estimation based Blood Flow Meausrement," *IEEE Trans. Ultrason, Ferroelectr. Freq. Control.* 2012. (Chapter 5)

In preparation:

[8] Xu, T and Gregory R. Bashford, "In vivo jugular vein blood flow velocity measurement using speckle size estimation", *Ultrasound. Med. Biol.* 2012. (Chapter 6)

[9] Xu, T and Gregory R. Bashford, "Two-dimensional blood flow velocity estimation using ultrasound speckle pattern dependence on scan direction

and velocity," *IEEE Trans. Ultrason, Ferroelectr. Freq. Control.* 2012 (Chapter 7)

8.3 Future work suggestions

The studies presented in this dissertation provide evidence that two-dimensional blood flow velocity can be measured using apparent speckle size and angle within a single B-mode image if the blood flow is moving in the same direction as the electronically-controlled transducer line selection in a 2-D image. However, there are several improvements which can be addressed in future studies.

First, initial attempts at a multiple-scan strategy for estimation flow by a least-squares model (Chapter 4) suggest the possibility of increased accuracy taking into account more than one frame of data. The basic general least-squares model was used for optimization using a limited number of estimation results. Advanced models may be investigated in the future regarding the relationship between scan velocity and blood flow velocity. A potential solution may be to design an adaptive system to dynamically alter the weighting coefficient of each scan velocity with training by a sufficient number of samples of estimated velocities.

Second, the apparent angle of speckle pattern changes with different scan velocities due to the mis-registration between the ultrasound beam and scatterers. Only nine scan velocities were used for data acquisition due the limits of the Antares Ultrasound Imaging System. More scan velocities may be applied by an advanced (or user programmable) ultrasound imaging system. Since the blood flow angle is resolved by searching for the maximum speckle size of an aligned blood flow image, increasing

the number of scan velocities will improve the resolution of blood flow angle estimation, thus increasing the blood flow velocity estimation accuracy.

Third, a high lateral resolution ultrasound imaging system (A-line increment less than one-fourth of the lateral beam width) could be used for data acquisition. When the scan velocity is close to the lateral component of the blood flow velocity, the speckle pattern will be more uniform (spatially coherent) since the scatterers and ultrasound beam are most correlated in this condition, and the power spectrum of the blood flow image will be more concentrated. When the scan velocity is lower or higher than the lateral component of blood flow, the speckle pattern will be complex due to mis-registration between scatterers and the ultrasound beam. As a result, the power spectrum of the blood flow image will be less concentrated. Thus, spectrum analysis on the blood flow images collected by different scan velocities may potentially be used for two-dimensional blood flow velocity estimation.

Bibliography

AllRefer. Carotid duplex. AllRefer 2012. [Online]. Available: http://health. allrefer.com/health/carotid-duplex-carotid-duplex.html

American Stroke Association. Learn About Stroke. American Stroke Association, 2009. [Online]. Available: http://www.strokeassociation.org.

American Stroke Association. Learn About Stroke. American Stroke Association, 2012. [Online]. Available: http://www.strokeassociation.org

Anderson ME. Multi-Dimension velocity estimation with ultrasound using spatial quadrature. IEEE Trans Ultrason Ferroelectr Freq Control 1998; 45(3): 852-861.

Anderson ME, Trahey GE. A seminar on k-space applied to medical ultrasound. Department of biomedical engineering, Duke University, 2006.

Bashford GR, Von Ramm OT. Ultrasound three-dimensional velocity measurements by feature tracking. IEEE Trans Ultrason Ferroelectr Freq Control;43(3): 376-384.

Bashford GR, Robinson DJ. Direct comparison of feature tracking and autocorrelation for velocity estimation. IEEE Trans Ultrason Ferroelectr Freq Control 2007;54(4): 757-767.

Bohs LN, Trahey GE. A novel method for angle independent ultrasonic imaging of blood flow and tissue motion. IEEE Trans Biomed Eng 1991;38(3): 280-286.

Bohs LN, Friemel BH, McDermott BA, Trahey GE. Real-time system for angle-independent US of blood flow in two dimensions: initial results. Radiology 1993;786(1): 259-261.

Burckhardt CB. Speckle in ultrasound B-mode scans. IEEE Trans Sonics Ultrason 1978;25(1): 1-6.

Christensen D. Ultrasonic Bioinstrumentation. New York: John Wiley & Sons, 1988.

Dunmire BK, Beach W, Labs K, Plett M, Strandness DE. Cross-beam vector Doppler ultrasound for angle-independent velocity measurements. Ultrasound Med Biol 2000; 26(8): 1213–1235.

Embree PM, O'Brien WD. The Accurate Ultrasonic Measurement of the Volume Flow of Blood by Time Domain Correlation. Ultrasonics Symposium IEEE 1985; 963-966.

Evans DH, McDicken WN, Skidmore R, Woodcock JP. Doppler Ultrasound: Physics, Instrumentation, and Clinical Applications. New York: John Wiley & Sons, 1989.

Ferrara KW, Algazi VR. A New Wideband Spread Target Maximum Likelihood Estimator for Blood Velocity Estimation -- Part I: Theory. IEEE Transactions on Ultrasonics, Ferroelectrics, and Frequency Control 1991;38(1): 1-15.

Fox MD. Multiple crossed-beam ultrasound Doppler velocimetry. IEEE Trans Sonics Ultrason 1978; 25(2): 281-286.

Friemel BH, Bohs LN, Nightingale KR, Trahey GE. Speckle decorrelation due to two-dimensional flow gradients. IEEE Trans Ultrason Ferroelectr Freq Contro 1998;45(2): 317-327.

Gill RW. Measurement of blood flow by ultrasound; Accuracy and sources of error. Ultrasound Med Biol 1985;11(4): 625-641.

Golstein, LB, Cheryl DB, et al. Guidelines for the Primary Prevention of Stroke: A Guideline for Healthcare Professionals from the American Heart Association/American Stroke Association. Stroke 2011;42:517-584.

Goodman JW. Statistical properties of laser speckle patterns. In: Dainty JC, ed. Laser Speckle and Related Phenomena. Berlin: Springer-Verlag, 1975. pp. 9-75.

Hamilton JD, Larry YLM, Bashford GR. Ultrasound based quantitative motion measurement using speckle size estimation. U.S. Patent 6,318,179 B1, Nov. 20, 2001.

Hein IA, O'Brien WD. Current time-domain methods for assessing tissue motion by analysis from reflected ultrasound echoes-A review. IEEE Trans. Ultrason. Ferroelectr. Freq. Control 1993; 40(2): 84-102.

Hein IA. 3-D flow velocity vector estimation with a triple-beam lens transducer - Experimental results. IEEE Transactions on Ultrasonics, Ferroelectrics and Frequency Control 1997;44(1): 85-95.

Hoskins PR. A review of the measurement of blood velocity and related quantities using Doppler ultrasound. Proc Inst Mech Eng 1999; 213(5): 391-400.

Insana MF. Ultrasonic imaging. In: Akay M, ed. Wiley Encyclopedia of Biomedical Engineering. Hoboden, NJ: Wiley, 2006.

Jensen JA, Svendsen NB. Calculation of pressure fields from arbitrary shaped, apodized, and excited ultrasound transducers. IEEE Trans Ultrason Ferroelectr Freq Control 1992; 39(2): 262-267.

Jensen JA. Field: A program for simulating ultrasound systems. Med Biol Eng Comput 1996a; 34(1): 351-353.

Jensen JA. Estimation of Blood Velocities using Ultrasound: A Signal Precessing Approach. Cambreidge, UK: Cambridge University Press, 1996b.

Jensen JA, Munk P. A new method for estimation of velocity vectors. IEEE Trans Ultrason Ferroelectr Freq Control 1998;45(3): 837-851.

Jensen JA. Medical ultrasound imaging. prog Biophys Mol Biol 2007; 93(1-3): 153-165.

Jensen JA. Field II Simulation Program. Technical University of Denmark, 2011. [Online]. Available: http://server.oersted.dtu.dk/personal/jaj/field/?main.html

Jorgensen HS, Nakayama H, Reith J, Raaschou HO and Olsen TS, "Stroke recurrence: predictors, severity, and prognosis," Cerebrovasc Dis. 6(supppl 2): 11, 1996.

Kasai CK, Namekawa AK, Omoto R. Real-time two-dimensional blood flow imaging using an autocorrelation technique. IEEE Trans Sonics Ultrason 1985; 32:458-463.

Kuo J, Von Ramm OT. Three-dimensional motion measurement using feature tracking. IEEE Trans Ultrason Ferroelectr Freq Control 2008;55(4): 800-810.

Lay DC, Stade E. Linear Algebra and its applications, 3rd edition. Boston, Massachusetts: Addison Wesley press, 2005.

Lowry R. Concepts & Applications of Inferential Statistics. Poughkeepsie, NY. 2011.

Morsy AA, Von Ramm OT. FLASH Correlation: A New Method for 3-D Ultrasound Tissue Motion Tracking and Blood Velocity Estimation. IEEE Trans Ultrason Ferroelect Freq Contr 1999;46(3): 728-736.

National Heart Lung and Blood Institute. Explore stroke. NHLBI 2012. [online]. Available: http://www.nhlbi.nih.gov/health/health-topics/topics/stroke/types.html

Newhouse VL, Reid J. Invariance of Doppler bandwidth with flow axis displacement. Proc IEEE Ultrasonics Symp 1990;3: 1533-1536.

Newhouse VL. Censor D, Vontz T, Cisneros JA, Goldberg BB. Ultrasound Doppler Probing of Flows Transverse with Respect to Beam Axis. IEEE Transactions on Biomedical Engineering 1987;34(10): 779-789.

Niels O, Lovstakken L, Torp H, Jensen JA. Estimating 2-D vector Velocities Using Multidimensional Spectrum Analysis. IEEE Trans Ultrason Ferroelect Freq Control 2008;55(8): 1744-1754.

Ortiz, SHC, Chiu T, Fox MD. Ultrasound image enhancement: A review. Biomedical Signal Processing and Control 2012. [Online]. Available: http://dx.doi.org/10.1016/j.bbr.2011.03.031

Overbeck JR, Beach KW, Strandness DE. Vector Doppler: Accurate measurement of blood velocity in two dimensions. Ultrasound Med Biol 1992;18(1): 19–31.

Phillips PJ, Kadi AP, Von Ramm OT. Feasibility Study for a Two-Dimensional Diagnostic Ultrasound Velocity Mapping System. Ultrasound in Med Biol 1995;21(2): 217-229.

Roger VL, Go AS, Lloyd-Jones DM, et al. Heart disease and stroke statistics—2012 update: a report from the American Heart Association. Circulation 2012; 125(1):e2-e220.

Roundhill DN. Ultrasound time domain velocity measurement. Ph.D. dissertation, Duke Univ., Durham, NC, 1991.

Shirley D, Weardon S, Chilko D. Statistics for Research, Third Edition. Hoboken, New Jersey; John Wiley & Sons, Inc, 2004.

Scabia, M, Calzolai M, Capineri L, Masotti L, Fort A. A real-time two-dimensional pulsed-wave Doppler system. Ultrasound Med Biol 2000;26(1): 121–131.

Schlaikjer M, Jensen JA. Maximum likelihood blood velocity estimator incorporating properties of flow physics. IEEE Trans Ultrason Ferroelectr Freq Control 2004;51(1): 80-92.

Swillens A, Segers P, Lovstakken L. A combined speckle tracking and phase-shift estimation approach for 2D blood flow imaging in the carotid bifurcation. Proc IEEE Ultrason Symp 2010; 1072-1075.

The Heart Foundation. Heart diseases statistics. The Heart Foundation, 2012. [Online]. Available: http://www.theheartfoundation.org/heart-disease-facts/heart-disease-statistics/

Trahey GE, Allison JW, Von Ramm OT. Angle independent ultrasonic detection of blood flow. IEEE Trans Biomed Eng 1987;34(2): 964-967.

Veyseller, B, Aksoy F, Acikalin M, Yildirim YS, Ivain Bayraktar FG and Demirhan H, "Assessment of internal jugular vein flow and patency with power duplex Doppler ultrasonography after functional neck dissection," *Kulak Burun Bogaz Ihtis Derg.* 2010 Jan-Feb; 20(1):38-43.

Von Ramm OT, Smith SW. Beam steering with linear arrays. IEEE Trans Biomed Eng 1983; BME-30(8): 438-452.

Wagner RF, Smith SW, Sandrik JM, Lopez H. Statistics of speckle in ultrasound B-scans. IEEE Trans Sonics Ultrassonics 1983;30(3): 156-163.

Wilcoxon F. Individual comparisons by ranking methods. Biometrics Bulletin 1945;1(6): 80 – 83.

Xu T, Bashford GR. Resolving the lateral component of blood flow velocity based on ultrasound speckle size change with scan direction and speed. Proceedings, Annual International Conference of the IEEE Engineering in Medicine and Biology Society 2009a; 491-494.

Xu T, Bashford GR. Further progress on lateral flow estimation using speckle size variation. Proceedings, IEEE International Ultrasonics Symposium 2009b; 1383-1386.

Xu T, Bashford GR. Lateral blood flow velocity estimation based on ultrasound speckle size change with scan velocity. IEEE Trans Ultrason Ferroelect Freq Control 2010; 57(12): 2695-2703.

Zahiri-Azar R, Salcuden SE. Time-delay estimation in ultrasound echo signals using individual sample tracking. IEEE Trans Ultrason Ferroelectr Freq Control 2008;55(12): 2640-2650.

Zhai L. Imaging and characterizing human prostates using acoustic radiation force. Ph. D dissertation, Duke Univ., NC, 2009.